Fundamental Interactions of Glassy Carbon and Graphite with liquid Fe-C and Fe-Ti-C-N

Submitted in partial fulfillment of the requirements for

the degree of

Doctor of Philosophy in

Materials Science and Engineering

Steven Thomas Britt

B.S., Materials Engineering, Auburn University
M.Sc., Materials Science and Engineering, Carnegie Mellon University

Carnegie Mellon University
Pittsburgh, PA

August 2022

For my three grandfathers: Pops, Grandpa, and D.C.
Each of you has had a profound effect on both my character and my approach to technical problems. The lessons learned with you did not stop at fixing tractors or changing batteries but extended into solving the problems within these pages. I stand on the lessons you taught me.

Acknowledgements

Any work with this many hours invested cannot be accomplished without some small help from others. I have received much. This work could not be accomplished without the assistance of my advisor, Prof. Chris Pistorius, who was not just advisor but also partner in the laboratory. Thank you for support in my research, but also allowing me to pursue my love of the arts concurrently. My thanks to my committee members: Prof. Bryan Webler, Prof. Anthony Rollett, Dr. Robert Nightingale, and Dr. Yun Li for your time and your careful review of this project. Your comments have transformed this thesis from an anthology of work to a cohesive narrative.

This research was supported by the member companies of the Center for Iron and Steelmaking Research at Carnegie Mellon University. The characterization techniques made use of the Materials Characterization Facility at CMU, which was supported by grant MCF-677785. Thank you to Dr. Betsy Clark and Logan Solotky for their time, training, and suggestions.

I must thank my seniors: Dr. Dai Tang, Dr. Stephano Piva, Dr. Ming Tang, and Dr. Chris Kantos. Your knowledge and willingness to teach and advise were vital to my learning, growth, and work. Thank you to Alyssa Shear for guidance in creating figures. Thank you to Dr. Matt Wilkin who was a constant companion throughout my time at CMU. Thank you to Dr. Jason Kush: the joy and growth your lessons brought me often overcame the frustration of the slow progress of my research.

Thank you to my parents, Anne and Bo, who have flown around the world to support me. This work may be a performance of a different type, but your steadfast support is the same. Thank you to my sister Christy for your patience when proof-reading this document. Thank you to my friends from CMU, Bellefield, and H_2O. Your companionship eased the weight of this work, lifted my spirits, and given me great joy.

Finally, I give thanks to the Lord my God who has strengthened my hands through this process.

Soli Deo Gloria

Table of Contents

List of Figures

List of Tables

1 Abstract

The fundamental interactions of liquid iron with carbon, titanium, and nitrogen are at the heart of the blast furnace process, dictating productivity and longevity. The interactions of liquid Fe and C are particularly important in the hearth, with dissolution governing the properties of degradation of the carbonaceous hearth. When titanium and nitrogen are included in liquid Fe-C, Ti(C,N) can catalyze the solidification of an iron skull, further protecting refractory. Though a four-component system may seem simple, basic questions still need to be answered as to how these interactions affect the hearth refractory and, therefore, the campaign life of the blast furnace. A set of experiments is presented to illuminate how the formation of Ti(C,N) may protect the hearth. Graphite rods were dissolved into Fe-C containing Ti(C,N) but showed little difference in dissolution rate compared to rods dissolved without Ti(C,N). Rods with carbonaceous coatings doped with TiC, TiN, and Ti(C,N) were dipped into stagnant liquid Fe-C to test the propensity of dopants to assist in shell solidification. These experiments showed the importance of heat extraction to protecting the hearth. Micrographs of iron-carbon interfaces saw the majority of Ti(C,N) in large agglomerations away from the interface. The ability of Ti(C,N) to form these large agglomerations is likely the reason Ti additions are uniquely able to protect the hearth. The interactions of liquid Fe-C_{sat} and glassy carbon are also investigated to determine if glassy carbon is a suitable material for the hot face. Other experiments are documented to increase the utility of the high temperature confocal scanning laser microscope.

2 Introduction

The blast furnace (BF) is the primary way to reduce iron ore into hot metal (HM). Despite the increase in direct reduction techniques, the BF method was used to produce 1.28 billion tonnes of pig iron compared to 111 million tonnes by direct reduction in 2019 [1]. It remains the most productive method to reduce iron and is a vital step in the integrated steel process. Though emissions standards and the rise of direct reduced iron seek to eliminate the blast furnace, western ironmakers are scheduling relines of furnaces to attain one more campaign before phasing out the technology [2,3]. The reduction of iron ore by the BF is a continuous process - operating 24/7- and a well performing BF is productive and safe. BF up-time can be limited by a number of occurrences – including tuyere failure [4], top replacement [5], stave bending [6], reline of the bosh/upper refractory [7]. The major limitation of campaign life is the wear of the hearth refractory, due to multiple months of downtime, and the cost of materials and labor [8]. Campaign lives have started averaging 15-23 years with some campaigns as high as 30 years [2,3,9].

A schematic of the BF is shown in Figure 2.1a. Alternating layers of iron ore and coke are charged through the top of the furnace to be gradually reduced as the burden (the material that is charged) descends. Separate layers cease to exist in the cohesive zone as the iron is fully reduced and begins to melt. The scale of the blast furnace creates a variety of temperatures and conditions; Figure 2.1b denotes the zones of the BF, and the schematic is color-coded to the different types of refractory used in the furnace [2]. This range of refractories is needed because different zones are subject to degradation by different causes. For example, the primary concern of the stack refractory is abrasion while the bosh is subject to both thermal shock and chemical attack [10]. Though the hearth refractory is not necessarily more prone to degradation than those in other zones, its position within the furnace limits access and spells the end of campaign life for any major repair [3,10].

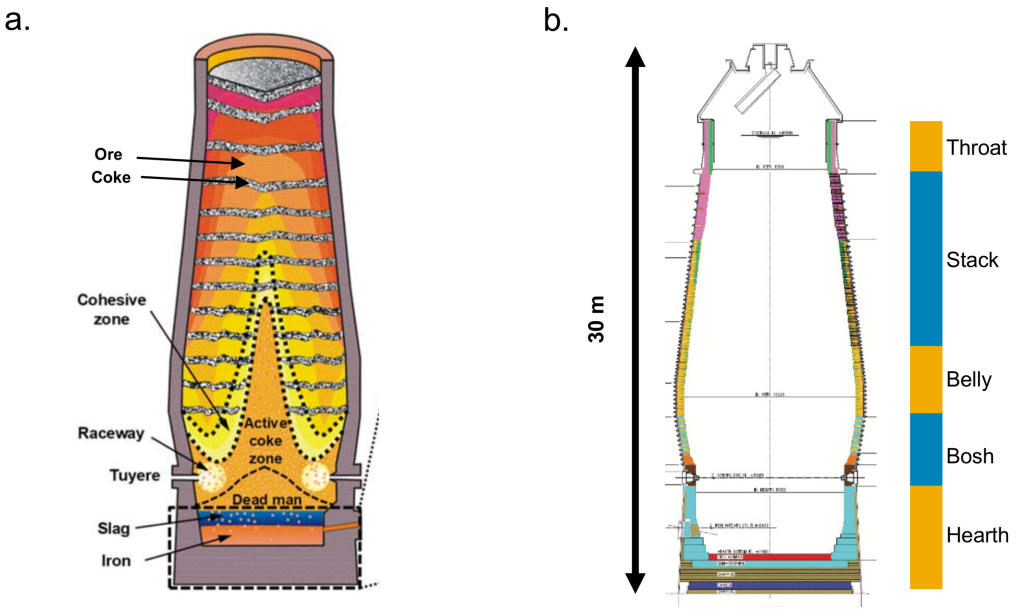

Figure 2.1. Schematic of blast furnace. a) representation of internal reaction zones. Adapted from [11]. b) representation of BF zones and color coating of the different refractory types in use. Green represents SiC; pink represents chamotte; red represents alumina; and all other colors represent a form of carbon. Adapted from [2].

The high temperatures and contact with liquid and vapor species create a number of routes for the hearth to degrade. Modern blast furnace hearths use bricks made of carbon, chosen to limit the number of degradation routes. Carbon refractory has the advantage of resistance to thermal shock and increased thermal conductivity compared to traditional refractory material [10]. However, introducing liquid Fe to carbon allows a dissolution reaction to occur, removing refractory from the hearth. If the liquid iron is not saturated in carbon, dissolution will occur when the liquid contacts the carbonaceous refractory. At 1500 °C, pure iron can dissolve 5.2% wt carbon [12]. The majority of this comes from coke, but dissolution does occur if the deadman (a porous coke bed in the hearth) is either clogged or floating.

Dissolution is sensitive to the type of carbon. Dissolution of graphite is generally mass transfer limited, but amorphous forms of carbon (coke and coal) can be under interfacial or mixed control [13,14]. Dissolution limited by mass transfer is governed by the removal of liquid high in [C] from the diffusion boundary layer. This is well evidenced near BF tapholes. The faster velocities allow for faster dissolution, and the refractory near the taphole degrades more quickly. “Elephant’s foot” wear profiles, shown in Figure 2.2, are often observed at the end of campaign lives [10]. This profile is related to mass transfer limited dissolution, enhanced by peripheral metal flow when the deadman is either clogged or floating [15]. The simulations of Barbes et al. showed

similar profiles when using a nodal wear model, i.e., not accounting for fluid flow but primarily heat transfer [16]. Hearth deterioration is caused by more than dissolution - notably spalling and attack by alkalis, zinc, and oxygen [10,17]- but it is the focus for this work.

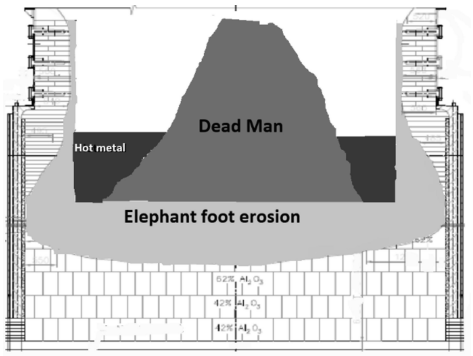

Figure 2.2. Schematic representation of the floating deadman and hearth with "elephant's foot" wear profile. Figure reproduced with permission [10].

Despite the many ways refractory can fail, extensive BF campaigns are obtained if the furnace is well operated and charged with high quality materials. One of the primary ways the hearth life is decreased is when operating at high productivity [18], but the quality of raw materials, particularly the coke, is also vital. Low quality coke degrades into fines more easily which can block pores in the deadman. These fines can be carbonaceous [19] or minerals like calcium aluminates [20]. It is important that the deadman remains porous, allowing most of the carbon pickup to come from the coke rather than the carbon walls.

Unfortunately, there are few fixes once a portion of the hearth is worn away. The exception to this is the charging of titanium containing ore, often ilmenite. A case study from Shougang Jingtang BF No. 2 is presented in Figure 2.3 [18], but other industrial reports tell similar stories [21–24]. It was found that when hearth temperatures increased, adjusting the flow rate and temperature of the cooling water (line A) had a marginal effect. Furnace productivity could be decreased to control the temperature (Line B), but the temperatures at normal productivity (Line C) were only returned to normal after ilmenite charging began (Line D).

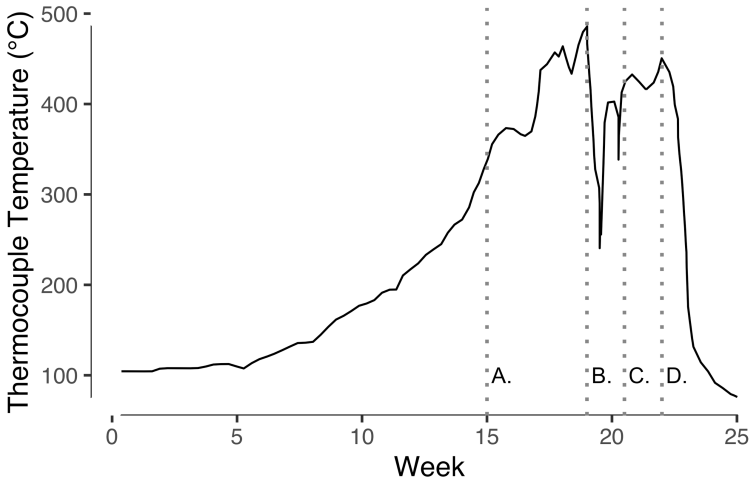

Figure 2.3. Case Study of Shougang Jingtang BF No. 2 [18]. Line A: Water flow rate increased. Line B: Production decrease. Line C: Production increase. Line D: Ilmenite charging initiated.

There is strong evidence that the charging of Ti ores protects the hearth from wear, but further studies need to be done to understand the mechanism and intricacies of the process. Bergsma and Fruehan's mechanism is commonly accepted, shown by schematic in Figure 2.4 and explained below [25].

1. Ti ore charged into the furnace is reduced, with [Ti] dissolving in the HM.
2. Refractory is in contact with hot metal (Figure 2.4a) then lost in a wear event (Figure 2.4b). This thinner region of intact refractory has a lower thermal resistance between the hot face and the cooled outside of the hearth. The lower resistance results in a lower hot-face temperature (Figure 2.4b).
3. When the temperature is low enough (occurring after enough refractory loss), the formation of Ti(C,N) crystals is thermodynamically favorable, shown in Figure 2.4c.
4. Ti(C,N) crystals restrict the flow of metal in the region of lost refractory. Enough restriction can facilitate heat extraction so that the iron can solidify, shown in Figure 2.4d.

This mechanism has overlap with the concept of fluidity in the casting industry. There, the formation of higher melting point solid metal dendrites can restrict the flow of the liquid, preventing metal from entering some of the cavities [26]. Here, the carbonitrides restrict the flow of HM while heat is extracted through the hot face. The restriction of the metal flow can be understood in terms of the Einstein-Roscoe relation: an increase in solid fraction restricts flow and therefore increases effective viscosity [27].

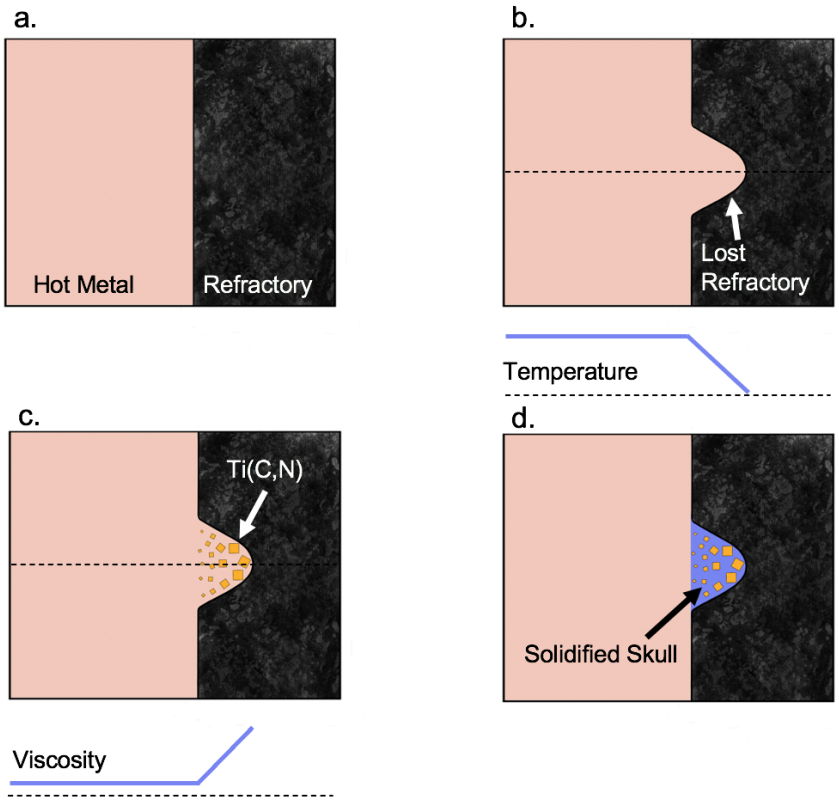

Figure 2.4. Hypothesized mechanism of Ti(C,N) protection of the hearth. a.) HM-refractory interface before wear has occurred. b.) a wear event has occurred, leaving a thinner region of refractory. The thinner region promotes a temperature drop in the hot metal in the region that was lost. c.) if the temperature is low enough, Ti(C,N) become stable. This increased solid volume increases viscosity. d.) With HM flow restricted by the solid Ti(C,N), enough heat can be extracted to solidify a skull in the region where refractory was lost.

Despite wide acceptance of this mechanism by industry, fundamental questions remain. One unknown is how far the mechanism must proceed to see beneficial effects. In isothermal dissolution experiments absent of Ti(C,N), Deng et al. saw a reduction in the dissolution rate of hearth samples with dissolved [Ti] in HM [28]. While the eutectic temperature of iron is 1147 °C, Ti(C,N) is stable at higher temperatures, and the presence of the solid Ti(C,N) could restrict the flow of HM enough to protect refractory even without skull solidification. As the hearth can degrade by multiple mechanisms, there are also questions of what mechanism of deterioration Ti additions help. Guo et al. developed computational models to study where Ti would build up in the hearth. Their results showed Ti(C,N) build-up in the bottom corners of the BF, most helpful in preventing the dissolution that leads to an "elephant's foot" wear profile [29]. However, the remedial effects of Ti additions warrant study beyond their model. Another question is how Ti(C,N) localizes within the BF [30]. Does Ti(C,N) show a propensity to anchor to the carbonaceous refractory or does it form in a dynamic equilibrium (analogous to liquid-vapor interfaces)? This dynamic equilibrium would occur from

hotter HM (with no precipitated Ti(C,N)) replacing cooler HM (with Ti(C,N)) near the hot face. The hotter HM would begin to cool and form Ti(C,N) and the cooler HM would begin to warm and redissolve Ti(C,N). Answering these questions could help inform better ways to charge Ti into the furnace.

Within the last 20 years, industry has been developing new methods of introducing Ti to the BF [24]. Ti has previously been added to the BF through the burden, through the tuyeres, and through taphole clay [31]. Nippon Steel has reported that carbonaceous refractory doped with either Ti or TiC has an improvement over undoped refractory, earning a patent [32]. The form in which Ti is added is important, but - to the author's knowledge - no work has been published comparing the protective effects of the carbide versus the nitride or carbonitride. The form of Ti dictates thermodynamic stability as well as wetting behavior with HM. Thermodynamic stability varies between Ti(C,N)- the stable form in the blast furnace- TiC, and TiN [30].

The investigations in this work seek to answer the questions posed above. No two investigations used the same procedure, with the exception of Ch. 5 and Ch. 9. Each study is presented as an independent chapter, with all the needed information in a single chapter. This means that each chapter contains its own abstract, experimental section, etc., rather than all methods being contained within a single experimental chapter. This was done to help the reader access all the information of interest in a single chapter. To keep all necessary information contained within each chapter, some information and figures will appear multiple times, particularly in the introduction sections. The "Within the Narrative" sections of the chapters seek to help guide the reader between chapters, contextualizing the chapter within the larger work while denoting which parts were necessarily repeated to allow the chapter to stand alone.

The investigations directly relevant to the blast furnace are contained in Ch. 5-9. Ch. 10-11 documented the necessary work to better understand of the results of the *in-situ* observations in Ch. 5 and Ch. 9. Ch. 10-11 were more tangential to the industrial application but are important to supporting the work within this document and to the broader community. A short description of each chapter is given:

- Ch. 5 is a qualitative view of how Ti(C,N) particles interact in liquid HM.
- Ch. 6 investigates the effect of Ti(C,N) on isothermal dissolution.
- Ch. 7 tests the effect of Ti-based dopants on the propensity of carbon rods to solidify iron shells in a stagnant melt.

- Ch. 8 does not consider the effect of Ti but shows the dramatic case of catalytic graphitization of glassy carbon while comparing the effects to a laboratory coke analog.
- In Ch. 9, it was attempted to probe the thermodynamics of the Fe-Ti-C_{sat} system by the confocal scanning laser microscope (CSLM) as an extension of Li et al. [33].
- To perform the work of the preceding chapter, an investigation of metal-crucible interactions was needed to improve the visibility of liquid metal samples within the CSLM (Ch. 10).
- In Ch. 11, multiphysics simulations and experimental observations were combined to characterize the fluid conditions within molten metal samples heated in the CSLM.

2.1 References

[1] World Steel Association: *Steel Statistical Yearbook 2020 Concise Version*, 2020.
[2] F. Kerkhoven, J. Stuurwold, G. Tijhuis, B. Nugteren, and R. van Laar: *Iron Steel Technol.*, 2022, vol. 19, 3 (March), pp. 70–9.
[3] V. Vogl, O. Olsson, and B. Nykvist: *Joule*, 2021, vol. 5, pp. 2646–62.
[4] T.L. Gao, K.X. Jiao, H.B. Ma, and J.L. Zhang: *Ironmak. Steelmak.*, 2020, pp. 1–6.
[5] T.J. Jolink, J.W. Entwistle, D. Berdusco, and P. Bermes: in *AISTech Proceedings*, 2018, pp. 353–6.
[6] R. Horwood, R. Mawer, R. Harvey, and D. Osborne: in *AISTech Proceedings*, 2019, pp. 359–64.
[7] N. Ward and J. D'Alessio: in *AISTech Proceedings*, vol. 2018, 2018, pp. 523–31.
[8] A.J. Dzermejko: *Iron Steel Technol.*, 2015, vol. 12, 3 (March), pp. 58–70.
[9] S. Filatov, I.F. Kurunov, Y. Gordon, A. Sadri, and W. Ying: in *AISTech Proc.*, 2016, pp. 695–704.
[10] S. Biswas and D. Sarkar: in *Introduction to Refractories for Iron- and Steelmaking*, 2020, pp. 147–218.
[11] L. Shao, Q. Xiao, C. Zhang, Z. Zou, and H. Saxén: *Processes*, 2020, vol. 8, pp. 1–16.
[12] F. Neumann, H. Schenck, and W. Patterson: *Giesserei*, 1960, vol. 47, pp. 25–32.
[13] D. Jang, Y. Kim, M. Shin, and J. Lee: *Metall. Mater. Trans. B*, 2012, vol. 43B, pp. 1308–14.
[14] C. Wu, R. Wiblen, and V. Sahajwalla: *Metall. Mater. Trans. B*, 2000, vol. 31, pp. 1099–104.
[15] K. Komiyama, B. Guo, H. Zughbi, P. Zulli, and A. Yu: *Metall. Mater. Trans. B*, 2014, vol. 45, pp. 1895–914.
[16] M.F. Barbés-Fernández, E. Marinas-García, E. Brandaleze, R. Parra-Figueroa, L.F. Verdeja-González, G.A. Castillo-Rodriguez, and R. Colás: *ISIJ Int.*, 2008, vol. 48, pp. 134–40.
[17] S. Silva, F. Vernilli, S. Justus, O. Marques, A. Mazine, J. Baldo, E. Longo, and J. Varela: *Ironmak. Steelmak.*, 2005, vol. 32, pp. 459–67.
[18] J. Huo and J. Huang: *Ironmak. (In Chinese)*, 2013, vol. 32, pp. 14–6.
[19] M. Geerdes, R. Chaigneau, and O. Lingiardi: *Modern Blast Furnace Ironmaking: An Introduction (2020)*, Ios Press, 2020.
[20] M. Chapman, R. Nightingale, and B. Monaghan: *CHEMECA 2011 Australas. Conf. Chem.*

Eng., 2011, pp. 1–14.
[21] S. Street, C. Copeland, and E. Worral: in *AISTech Proceedings*, 2013, pp. 381–403.
[22] J.W. Entwistle, J. Grindey, R. Albanese, D. Lee, B. Rogers, T. Schrenk, M. McCoy, I. Cameron, M. Sukhram, M. Bodley, R. Midha, M. Al-Dojayli, K. Chomyn, Y. Ghobara, J. Busser, and P. Towsey: *Iron Steel Technol.*, 2020, vol. 17, pp. 64–74.
[23] K. Narita, M. Maekawa, T. Onoye, Y. Satoh, and M. Miyamoto: *Trans. Iron Steel Inst. Jpn.*, 1977, vol. 17, pp. 459–68.
[24] M. Nitta and K. Hatakeyama: *Nippon Steel Tech. Rep.*, 2020, pp. 40–4.
[25] D. Bergsma and R.J. Fruehan: *60th Ironmak. Conf. Proc.*, 2001, pp. 297–312.
[26] L. Arnberg and A. Mo: in *Casting Vol. 15 ASM Handbook*, D.T. Srinath Viswanathan, Diran Apelian, Raymond J. Donahue, Babu DasGupta, Michael Gywn, John L. Jorstad, Raymond W. Monroe, Mahi Sahoo, Thomas E. Prucha, ed., ASM International, 2008, pp. 375–8.
[27] R. Roscoe: *Br. J. Appl. Phys.*, 1952, vol. 3, pp. 267–9.
[28] Y. Deng, J. Zhang, K. Jiao, and Z. Liu: *ISIJ Int.*, 2019, vol. 59, pp. 1–8.
[29] B. Guo, P. Zulli, D. Maldonado, and A. Yu: *Metall. Mater. Trans. B*, 2010, vol. 41, pp. 876–85.
[30] Y. Zhao: *Iron Steel Technol.*, 2014, vol. 11, 3 (March), pp. 95–103.
[31] S. Street, A. Cheng, and I. Cameron: in *AISTech Proceedings*, 2019, pp. 275–88.
[32] H. Inoue, M. Nitta, T. Matsui, T. Wakasa, Y. Yamagami, and T. Mochida: *United States Pat.*, Patent #8889062, Nippon Steel and Sumitomo Metal Corporation, 2014.
[33] Y. Li, Y. Li, and R.J. Fruehan: *ISIJ Int.*, 2001, vol. 41, pp. 1417–22.

3 Literature Review

3.1 Thermodynamics Review

Understanding the thermodynamics of Ti(C,N) formation in liquid Fe is critical both to understanding industrial practice and the performed experiments. Forming Ti(C,N), or avoiding formation, is important to the hearth protection and to prevent downstream issues in both metal and slag. Relevant thermodynamics are reviewed to provide the best prediction of the conditions needed to form Ti(C,N). Though this seems trivial given the availability of thermodynamic packages like FactSage and Thermo-Calc, even a simple number like the saturation limit for carbon in liquid iron has some disagreement between different solution databases and is worthy of investigation.

3.1.1 Carbon structure

Even as a single-component system, the phases and structure of carbon can vary widely. Three phases will be considered in this thesis: graphite, coke, and glassy carbon. Graphite is the most stable form of carbon at atmospheric pressure [1]. A single sheet of graphite (i.e., graphene) is comprised of sp^2 bonded carbons forming 6-member rings in a 2D plane [2]. In graphite, single planes of graphene are stacked and held together by van der Waals bonds. Glassy carbon is a close structural variation of this. Rather than wide 2D sheets of carbon atoms, glassy carbon is comprised of much smaller sheets. These contain bonded carbons of 5 and 7 member rings, which creates curvature in these sheets [3]. These sheets tangle and intertwine creating a disordered structure only comprised of sp^2 bonds [3,4].

Coke is carbon source derived from heating certain types of coal in the absence of O_2 to remove volatile matter, and to allow the structure to soften and subsequently resolidify in a stronger form [5]. Coke falls into a broader structural class of 'amorphous carbons'. These are defined as containing 1-10% sp^3 bonds [2]. These sp^3 bonds are interplanar, and those bonds create a more 3D structure due to the crosslinking between planes [6].

The structure of each allotrope affects its thermodynamic stability. Both coke and glassy carbon are metastable structures, with graphite being the stable form [1]. It might be expected that cokes exhibit excess enthalpy and entropy compared to graphite while glassy carbon only exhibits excess entropy. Instead, both coke and glassy carbon both have excess enthalpy and entropy [1].

3.1.2 Liquid Fe with C and C-N

The full predictive power of thermodynamic databases is only applicable if simpler systems are represented accurately. Therefore, the simplest system will be presented first: binary Fe-C. The most important region for the experiments performed in this work is the carbon-saturated, liquid region. Even in such a simple system, there is disagreement. Figure 3.1 shows the experimental data [7–9] compared to the prediction by an analytical model (Neumann), a thermodynamic evaluation (Gustafson), FactSage (FSstel 8.1), and Thermo-Calc (TCFE11) [10–13]. The results of FSstel match the analytical solution of Neumann and Gustafson closely. These agree with the experimental data of Chipman and Kitchner. Nakagawa saw higher concentrations from experiments performed in a CO atmosphere [11]. TCFE11 is close to the data of Nakagawa; it over-predicted the saturation of the other data by about 0.07% wt C.

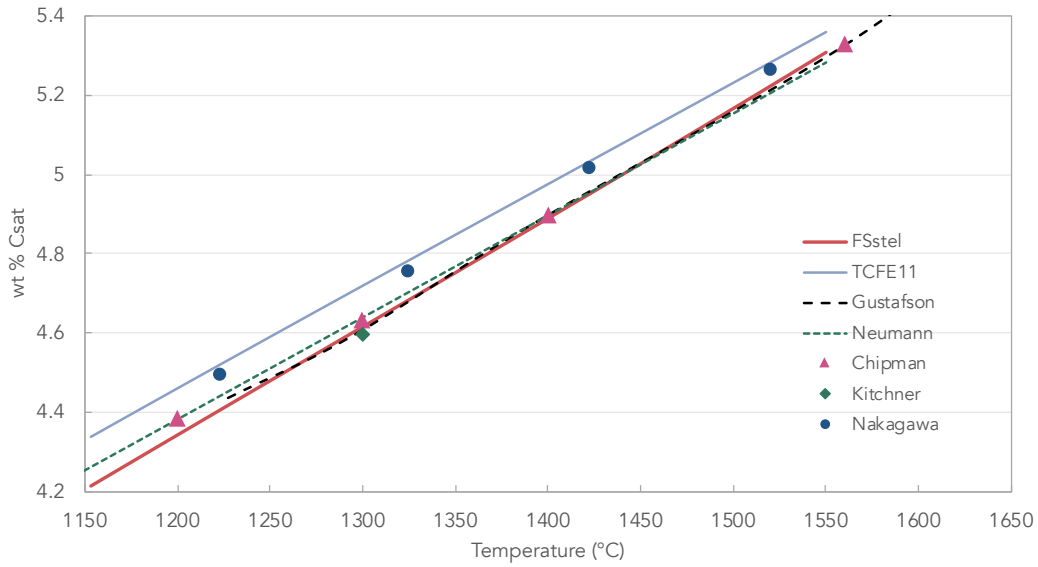

Figure 3.1. Results of the graphite saturation values in liquid Fe [7–11]. Comparison of experimental data (shown by points), literature models (the dotted line), and thermodynamic databases (solid lines).

While there is reasonable agreement on the graphite saturation limit in liquid Fe, the nitrogen saturation limit in liquid Fe-C_{sat} is less clear. The solubility of [N] with temperature is compared in Figure 3.2. Older literature predicts an increase of [N] with temperature [14–19], but the recent experiments by Jang et al. show the opposite [20]. FactSage FSstel 8.1 followed the results of Jang, Miyamoto, and Tsukihashi. FactSage FSmisc 8.1 far overpredicted the solubility. Thermo-Calc TCFE10 followed the trend of data reported by Opravil & Pehlke and Svyazhin, but over-predicted the solubility compared to those points.

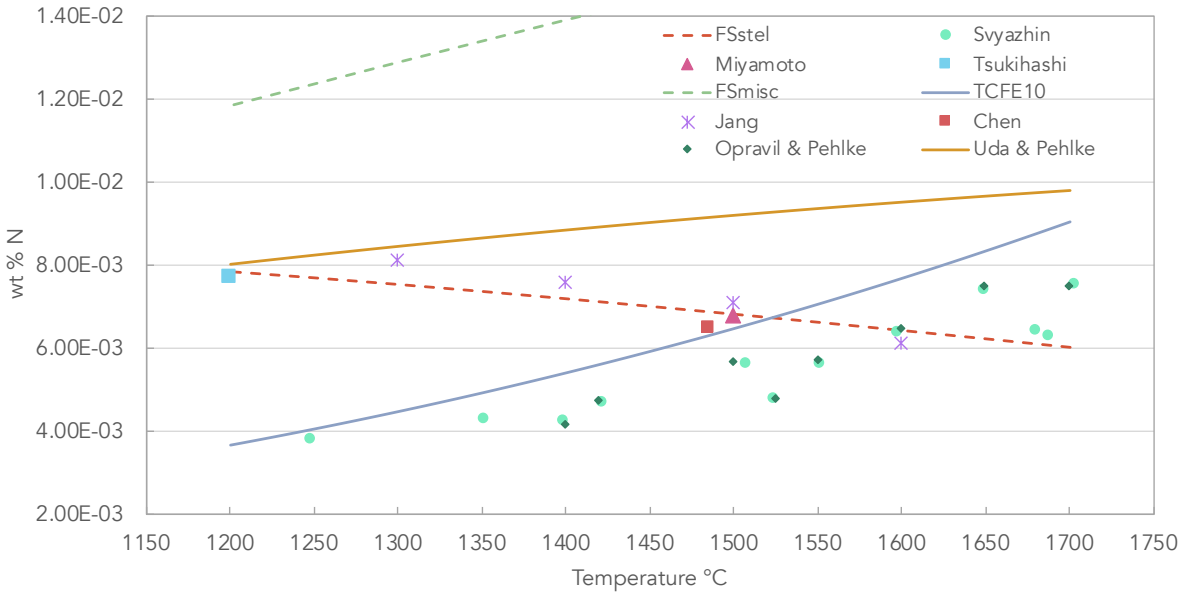

Figure 3.2. Nitrogen Solubility in Fe-C_{sat} alloys [14–20]. Calculations were performed with p_{N_2} = 1 atm. Data points are experimental data from the listed sources. Lines are calculated from thermodynamic databases (Thermo-Calc, FSstel 8.1, FTmisc 8.1), with the exception of Uda & Pehlke.

3.1.3 Thermodynamics of Ti(C,N)

Ti(C,N) is a near-ideal solid solution comprised of TiC and TiN in an FCC structure with anion positions filled with either C, N, or a vacancy [21,22]. The solid solutions are reported as having most anion sites filled, though as much as 40% of the anion sublattice can be vacant for the pure components [23,24]. The non-stoichiometry of the compounds greatly affects surface energy and therefore the wetting by liquid metals. Ag and Cu were reported to wet neither stoichiometric TiC nor TiN, but wettability increased with increasing non-stoichiometry [23]. Iron was reported to wet stoichiometric TiC but not TiN [25]. The strong dependence on composition and stoichiometry has implications not only for the thermodynamics but also for the blast furnace. The surface energy could determine the ability of Ti(C,N) to either adhere to graphite or to determine the rate of crystal growth.

The thermodynamic stability of Ti(C,N) in liquid Fe has implications for performance in the BF. A solid solution of TiC and TiN is the thermodynamically favorable form in the blast furnace, and the formation of pure TiC within the conditions of the blast furnace is unlikely due to the prevailing 1 atm p_{N_2} [26]. The solubility of [Ti] in liquid predicted by FactSage 8.1 is shown in Figure 3.3. More [Ti] is needed to reach TiC saturation compared to TiN or Ti(C,N). At temperatures above 1300 °C, the solubility of Ti(C,N) and TiN start to diverge, with this difference increasing with temperature

increase. It has been experimentally confirmed that Ti(C,N) is the stable form: crystals formed in high-temperature confocal scanning laser microscopy experiments were determined to be the solid solution when both [C] and [N] were present in the Fe-C_{sat} melt [27]. The equilibrium composition of Ti(C,N) will vary with temperature. The equilibrium composition can be calculated by Eq. 1, where x_{TiC} is the mole fraction of TiC, p_{N_2} is the partial pressure of N_2 in atmospheres, and T is the temperature in K [26]. As p_{N_2} increases, a higher fraction of TiN is expected. This calculation of composition is compared to that predicted by FactSage and Thermo-Calc in Figure 3.4. Thermo-Calc and FactSage predicted similar amounts of TiC in the solid solution compared to Datta.

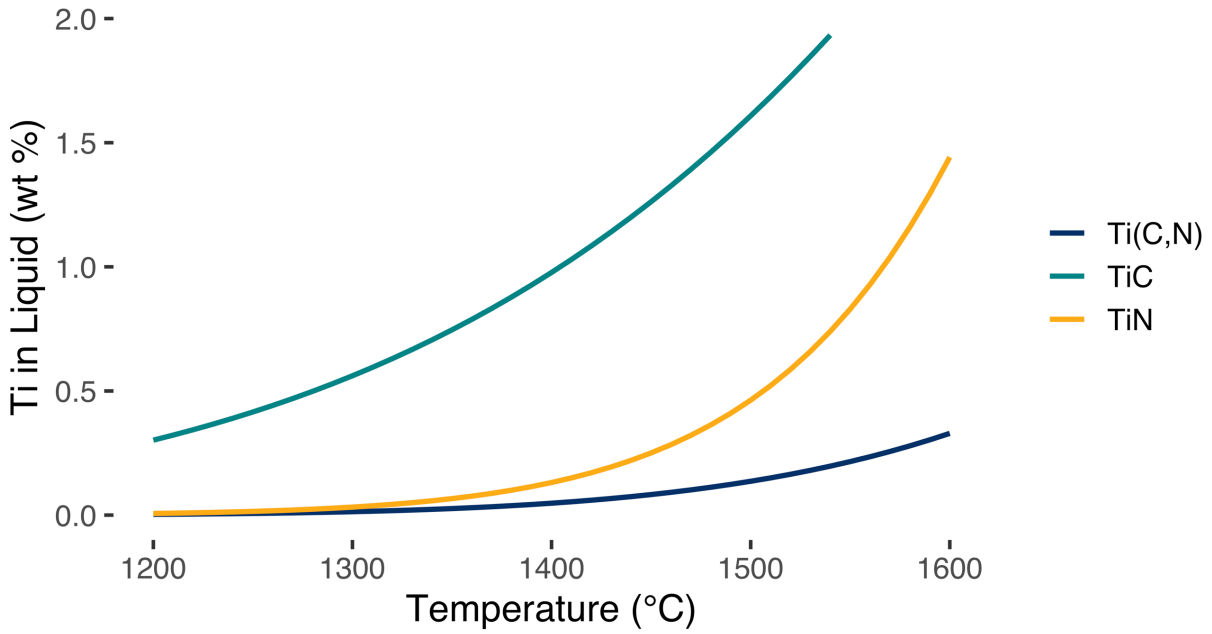

Figure 3.3. Solubility of [Ti] in liquid Fe-C_{sat}-N_{sat} at 1 atm N_2 calculated with FactSage FSstel 8.1.

$$x_{TiC} = \left(1 + p_{N_2}^{0.5} * 10^{\frac{7781}{T} - 4.11}\right)^{-1} \qquad \text{Eq. 1}$$

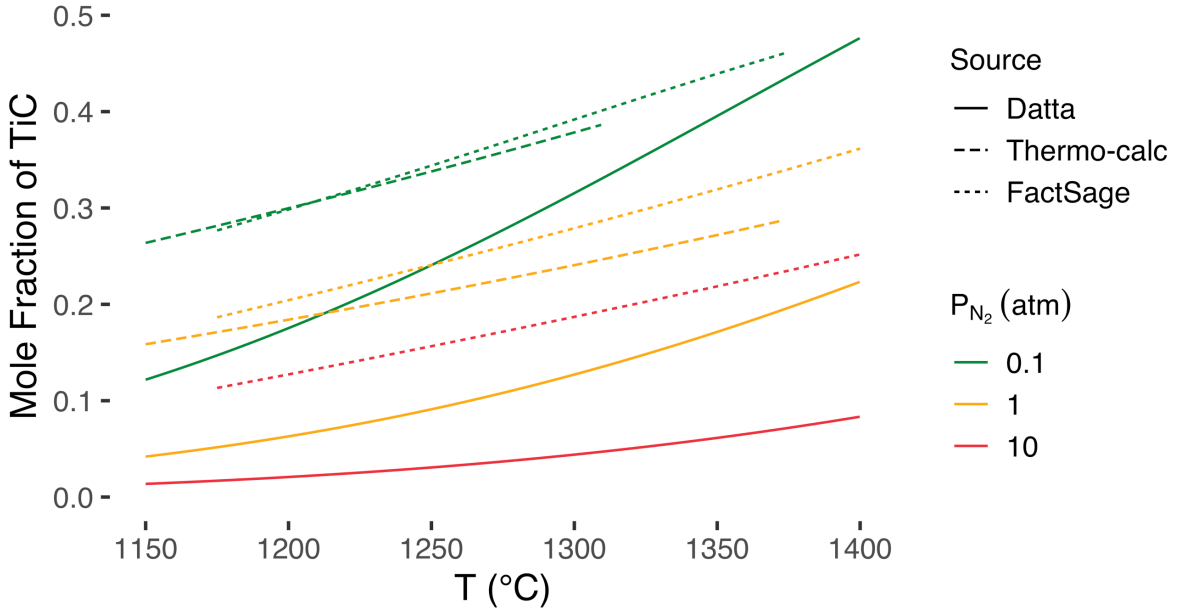

Figure 3.4. Predicted equilibrium composition of Ti(C,N) from Datta [26], Thermo-Calc, and FactSage. Lines from Thermo-Calc extend for the stability range of the carbonitride in liquid HM with the stated p_{N_2}. Thermo-Calc results were calculated with TCFE11 with 0.1% Ti, 0.1% N, 5% C by weight. FactSage results were calculated with FSstel 8.1 in the same way.

At a high pressure of N_2 (1 atm or higher), these results predict that Ti(C,N) will be N-rich at most temperatures. However, Ti(C,N) found within the BF are more complex. Dissected furnaces show Ti(C,N) particles with ring-like structures and colors that indicate different C:N ratios [28,29]. These structures were not in equilibrium and, much like tree rings, could indicate composition fluctuations within the HM. The composition of one of these rings within a Ti(C,N) particle is quite stable. Kang heated $Ti(C_x,N_y)$ pellets under vacuum at 1500 °C and saw little change in composition over 5 hours. The lack of a change was attributed to the small diffusivity of C and N atoms in the stoichiometric crystal [30]. Furthermore, the carbonitrides within the BF have been seen to grow non-classically, i.e., rather than growing atom by atom, the crystal grows by alignment and sintering of Ti(C,N) nanoparticles [29].

3.1.4 Published Thermodynamic Models

A discussion of thermodynamic models will begin with the ternary Ti-C-N system. This was modeled by Frisk et al. who, with three ternary parameters, was able to accurately reflect experimental data of the Ti(C,N) and predict the molar volume of the species [31]. Kang presented a deviation from ideality in the solid solution, but this was based on experimental results that did not reach equilibrium [30].

Jonsson built on the body of literature to combine the ternary Fe-Ti-C and Fe-Ti-N systems to into a model of the quaternary system [32]. This was improved upon by Lee which appears to be the basis of the model used by Thermo-Calc to calculate the Fe rich region of the system [33]. The important region for this work is the Fe-rich, C-saturated, and N-saturated region. The notable experimental bases for this region are shown in Table 3.1.

Table 3.1. Experimental Bases for Jonsson Fe-C-Ti-N thermodynamic model [32].

Finding	**Reference**
Change in the Fe-C eutectic with [Ti]	Magnin and Kurz [34]
Solubility of TiC in Fe-C_{sat}	Sumito et al. [35]
Solubility of TiN_x in liquid iron	Morovov et al. [36]
Nitrogen solubility in liquid Fe-Ti	Morita and Kunisada [37]
TiN_x solubility in Fe-N-Ti	Evans and Pehlke [38]
Solubility limit of specific compositions of Ti(C,N) in Fe-C-N	Ozturk and Fruehan [39]

Jonsson's model produced adequate agreement with the experimental results overall but deviated in a few areas, specifically overestimating the solubility of TiN and underestimating the solubility of $Ti(C_{.05}, N_{.95})$ [32]. Unfortunately, this region that disagreed with experimental data is the region of interest for this work.

Due to the problems (noted earlier) in the Fe-C and Fe-C-N systems from Thermo-Calc, FactSage 8.1 was used for thermodynamic predictions. Figure 4.5 shows the isothermal sections at 1500 °C of two pseudo-ternary phase diagrams.

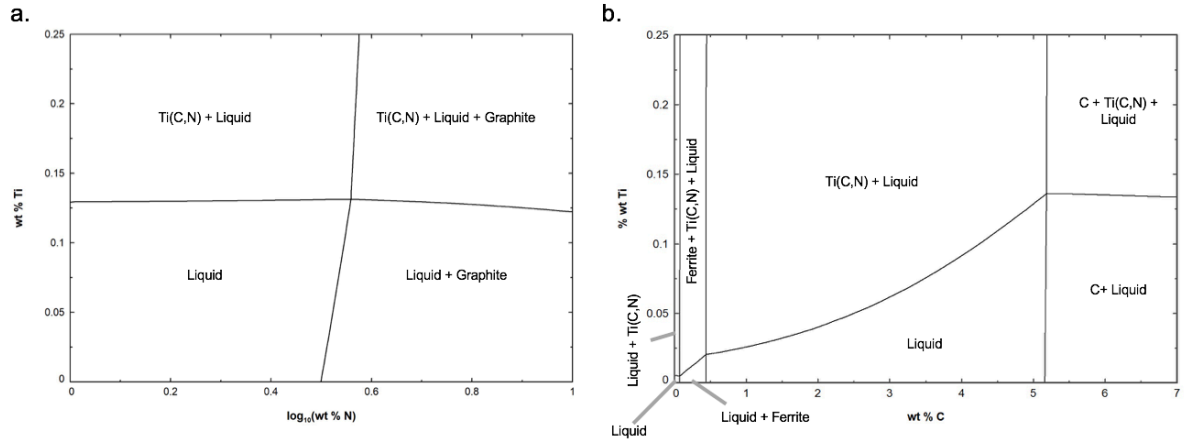

Figure 3.5. Pseudo-quaternary phase diagrams of the Fe-C-Ti-N systems at 1500 °C. a.) phase diagram with Ti and N composition variable. b.) phase diagram with Ti and C composition variable. For both diagrams, N_2 was stable in all regions.

3.1.5 Slag and the influence of other elements

While many thermodynamic models research only the ternary or quaternary system, the blast furnace introduces many more elements than the four discussed. When discussing hearth wear, the most important secondary elements are sulfur and silicon. Dissolved sulfur is important for the effect on dissolution: Wu and Sahajwalla saw a decrease in reaction rate as the sulfur dissolved in iron increased from zero to over 1% when dissolving carbonaceous materials (graphite and coal chars) [40]. However, Deng et al. saw an increase in rate with [S] increases in a near saturated melt ($\Delta C = 0.5\%$ wt) that included [Ti] [41]. Deng attributed this to a decrease in liquid surface tension, increasing the ability of the HM to wet graphite [41]. Wu and Sahajwalla suggested that [S] decreases the diffusion of C within the melt and that S causes surface blockage, limiting the dissolution rate [40].

Industrial publications have shown a positive correlation between [Si] and [Ti] in the HM [42]. Considering only the metal, Thermo-Calc and FactSage predict increasing [Si] decreases slightly [Ti] for a given Ti activity. This implies a positive interaction coefficient between Ti and Si. In contrast, Do et al. reported a small negative interaction parameter of e_{Ti}^{Si} [43], a different sign from some previously reported values [44,45], but with a very small effect on the solubility product [%Ti][%N] at TiN saturation. The industrial correlation is due to the slag-metal reactions rather than an oversight in thermodynamics. Industrial trials show a dependence of the partitioning of Ti on the partitioning of Si [42,46]. However, controlling Si content remains one of the biggest challenges of the BF [47].

3.1.6 Industrial Application of Thermodynamics

Though more complex thermodynamics have been studied for predicting the stability of inclusions in Ti-containing steels [39], the literature discussing Ti effects in the BF often utilize an Fe system that is saturated with N and C while varying Ti. Industrial reports use the results of Li et al. for predicting Ti(C,N) formation [27]. Despite those results being based on precipitation temperatures rather than true equilibrium experiments, the results correlate well with operator practice within the blast furnace, i.e., having HM with at least 0.07% wt Ti in the hot metal has been seen to improve the hearth refractory condition.

3.2 Evolution of Blast Furnace Hearth Refractory

One of the greatest improvements in blast furnace (BF) hearth life was changing the hearth material from chamotte bricks (an alumina-silicate mix) to carbonaceous bricks. This, along with operational improvements, contributed to the extension of campaign lives. Campaigns were reported to be around 6 years in the 1960s [48], 9-11 years in 1980 [48,49], and between 15-23 years for campaigns starting in the mid-1990s [50]. Even after the introduction of carbon blocks to the hearth, improvements in the processing of refractories have continued to enhance wear resistance, particularly through an increase in thermal conductivity. In 1965, Nippon Steel modified carbon refractory used in EAF furnaces for the BF, targeting a campaign life of 10 years [51]. The target life increased to 15 years through the development of hot pressing and Si-based binders which limited pore size and therefore reduced iron infiltration. Further improvements were made to thermal conductivity through semi-graphitization and micropore processing with campaign life estimate as 25 years [52]. Hearths today are designed with wall thicknesses between 3-5 m at the start of the campaign [53]. Despite this evolution, the refractory condition remains the major limitation of campaign life with a rebuild of the hearth requiring a multiple months of downtime [54,55].

The improvement in campaign life has not happened without operational adjustments. A higher thermal conductivity of the hearth lining allows better temperature control but must be properly utilized to protect the refractory. Current operator practice is to solidify an iron "skull" on the hot face of the refractory, eliminating the contact of liquid iron with the refractory [56]. The high thermal conductivity refractory allows more heat to be extracted, solidifying a skull (below 1150 °C, the eutectic temperature in the Fe-C system) while the bulk liquid is still near 1500 °C. Even if the skull is not formed, a lower temperature decreases the solubility of carbon in the hyper-eutectic region of the Fe-C phase diagram, lowering the driving force for refractory dissolution.

3.3 Mechanisms of Hearth Deterioration

The complexity of the blast furnace means refractory can deteriorate in a number of ways. These include attack by vapor impurities (alkali and zinc), oxidation, penetration by hot metal (HM), and chemical dissolution [52,57]. Excluding dissolution, these degradations happen when a gas or liquid species infiltrates the refractory pores [58]. The result of these attacks is a "brittle zone" near the hot face: a zone that is not well adhered to the bulk refractory. At best this zone is still structurally sound but with

reduced the thermal conductivity; at worst this results in the brittle zone spalling off, exposing fresh refractory [59]. Carbon refractories with higher impurity concentrations are more susceptible to oxidation and alkali attack, the later due to the reaction of alkalis with impurities to form phases that expand on solidification [60].

3.3.1 Dissolution of Carbon

Many of the hearth wear mechanisms can be limited by reducing pore size and pore connectivity within the refractory [58]. Dissolution of refractory by HM undersaturated in carbon is the exception to this. The problem is apparent: liquid iron – which can dissolve carbon - is in contact with carbon. The wear of hearth refractory is normally well controlled (3-10 mm/month [61]) by operational practice and monitoring of the hearth. This is an average over the campaign life; industrial reports often show "wear events" where the hearth deteriorates quickly rather than a constant, slow decline in thickness [62–64]. Wear events caused by dissolution can happen when HM that is undersaturated is carbon-possibly due to a lack of carbon pickup from a clogged deadman [65]- contacts the hot face of refractory, dissolving carbon until saturated. For graphite, this dissolution process is often mass transfer controlled; that is, the dissolution rate is limited by the speed at which [C] can be removed from the diffusion boundary layer. This means limiting flow near refractory walls is paramount to protecting the hearth. Carbon refractory is not simply pure graphite, however. Amorphous forms of carbon like anthracites and cokes have been seen to dissolve at slower rates, thought to be due to the higher activation energy needed to overcome the sp^3 bonds of amorphous carbons [40,57,66,67]. This effect was not proven without other studies [68,69] because many naturally occurring carbons have a high content of inorganic material ("ash"), which was seen to accumulate on the interface between the refractory and liquid metal and further slow the dissolution. Once enough ash has been accumulated, the dissolution becomes controlled by a mix of interfacially limited and mass transfer limited kinetics [66].

3.4 Industrial Practice in the Hearth

3.4.1 Selection of Hearth Refractory

While there is still some debate on what style of brick to use, a semi-graphitized supermicropore block is often the choice for the hot face [52]. Hot-face brick selection is a compromise: pure graphite bricks have the highest thermal conductivity but are expected to dissolve the fastest. Amorphous carbons are lower in thermal conductivity but have the double advantage of a higher activation energy (limiting dissolution) and

having a higher ash content that limits the interfacial area. “Semi-graphitized” carbon contains both binder and particles that are non-graphitic and are heat-treated at temperatures below the graphite transition temperature [70]. This provides a compromise between the higher thermal conductivity of graphite and the resistance to the dissolution of amorphous carbons. Supermicropore bricks should have average pore diameter less than 1 μm [52]. Note that “semi-graphitized” is different from “semigraphite;” the latter is comprised of graphite particles that are mixed with non-graphitic carbon binders [70].

The same refractory materials can be implemented in a variety of ways. Carbonaceous refractories are available in small bricks (around 1 m long and 0.25 m tall) or larger blocks (around 0.5 m tall and 2-4 m long), and both are used [53]. Large bricks need less grout and are less labor-intensive to replace but are more likely to crack from stress. Many furnaces use a mixture of materials for the hearth, such as an anthracitic carbon at the hot face with the more conductive graphite behind or even use a ceramic cup on the hot face [70]. Examples of hearth designs are shown in Figure 3.6 [53]. Some authors take issue with using a ceramic cup, due in part to the susceptibility of ceramic to thermal shock and because the inclusion of a ceramic with low thermal conductivity is in direct opposition to the current practice of solidifying an iron skull [56]. The ceramic cup is considered sacrificial with a predicted life of 3-5 years [53]. Sacrificial firebrick layers are also use for protection during blow-in, protecting carbon refractory until steady state is reached, but these layers readily crack and are low quality, meant to temporarily protect the hearth [56]. Should a longer term ceramic solution be desired, Dzermejko recommended using a sol-gel castable refractory for labor and cost efficiency (pumped rather than laid as bricks), completeness in coverage (liquid state provides a seamless layer), chemical stability (no calcium aluminates), and a reduced minimum refractory thickness required compared to ceramic bricks [56,71]. A thinner refractory has a lower thermal resistance, making it compatible with the operational practice of forming a skull. Some companies also have proprietary methods of brick processing. Nippon steel reported the use of refractory developed in-house which included a surface layer of TiC meant to reduce wear of the refractory hot face [72]. Current reports estimate a better performance than bricks not doped with Ti [51].

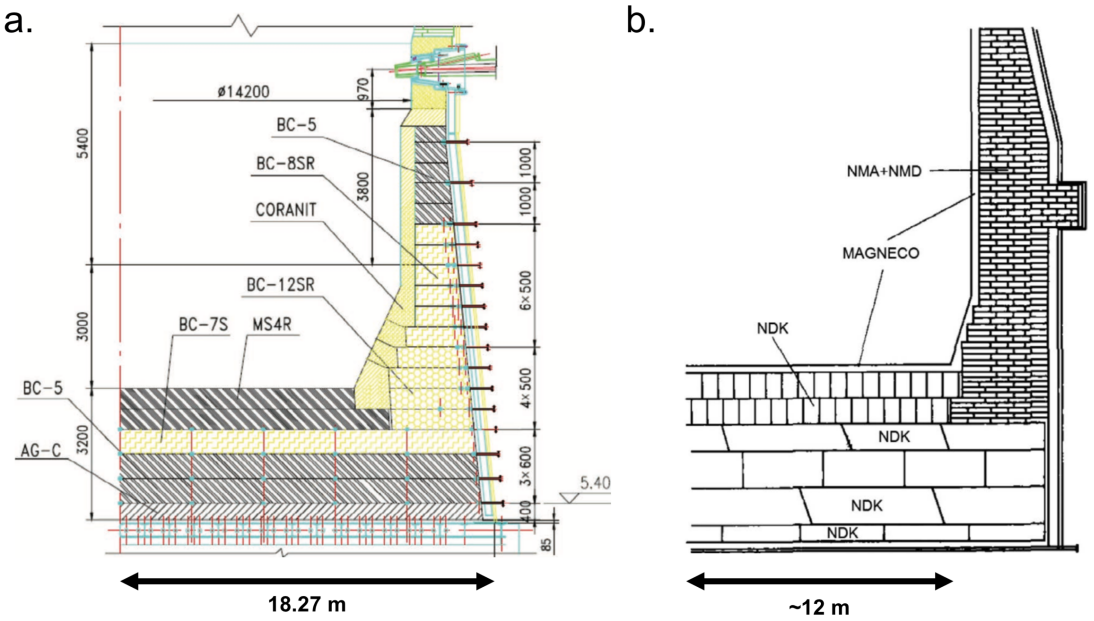

Figure 3.6. Industrial Hearth Designs. a). design with large carbon blocks and ceramic cup. b). design with smaller carbon bricks and sol-gel layer. Figure adapted from [53].

3.4.2 Modeling of Blast Furnace Phenomena

Though the blast furnace has historically been a black box, there has been much work on modeling the phenomena within. A complete understanding requires simulations at multiple length scales, from chemical interfacial phenomena at the meso-scale to computational fluid dynamics (CFD) models at the macro-scale [73]. Even within CFD models, the complexity is such that models often focus on a single region of the BF, for example, the stress and velocity of particles in the belly and bosh [74–76] or the shape of the raceway [73]. Some authors have developed more complex models by feeding the results of one type of simulation as the starting conditions for another [77]. Nevertheless, combined models are not usually needed to understand the condition of the hearth; it is enough to use the furnace productivity (in kg/s) as an outlet boundary condition for the taphole and to implement the iron-slag interface as an inlet at an equal mass flow rate [78]. Many authors have developed CFD models to answer different questions about hearth phenomena, including:

- Normal stress and shear stress in the hearth [79]
- Conditions of the slag-HM interface during tapping [80,81]
- Flow patterns within the hearth during tapping [82]
- The necessity of convective effects when modeling hearth flow [78]
- Prediction of refractory and skull thickness [83–85]
- Influence of permeability and position of the deadman on flow [86–88]

- Estimating the region of Ti scaffolding [89–91]

The last two investigations are of particular importance for this work. The former gives quantitative insight into how the deadman's position or porosity can affect the hearth wear. It is agreed upon that a clogged deadman both reduces carbon pickup from the deadman and promotes higher circumferential velocities, both detrimental to the hearth [76,86–88]. When the deadman floats, a "coke-free zone" is present between the deadman and the hearth. This allows HM to flow unimpeded near the hearth, and greater dissolution occurs due to the higher velocity [87].

3.4.3 Industrial Use of Titanium

Ilmenite is a ferrotitanium ore charged into the blast furnace as a way to prevent and correct hearth wear [42]. Papers as early as 1962 report the beneficial effects of Ti within the BF [92]. Narita observed large Ti(C,N) crystals embedded in chamotte bricks taken from dissected blast furnace as far back as the 1970s. These crystals were thought to have increased the refractory life. Solidified iron with embedded Ti(C,N) has since been reported in a number of other dissected furnaces [29,93–95]. There are also many reports that Ti additions do indeed increase the wear life, both as a preventative and reactionary measure [28,51,62,63,96]. The widely accepted mechanism of Bergsma and Fruehan can be found in the Introduction [46].

3.4.3.1 Charging Titanium to the Furnace

There is no established way to introduce Ti to the furnace. Street reports seven ways to add Ti to the furnace [42]. These include variations on charge material (metallic Ti, ferrotitanium ore, or titanium ore) and location (charging the bell, injecting at the tuyere, or adding to refractory). Ch. 7 includes more discussion of the location of additions.

The amount and schedule of Ti-bearing materials is also not established. Each plant has its own practice. For the case study contained in the Ch. 2, Huo et al. added only 3-5 kg Ti per net ton of hot metal (NTHM). At AK Steel Dearborn Works, ilmenite (ferrotitanium ore) was charged at 90 lb/NTHM (~28 lb Ti/NTHM) but only 4-6 times a day [42]. If the problem progressed, 15-20 lb ilmenite/NTHM was constantly charged. Entwistle et al. at followed this procedure at USS Gary Works, to good success [63]. Korthas et al. reported a charge practice of 3-5 kg Ti/NTHM, maintained by charging titano-hematite [97]. Regardless of the charge practice, many North American producers strive to achieve 0.07-0.15% [Ti] to see benefits [42,63,98].

3.4.3.2 Industrial Challenges when Charging Titanium

Thus far, only the benefits of Ti additions have been presented, but historically, use of ferrotitanium ores was limited due to issues caused by high [Ti]. Street reported that a large reason for the failure of the Adirondack Iron and Steel Company in New York State was due to the high Ti content in ferrous ores [96]. Ti, whether dissolved in metal as [Ti] or dissolved in slag as (TiO_2), can increase the viscosity of the respective medium, and operating conditions must change to account for this. The downstream processes are particularly sensitive to this. Higher titanium contents can introduce problems in steelmaking: steelmaking shops prefer less than 0.07% wt Ti, with a maximum of 0.16-0.2% [42]. High [Ti] contents in pig iron can lead to TiN particles in the steel melts which are thought to clog tundish nozzles [99]. TiO_2 in the ladle slag increases the solubility of MgO [96], leading to increased wear of ladle refractory. This is in addition to problems with hot metal desulfurization, thought to be due to precipitated TiN or perovskites forming a "crusty" slag [100]. The other downstream buyer, cement companies, who receive BF slag have limits to the amount of TiO_2 in the slag, normally between 1-3% wt for hydrodynamic reasons [42].

There are industrially established practices to help the operator control the Ti content in slag and HM. The dissolved (TiO_2) in the slag can be kept low by increasing slag basicity or increasing [Si] [42]; this would increase [Ti] in the hot metal. HM chemistry can also be controlled though metal temperature and by minimizing the amount of Ti-bearing ore charged. One of the advantages to localizing Ti charges near areas of wear is to provide protection where needed rather than introducing Ti to the entire furnace.

3.5 References

[1] B. Terry and X. Yu: *Ironmak. Steelmak.*, 1991, vol. 18, pp. 27–32.
[2] J. Robertson: *Adv. Phys.*, 1986, vol. 35, pp. 317–74.
[3] P. Harris and S. Tsang: *Philos. Mag. A*, 1997, vol. 76, pp. 667–77.
[4] K. Jurkiewicz, S. Duber, H.E. Fischer, and A. Burian: *J. Appl. Crystallogr.*, 2017, vol. 50, pp. 36–48.
[5] H. Ahmed: *Minerals*, 2018, vol. 8, pp. 1–20.
[6] K. Li, R. Khanna, J. Zhang, Z. Liu, V. Sahajwalla, T. Yang, and D. Kong: *Fuel*, 2014, vol. 133, pp. 194–215.
[7] J.A. Kitchener, J.O. Bockris, and D.A. Spratt: *Trans. Faraday Soc.*, 1952, vol. 48, pp. 608–17.
[8] Y. Nakagawa, K. Suzuki, and M. Fukumoto: *Trans. Japan Inst. Met.*, 1966, vol. 7, pp. 23–31.
[9] J. Chipman: *Met Trans*, 1970, vol. 1, pp. 2163–8.
[10] F. Neumann, H. Schenck, and W. Patterson: *Giesserei*, 1960, vol. 47, pp. 25–32.
[11] P. Gustafson: *Scand. J. Met.*, 1985, vol. 14, pp. 259–67.
[12] C.W. Bale, E. Bélisle, P. Chartrand, S.A. Decterov, G. Eriksson, A.E. Gheribi, K. Hack, I.H.

Jung, Y.B. Kang, J. Melançon, A.D. Pelton, S. Petersen, C. Robelin, J. Sangster, P. Spencer, and M.-A. Van Ende: *Calphad*, 2016, 54, vol. 54.
[13] J.-O. Andersson, T. Helander, L. Höglund, P. Shi, and B. Sundman: *Calphad*, 2002, vol. 26, pp. 273–312.
[14] A. Svyazhin, V. Kindop, and T. El Gammal: *Mater. Sci. Forum*, 1999, vol. 318, pp. 81–8.
[15] O. Opravil and R. Pehlke: *Am. Foundry Soc. Trans.*, 1969, vol. 77, p. 415.
[16] M. Uda and R. Pehlke: *Cast Met. Res. J.*, 1974, vol. 10, p. 14.
[17] E. Chen, S. Wang, Y. Dong, B. Wu, and Y. Zhou: *J. Iron Steel Res. Int.*, 2007, vol. 14, pp. 21–4.
[18] F. Tsukihashi, E. Oktay, and R.J. Fruehan: *Metall. Mater. Trans. B*, 1986, vol. 17, pp. 541–5.
[19] M. Miyamoto and T. Onoye: *ISIJ Int.*, 1992, vol. 32, pp. 76–80.
[20] J. Jang, K. Do-Hyeong, M. Paek, and P. Jong-Jin: *ISIJ Int.*, 2018, vol. 58, pp. 1185–90.
[21] K. Frisk: *Calphad Comput. Coupling Phase Diagrams Thermochem.*, 2008, vol. 32, pp. 326–37.
[22] V. Ivanchenko and Materials Science International Team: *C-N-Ti Ternary Phase Diagram Evaluation*, in Springer Materials.
[23] P. Xiao and B. Derby: *Acta Mater.*, 1996, vol. 44, pp. 307–14.
[24] H. Okamoto: *J. Phase Equilibria*, 1998, vol. 19, p. 89.
[25] P. Alvaredo, M. Dios, B. Ferrari, and E. Gordo: *J. Alloys Compd.*, 2019, vol. 770, pp. 17–25.
[26] K. Datta, P. Sen, S. Gupta, and A. Chatterjee: *Steel Res.*, 1993, vol. 64, pp. 232–8.
[27] Y. Li, Y. Li, and R.J. Fruehan: *ISIJ Int.*, 2001, vol. 41, pp. 1417–22.
[28] K. Narita, M. Maekawa, T. Onoye, Y. Satoh, and M. Miyamoto: *Trans. Iron Steel Inst. Jpn.*, 1977, vol. 17, pp. 459–68.
[29] C. Wang, K. Jiao, J. Zhang, and S. Wu: *ISIJ Int.*, 2021, vol. 61, pp. 138–45.
[30] S. Kang: *Powder Metall.*, 1997, vol. 40, pp. 139–42.
[31] K. Frisk, J. Zackrisson, B. Jansson, and A. Markström: *Zeitschrift für Met.*, 2004, vol. 95, pp. 987–92.
[32] S. Jonsson: *Metall. Mater. Trans. B*, 1998, vol. 29, pp. 371–84.
[33] B.J. Lee: *Metall. Mater. Trans. A*, 2001, vol. 32, pp. 2423–39.
[34] P. Magnin and W. Kurz: *Metall. Trans. A, Phys. Metall. Mater. Sci.*, 1988, vol. 19 A, pp. 1955–63.
[35] M. Sumito, N. Tsuchiya, K. Okabe, and K. Sanbongi: *Trans. Iron Steel Inst. Japan*, 1981, vol. 21, pp. 414–21.
[36] A.N. Morozov, V.F. Isaev, and L.G. Korolev: *Izv. Akad. Nauk SSSR, Met. i Gorn. Delo*, 1963, vol. 4, pp. 141–4.
[37] Z. Morita and K. Kunisada: *Trans. Iron Steel Inst. Japan*, 1978, vol. 18, pp. 648–54.
[38] D.B. Evans and R.D. Pehlke: *Trans. Met. Soc. AIME,* vol. 233, 1965.
[39] B. Ozturk and R.J. Fruehan: *Metall. Mater. Trans. B*, 1990, vol. 21B, pp. 879–84.
[40] C. Wu and V. Sahajwalla: *Metall. Mater. Trans. B*, 2000, vol. 31B, pp. 243–51.
[41] Y. Deng, J. Zhang, K. Jiao, and Z. Liu: *ISIJ Int.*, 2019, vol. 59, pp. 1–8.
[42] S. Street, A. Cheng, and I. Cameron: in *AISTech Proceedings*, 2019, pp. 275–88.
[43] K.H. Do, J.M. Jang, H.S. Son, M.K. Paek, and J.J. Pak: *ISIJ Int.*, 2018, vol. 58, pp. 1437–42.
[44] M. Ohta and K. Morita: *ISIJ Int.*, 2003, vol. 43, pp. 256–8.
[45] G.I. Batalin and V.S. Sudavtsova: *Sov. Prog. Chem,* 1976, vol. 9, p. 93.
[46] D. Bergsma and R.J. Fruehan: *60th Ironmak. Conf. Proc.*, 2001, pp. 297–312.
[47] T.I. and S.I. of Japan: *Blast Furnace Phenomena and Modelling*, Springer Netherlands, Dordrecht, 1987.
[48] K. Kobayashi, T. Matsumoto, and K. Yanagisawa: *Kawasaki Steel Giho*, 1993, vol. 25, pp. 258–65.

[49] W. Hartig, D. Amirzadeh-Asl, and D. Fünders: in *AISTech Proceedings*, 2012.
[50] S. Filatov, I.F. Kurunov, Y. Gordon, A. Sadri, and W. Ying: *AISTech Proc.*, 2016, pp. 695–704.
[51] M. Nitta and K. Hatakeyama: *Nippon Steel Tech. Rep.*, 2020, pp. 40–4.
[52] S. Biswas and D. Sarkar: in *Introduction to Refractories for Iron- and Steelmaking*, 2020, pp. 147–218.
[53] Z.J. Liu, J.L. Zhang, H. Bin Zuo, and T.J. Yang: *ISIJ Int.*, 2012, vol. 52, pp. 1713–23.
[54] L. Keyl: *NLMK And Paul Wurth Accomplish Major Blast Furnace Reline Successfully*, 2019.
[55] V. Vogl, O. Olsson, and B. Nykvist: *Joule*, 2021, vol. 5, pp. 2646–62.
[56] A. Dzermejko: *Iron Steel Technol.*, 2014, vol. 11, 3 (March), pp. 41–56.
[57] S. Silva, F. Vernilli, S. Justus, O. Marques, A. Mazine, J. Baldo, E. Longo, and J. Varela: *Ironmak. Steelmak.*, 2005, vol. 32, pp. 459–67.
[58] J. Stec, R. Smulski, S. Nagy, K. Szyszkiewicz-Warzecha, J. Tomala, and R. Filipek: *Ceram. Int.*, 2021, vol. 47, pp. 16538–46.
[59] A. Shinotake, H. Nakamura, N. Yadoumaru, Y. Morizane, and M. Meguro: *ISIJ Int.*, 2003, vol. 43, pp. 321–30.
[60] S. Silva, F. Vernilli, S. Justus, E. Longo, J. Baldo, J. Varela, and J. Lopes: *Mater. Corros.*, 2013, vol. 64, pp. 1032–8.
[61] S. Rao, R. Anand, L. Mallikarjun, L.R. Singh, Y. Gordon, M. Henstock, and W. Ying: in *AISTech Proceedings*, 2019, pp. 311–20.
[62] J. Huo and J. Huang: *Ironmak. (In Chinese)*, 2013, vol. 32, pp. 14–6.
[63] J.W. Entwistle, J. Grindey, R. Albanese, D. Lee, B. Rogers, T. Schrenk, M. McCoy, I. Cameron, M. Sukhram, M. Bodley, R. Midha, M. Al-Dojayli, K. Chomyn, Y. Ghobara, J. Busser, and P. Towsey: *Iron Steel Technol.*, 2020, vol. 17, 3 (March), pp. 64–74.
[64] Y. Zhao, D. Fu, L.W. Lherbier, Y. Chen, C.Q. Zhou, and J.G. Grindey: *Steel Res. Int.*, 2014, vol. 85, pp. 891–901.
[65] M. Chapman, R. Nightingale, and B. Monaghan: *CHEMECA 2011 Australas. Conf. Chem. Eng.*, 2011, pp. 1–14.
[66] D. Jang, Y. Kim, M. Shin, and J. Lee: *Metall. Mater. Trans. B*, 2012, vol. 43B, pp. 1308–14.
[67] X. Xing, S. Jahanshahi, J. Yang, and O. Ostrovski: *Arch. Mater. Sci. Eng.*, 2018, vol. 92, pp. 22–7.
[68] M. Sun, J. Zhang, K. Li, H. Li, Z. Wang, C. Jiang, S. Ren, L. Wang, and H. Zhang: *JOM*, 2020, vol. 72, pp. 2174–83.
[69] R. Wiblen, V. Sahajwalla, and C. Wu: *Ironmak. Conf. Proc.*, 2001, pp. 1005–13.
[70] A. Dzermejko: in *Refractories Handbook*, C. Schacht, ed., Marcel Dekker, New York, 2004, pp. 201–14.
[71] A.J. Dzermejko: *Iron Steel Technol.*, 2015, vol. 12, pp. 58–70.
[72] H. Inoue, M. Nitta, T. Matsui, T. Wakasa, Y. Yamagami, and T. Mochida: *United States Pat.*
[73] S. Kuang, Z. Li, and A. Yu: *Steel Res. Int.*, 2018, vol. 89, p. 1700071.
[74] A.T. Adema, Y. Yang, and R. Boom: *ISIJ Int.*, 2010, vol. 50, pp. 954–61.
[75] Z. Fan, S. Igarashi, S. Natsui, S. Ueda, T. Yang, and R. Inoue: *ISIJ Int.*, 2010, vol. 50, pp. 1406–12.
[76] K. Nakano, Y. Ujisawa, T. Inada, A. Oboso, and K. Katayama: *Nippon Steel Tech. Reprt*, 2020, pp. 109–18.
[77] L. Liu, B. Guo, S. Kuang, and A. Yu: *Metall. Mater. Trans. B*, 2020, vol. 51, pp. 2211–29.
[78] B.Y. Guo, D. Maldonado, P. Zulli, and A.B. Yu: *ISIJ Int.*, 2008, vol. 48, pp. 1676–85.
[79] L. Shao and H. Saxén: *Steel Res. Int.*, 2012, vol. 83, pp. 878–85.

[80] L. Shao and H. Saxén: *Steel Res. Int.*, 2012, vol. 83, pp. 197–204.
[81] W.B.U. Tanzil, P. Zulli, J.M. Burgess, and W. V. Pinczewski: *Trans. Iron Steel Inst. Japan*, 1984, vol. 24, pp. 197–205.
[82] W.T. Cheng, E.N. Huang, and S.W. Du: *Int. Commun. Heat Mass Transf.*, 2014, vol. 57, pp. 13–21.
[83] J. Brännbacka and H. Saxén: *Ind. Eng. Chem. Res.*, 2008, vol. 47, pp. 7793–801.
[84] M.F. Barbés-Fernández, E. Marinas-García, E. Brandaleze, R. Parra-Figueroa, L.F. Verdeja-González, G.A. Castillo-Rodriguez, and R. Colás: *ISIJ Int.*, 2008, vol. 48, pp. 134–40.
[85] Y. Kaymak, H. Bartusch, T. Hauck, J. Mernitz, H. Rausch, and R. Lin: *Steel Res. Int.*, 2020, vol. 91, p. 2000055.
[86] A. Preuer, J. Winter, and H. Hlebler: *Steel Res.*, 1992, vol. 63, pp. 139–46.
[87] K. Komiyama, B. Guo, H. Zughbi, P. Zulli, and A. Yu: *Metall. Mater. Trans. B*, 2014, vol. 45, pp. 1895–914.
[88] K. Shibata, Y. Kimura, M. Shimizu, and S. Inaba: *ISIJ Int.*, 1990, vol. 30, pp. 208–15.
[89] B. Guo, P. Zulli, D. Maldonado, and A. Yu: *Metall. Mater. Trans. B*, 2010, vol. 41, pp. 876–85.
[90] B.-Y. Guo, A.-B. Yu, P. Zulli, and D. Maldonado: *Steel Res. Int.*, 2011, vol. 82, pp. 579–86.
[91] K. Komiyama, B. Guo, H. Zughbi, P. Zulli, and A. Yu: *Steel Res. Int.*, 2015, vol. 86, pp. 592–603.
[92] Y. Jomoto, B. Eto, Y. Kanayama, Y. Okuno, and M. Isoyama: *Tetsu-to-Hagane (In Japanese)*, 1965, vol. 51, pp. 1713–22.
[93] L. Zhang, J. Zhang, K. Jiao, and C. Wang: *ISIJ Int.*, 2020, vol. 60, pp. 1655–61.
[94] K. Gao, K. Jiao, J. Zhang, L. Zhang, C. Wang, W. Gong, J. Zheng, and H. Zhang: *ISIJ Int.*, 2020, vol. 60, pp. 2385–91.
[95] V.A. Perepelitsyn, K.G. Zemlyanoi, K. V. Mironov, A.A. Forshev, F.P. Nikolaev, and D. V. Sushnikov: *Refract. Ind. Ceram.*, 2020, vol. 61, pp. 364–73.
[96] S. Street, C. Copeland, and E. Worral: in *AISTech Proceedings*, 2013, pp. 381–403.
[97] B. Korthas, J. Hunger, V. Pschebezin, J. Adam, G. Harp, S. Kallio, R. Hurme, J.-O. Wikström, P. Hahlin, S. Wiedner, and others: *Eur. Comm. Dir. Res. Innov.*, 2007, pp. 1–140.
[98] Y. Zhao: *Iron Steel Technol.*, 2014, vol. 11, pp. 95–103.
[99] P. Dorrer, S.K. Michelic, C. Bernhard, A. Penz, and R. Rössler: *Steel Res. Int.*, 2019, vol. 90, p. 1800635.
[100] S. Street, R.P. Stone, and P.J. Koros: *Iron Steel Technol.*, 2005, vol. 2, 11 (November), pp. 65–74.

4 Hypotheses Tested

Ch. 6 The formation of Ti(C,N) will decrease the dissolution rate of pure graphite 70% compared to a binary alloy and 30% compared to dissolved Ti alone.

Ch. 7 Doping coke analog coated graphite rods with 10% TiC will result in the formation of statistically significantly thicker solid iron shells, compared with undoped coatings or those containing Ti(C,N) or TiN.

Ch. 8 Liquid Fe-C_{sat} will not react with or wet glassy carbon. An angle of contact should be greater than 90°.

Ch. 10 The wetting of Alumina by Fe-C_{sat}-Ti can be prevented by coating the crucible in a thin layer of liquid flux. This should raise the angle of contact by at least 10°.

Ch. 11 The temperature gradient over the height of a liquid Fe sample contained in an MgO crucible is less than 3 K.

Ch. 11 The melting offset of pure metals in the CSLM is material dependent, and differs by more than 5 °C for pure metals that have melting points within 25 °C.

5 The Formation and Distribution of Ti(C,N) to Prevent Blast Furnace Refractory Wear

This chapter modified from its original form in the *Transactions of the AIST*:

T. Britt and P. C. Pistorius, "The Formation and Distribution of Ti(C,N) to Prevent Blast Furnace Refractory Wear," *AIST Trans.*, vol. 19, no. 5, Apr. 2022.
DOI: 10.33313/TR/0522.

5.1 Abstract

Titanium bearing ore has long been charged into blast furnaces to prevent carbonaceous refractory wear. Prevention is thought to be due to the formation of Ti(C,N) scaffolds which helps to promote iron solidification. Though Ti(C,N) has been investigated to some extent, little attention has been given to the differing properties of individual components. High temperature confocal scanning laser microscopy is used to qualitatively investigate the role of TiC and Ti(C,N) in preventing hearth wear. TiC and Ti(C,N) were seen to stop particle flow on the surface of molten iron and agglomerate in large clumps. Compared to TiC, Ti(C,N) scaffolds formed at higher temperatures and lower Ti contents and agglomerated more easily. In an *ex-situ* method, a coating of TiC sintered to graphite was seen to remain connected to the graphite crucible despite being in contact with molten iron undersaturated in Ti at 1550 °C. These observations are a first approximation to investigate how Ti additions protect the hearth.

5.2 Within the Narrative

The observations in this section, though qualitative, motivate much of the work completed. Seeing the ability of carbonitrides to agglomerate and form clusters, even so much as to anchor them on the surface of the molten bath, gives support to why Ti is uniquely able to protect refractory. Likewise, the persistence of TiC at the graphite interface despite metal being undersaturated in Ti supports the possibility that these compounds can bond to the refractory. There is a novelty to these results that prompted the investigations of the following chapters: if Ti(C,N) is so effective in coalescing, the protection of hearth refractory may be related to these observations.

5.3 Introduction

The charging of titanium-bearing ore in blast furnaces has long been known to prevent blast furnace (BF) hearth wear and to extend the campaign life of the BF [1–3]. Despite being "operationally effective" in protecting the furnace, much is still unknown about the exact mechanism of prevention. Narita et al. were the first to report Ti(C,N) crystals in the wall of a blown-out blast furnace with a chamotte brick hearth [2]. Since then, Bergsma and Fruehan hypothesized that Ti(C,N) forms in locations with less thermal resistance, i.e. where the refractory is thinner, and these particles protect the walls by restricting flow of liquid metal to the hot face [4]. This mechanism is described in depth in the introduction (Ch. 2) but is essentially a higher temperature variation on solidifying an iron skull. Wen et al. reported that the apparent solidus temperature of pig iron increased with Ti content [5]. This is an argument of fluidity, with the flow of metal decreasing as the solid fraction increases [6]. Typically, operational additions of titanium-bearing ore seek to obtain 0.07-0.15% wt Ti in hot metal (HM), which agrees with thermodynamic data on the conditions to form Ti(C,N) [7–9]. Zhao has proposed that the most important benefit of Ti additions is through viscosity increase [9]. The published version of this chapter presented Zhao's views as an alternative mechanism of protection to that of Bergsma and Fruehan [10]. Instead, we now view Zhao's focus on viscosity as compatible with Bergsma and Fruehan's mechanism: the increase in apparent viscosity provided by the formation of solid Ti(C,N) is vital to slowing the HM flow enough to extract heat for solidification.

The lack of clarity on the mechanism speaks to the limited laboratory work in literature. There are primarily two sources that studied interactions of carbonaceous material with Ti containing HM at the laboratory scale. Deng et al. dissolved rotating cylinders of hearth brick into HM [11]. Additions of 0.15% wt Ti (not enough to precipitate TiC) were seen to slow the erosion rate of the brick by half. However, this experiment falls short of testing the full mechanism, being both absent of Ti(C,N) and only considering dissolution. While the hearth does deteriorate through dissolution, how Ti additions may prevent dissolution in the BF as opposed to other mechanisms has not been established. Bergsma and Fruehan looked at the locations of Ti(C,N) after solidifying stagnant laboratory-scale melts, but the observed location of carbonitrides was influenced by buoyancy of Ti(C,N) [4]. Where Ti(C,N) accretions form in operation is an important question to the protection of the BF hearth. Zhao observed that Ti(C,N) was only found in cracks of the bottom lining at Edgar Thompson No. 1 (not on the sidewall) and questioned why Ti(C,N) would localize in a region of wear [8]. One reason Ti(C,N) might show a propensity to accumulate on the side wall is due to high surface energy. Wang observed that BF Ti(C,N) accretions were comprised of small

Ti(C,N) cubes which had sintered together to reduce the surface energy [12]. Likewise, it is possible that the carbonitrides would bond to the refractory to reduce surface energy. With this focus on surface energy, the composition of Ti(C,N) is important.

Ti(C,N) is a solid solution with either carbon or nitrogen atoms on the anion positions, but the properties (including surface energy) of the component phases differ widely [13,14]. Many liquid metals, including Fe, wet TiC extremely well (~30° contact angle) [15]. Yet liquid iron will not wet stoichiometric TiN [16]. Xiao and Derby observed that the wetting angle of liquid metals (Ag and Cu) differed by 10° between stoichiometric TiC and TiN and as much as 90° in non-stoichiometric TiC and TiN [17]. These variations in surface energy could affect how Ti(C,N) behaves in the BF.

To complicate matters, carbonitrides found within the BF are not of a single composition. Narita et al. performed EPMA on a particularly large Ti(C,N) polycrystal and saw rings of varying C:N ratios within the crystals [2]. TiN is much more thermodynamically stable (than TiC) under BF conditions, and by thermodynamic calculation is the main component within the solid solution [18]. While the EPMA results of Narita support a high N content, observed rings had more TiC than predicted [2]. The compositions of these rings appeared to be functions of when they formed, rather than equilibrium conditions. Possibly, Ti(C,N) of certain compositions protect the furnace due to the combination of surface energy and thermodynamic stability.

With all the hypotheticals presented above, a starting point is to study how TiC interacts with liquid Fe. The higher surface energy of TiC could be necessary to the protection of the refractory, despite its lower stability. Additionally, it was the compound Nippon Steel chose to add to hearth refractory to provide additional protection against wear [19]. Here, an *ex-situ* investigation (one in which data was obtained after the experiment concluded) is performed to test if a TiC layer can persist in the presence of buoyant, erosive, and dissolutive forces when in contact with liquid Fe undersaturated with Ti.

There is also incentive to isolate and study the thermodynamics of TiC. The results of Li, Li, and Fruehan are compared with those of Sumito et. al in Figure 5.1 [20,21]. The experiment of Sumito et al. was performed by sampling liquid metal for chemical analysis and is the basis for many of the thermodynamic models of TiC in iron [21,22]. Those results disagree with the ones by Li et al. by around 50 °C [20]. When considering that Li et al. performed the experiments by directly observing the precipitation of TiC (upon cooling) in a high temperature confocal scanning laser microscope (CSLM), the true equilibrium temperature should be even higher due to the undercooling needed to

precipitate observable solid particles in a liquid. While revisiting the TiC equilibrium experiments of Li et al. (Ch. 9), TiC particles were seen to interact in ways previously unreported in literature. The *in-situ* experiment, one in which data was obtained while the metal was at temperature, contains these results. The observed phenomenon is discussed as a possible contribution to the hypothesized mechanisms that Ti additions reduce BF hearth wear.

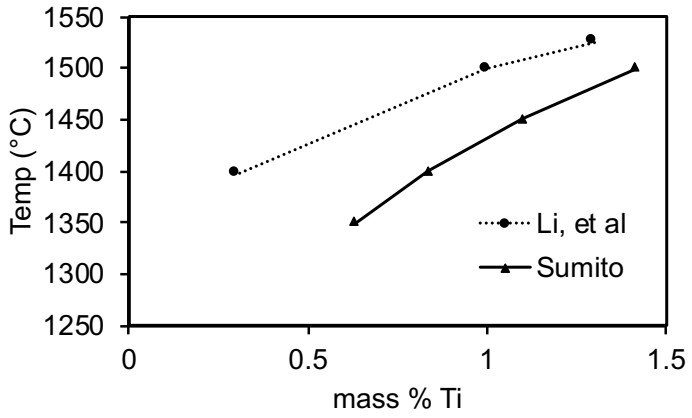

Figure 5.1. Comparison of TiC equilibrium literature [20,21], showing the reported TiC precipitation temperature in carbon-saturated iron.

5.4 Experimental

5.4.1 *Ex-Situ* Interface Experiments Layering TiC onto Graphite

TiC powder (0.012 g) was added to a graphite crucible (6.5mm OD x 4mm height x 0.5mm thickness). Isopropyl alcohol was used to fill the crucible, and the TiC was stirred into a slurry, to facilitate a more even coating. The graphite crucible was placed within an alumina crucible which was set onto a B-type thermocouple holder within the CSLM furnace. This step – to sinter a layer of TiC – was heated according to the "*ex-situ* sintering" parameters in Table 5.1 and Figure 5.2, and the alcohol was evaporated during this heating step. A further description of the CSLM is given in Ch. 11. The coating was sintered under Ar atmosphere with p_{O_2} less than 10^{-21} atm. The prepared crucible was examined visually to check that the coating covered the bottom surface completely. While adequate for a proof of concept, a more robust measurement is needed to quantify the coating thickness, and one such method is discussed in a later section.

Fe-C_{sat} was prepared by melting electrolytic iron in a graphite crucible with an induction furnace. After 10 minutes at 1550 °C the iron was sampled. A 0.19 g piece of the sampled iron was added to the graphite crucible with sintered TiC which was then placed within an alumina crucible and heated in the CSLM chamber under Ar atmosphere according to the "*ex-situ* metal experiment" column in Table 5.1 and Figure 5.2. Upon cooling, the sample was mounted vertically in epoxy with 7% wt Iodoform added to provide contrast [23] and polished to the estimated middle of the crucible. Images were taken with an FEI Quanta 600 and stitched to a single image using Adobe Photoshop CC.

5.4.2 *In-situ* Surface Observation Experiments

Carbon saturated iron of around 5.3% wt C was prepared as before, only here sampling after 5 minutes at 1550 °C. A bulk Fe-Ti alloy was prepared by mixing electrolytic iron and titanium sponge in an alumina crucible and melting in an induction furnace. The furnace was shut down soon after melting due to an air leak into the furnace. Because of the oxidation of Ti, the composition was determined by Oxford EDS on a polished section as 3.6% wt Ti.

Sections of the Fe-C_{sat} sampled alloy and the bulk Fe-Ti alloy were weighed and added to MgO crucibles (6 mm OD x 5 mm height x 1 mm thickness). These were initially heated under Ar atmosphere according to the "*in-situ* experiment" in Table 1 and Figure 5.2, but after ten minutes at 1550°C, the temperature was lowered by a hold function in 10 °C increments until TiC was visible. The temperature was again raised, watching for the TiC particles to dissolve at which point the temperature was again lowered until particles were visible. This was repeated three times on average. For experiments containing Ti(C,N), the method was largely the same, only switching to N_2 + 5% H_2 atmosphere at the upper temperature.

It should be noted that all temperatures shown in the heating profile are nominal. That is, the reported temperature is not corrected for the offset (approximately 20°C) between the measured temperature and the actual temperature within the crucible.

Table 5.1. Nominal Experimental Heating Parameters

Ex-situ Sintering			*Ex-situ* Metal Experiment			*In-situ* Experiment		
Temperature (°C)	Slope (°C/min)	Hold (sec)	Temperature (°C)	Slope (°C/min)	Hold (sec)	Temperature (°C)	Slope (°C/min)	Hold (sec)
300	50	60	300	50	60	300	50	60
1350	350	0	1350	400	0	1350	400	0
1560	100	300	1485	150	600	1550	100	600
20	-400	0	20	-400	0	Hold Function Controls		

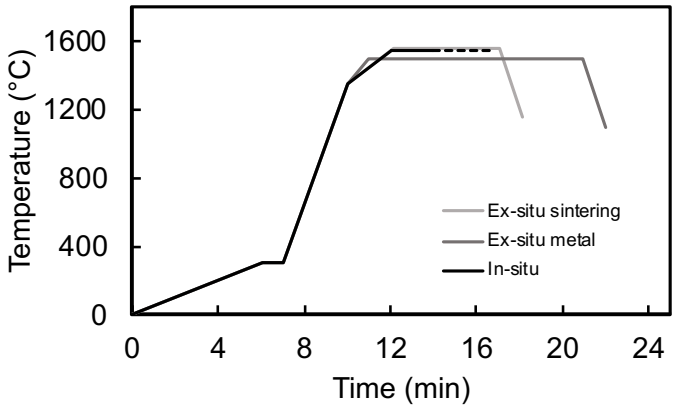

Figure 5.2. Nominal heating profile of the experiments. The dashed line of the *in-situ* experiment denotes the temperature was controlled manually for the remained of the experiment.

5.5 Results and Discussion

5.5.1 Discussion of *Ex-situ* experiments

The Bergsma-Fruehan mechanism requires that Ti(C,N) particles hold together near the graphite refractory. To be protective, the carbonitrides must stay near the refractory despite:

1. Being less dense than liquid iron
2. The metal being undersaturated in Ti
3. The erosive forces of the fluid flow

The CSLM was used to test if TiC particles are able to fulfill these requirements. Though often used only for *in-situ* experiments, the CSLM has advantages in certain experiments due to the ease of using smaller samples when coating and polishing is involved. However, the high surface-area to volume ratio of the small metal melt could be problematic. If the sintered layer disappears, further investigation will be required to definitively rule out this mechanism as the high surface area to volume ratio could have

an effect, but if a layer of TiC remains, it is credible that the layer could survive within a BF.

The resultant microstructure of the *ex-situ* interface experiment is shown in Figure 5.3, with the colored image showing the shadings of different regions. Near the bottom of the graphite crucible, a layer of TiC was present (shown in red) despite being well penetrated by iron. This region was not homogenous, and there were regions in the layer which lacked TiC (circled in green and magnified in Figure 5.4) in addition to the region at the right where the TiC layer was not seen. There was also primary graphite on top of the TiC layer suggesting that some of the TiC was indeed consumed, with the excess carbon precipitated as graphite upon solidification.

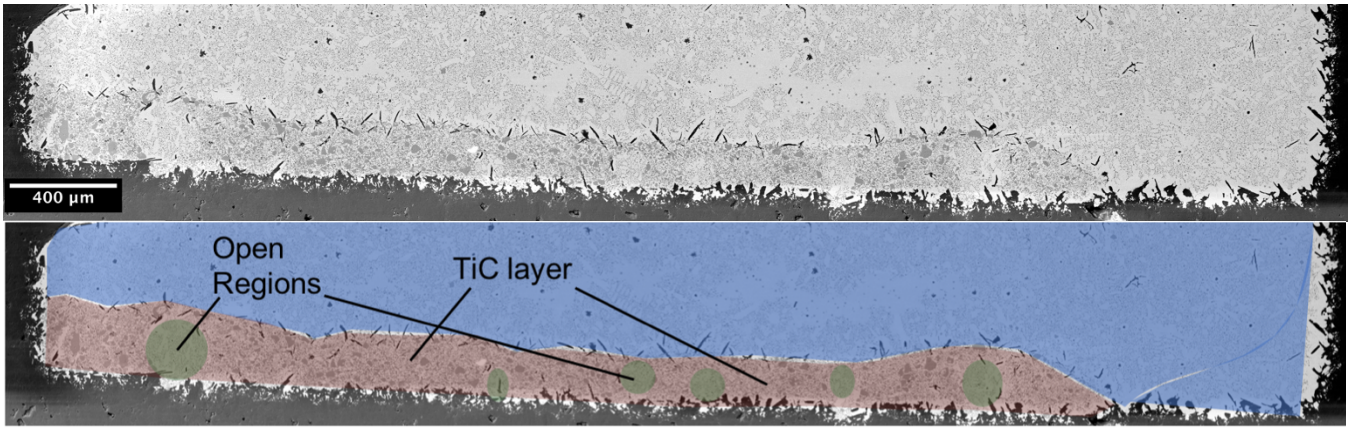

Figure 5.3. Scanning electron micrograph (backscattered electron image) of the TiC layer in iron at the bottom of a graphite crucible. Top: original image. Bottom: colored with red representing the TiC layer, green representing open regions within the TiC layer and blue representing regions outside of the TiC layer.

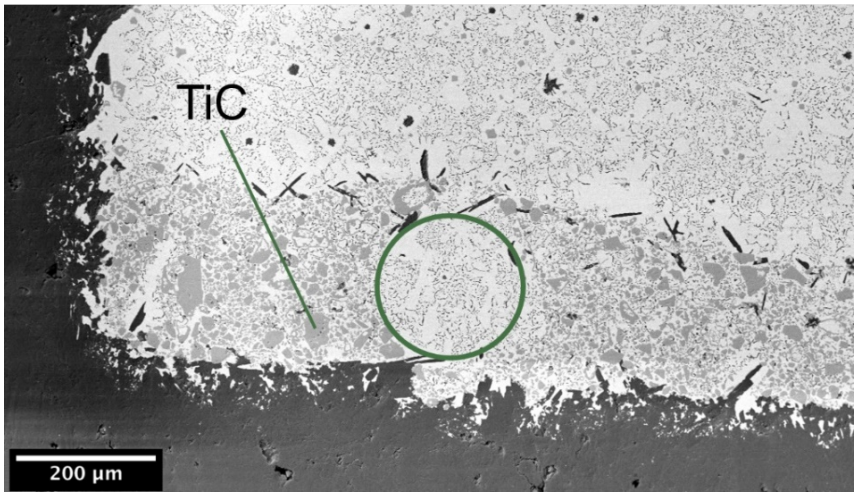

Figure 5.4. Higher magnification of a region lacking TiC (circled).

Though this experiment was only a first approximation, it does support the Bergsma-Fruehan mechanism. The most important finding is that the TiC remained as a layer

near the graphite and did not float to the surface nor disperse. The layer overall withstood the buoyant and erosive forces and the tendency to dissolve. Both irregular and equiaxed particles were found scattered through the bulk, the former characteristic of particles that were mechanically removed and the latter characteristic of dissolved Ti that reprecipitated into TiC upon solidification of the sample. A remaining question is why the gaps in the TiC layer form circular regions. This could be due to a pulse of metal undersaturated in carbon as evidenced by the lower graphite content within those regions, but more analysis must be attempted to eliminate inconsistencies in sintering.

While beneficial as a proof of concept, this method will need quantification in future experiments. One method is to use X-ray computed tomography (x-CT). x-CT provides a non-destructive method to view thickness of the adhered coatings. If a location of origin is made, such as a notch in one side of the crucible rim, the crucible with sintered coating can be analyzed by x-CT scan. A second scan can be performed after the heating with liquid metal, providing a quantitative 3-D representation of the changes in coating thickness.

5.5.2 Discussion of *In-situ* experiments

As erosion and dissolution are dynamic phenomena, viewing the behavior of TiC particles *in-situ* can provide insight into the protection mechanism. The most notable observation is that the particles floating on the fluid stopped moving completely after a certain amount of undercooling. This phenomenon was most pronounced in a sample with 0.38% wt Ti. Figure 5.5 shows this effect with the upper row of images showing the motion prior to stopping and the bottom images showing the stopped particles. The circled particle in the top row almost completely leaves the screen in 3.5 seconds, but the particles in the bottom row have barely moved in 14.1 seconds.

Flow may have ceased because the TiC particles formed a network or because the fluid was too viscous for the particles to move. Precipitation of Ti(C,N) has been seen to greatly increase the viscosity of molten iron [6,24], but the flow cessation was so complete and immediate that the effect appears to be due to linking of the carbides. While not all particles were visibly connected at the sample surface, the particles may have been connected to one another beneath the metal surface to stop the particle flow. Figure 5.6 shows larger grey TiC particles growing on darker clusters of TiC. These formed around 1240°C, the temperature at which the particle motion ceased during cooling. (Deep-etching was performed on the sample to look for TiC networks, but the Fe-C_{sat} alloy contained a high phase fraction of cementite which was not etched away by the method used.)

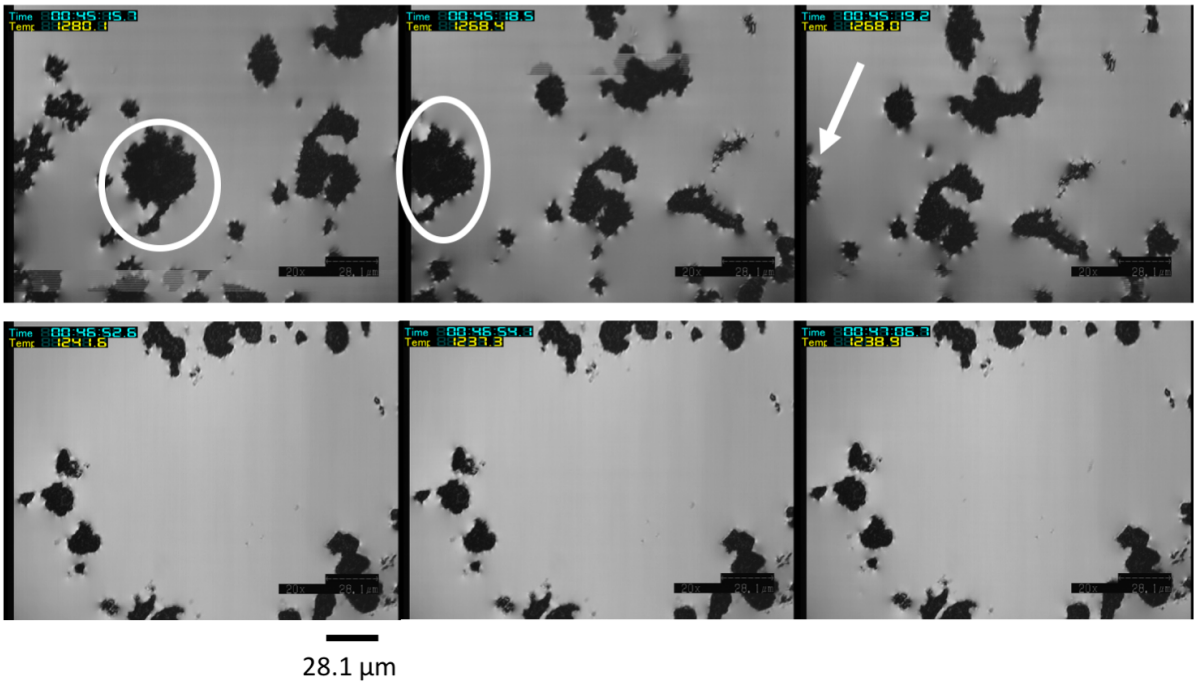

Figure 5.5. *In-situ* high temperature microscopy of molten iron, showing TiC particle motion before flow stoppage (top row – total time span 3.5 s) and after stoppage (bottom row – total time span 14.1 s). White annotations are used to track one particle between images.

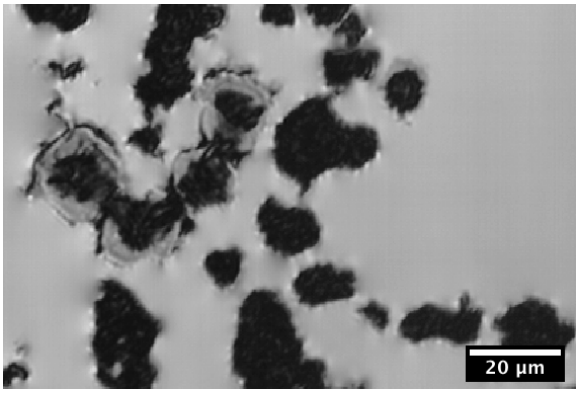

Figure 5.6. *In-situ* view of TiC particles (grey) growing on TiC clusters (black) in liquid iron (1240°C).

Formation of a carbide network could be one of the reasons Ti additions are uniquely able to protect the hearth. A network should be able to cut off metal flow to a much greater extent than a random distribution of unconnected particles. This would be most effective if the carbonitrides show a propensity to adhere to graphite. Otherwise, it would be difficult to localize protection at the hearth wall. Figure 5.7 shows a view from the *ex-situ* experiment of large TiC particles attached to graphite. While this view shows multiple TiC particles adhering to the graphite, carbides seem much more likely to

adhere to themselves rather than the graphite. This is best seen in Figure 5.8 where very small TiC particles have grown into a large TiC cluster on the surface of liquid metal. TiC binds to other particles, creating scaffolds rather than simply free-floating particles. Combined with the ability of TiC to anchor to graphite (at least if pre-sintered), could shed light on why Bergsma and Fruehan's mechanism could only work with Ti additions as opposed to any other addition that could form a compound that would be stable between 1150 and 1400 °C. Within the BF, conditions may be such that scaffolds have greater propensity to form. The present experiments contain relatively small thermal gradients within the metal [25], but the blast furnace has greater temperature gradients in proximity of the refractory hot face. In the BF, the velocity of HM near the hearth will vary. Komiyama et al. give an estimation: below the taphole during tapping; the velocity of metal adjacent to the hot face was 2 mm/s [26]. That is two orders of magnitude larger than what is seen in these *in-situ* experiments. However, the higher velocity could be beneficial to forming scaffolds. The TiC was seen to have a high collision efficiency, i.e., when two TiC particles collided, they almost always remained together. This is consistent with reports that large Ti(C,N) accretions grow primarily through the agglomeration and sintering of smaller TiC particles, rather than an classical atom by atom growth [12]. While the limitations of these laboratory experiments are unclear in regard to fluid velocity, the differences do not preclude this scaffolding from happening within the BF.

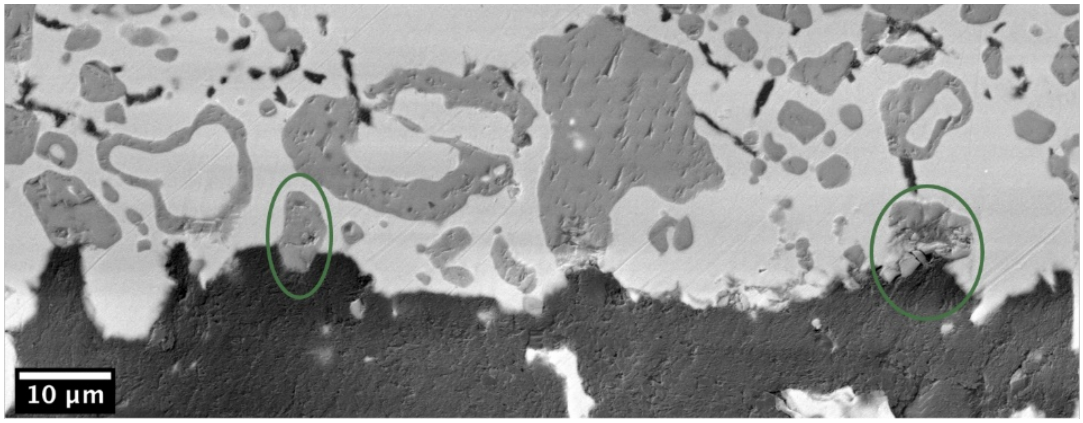

Figure 5.7. *Ex-situ* view of TiC particles (circled) attached to graphite (dark).

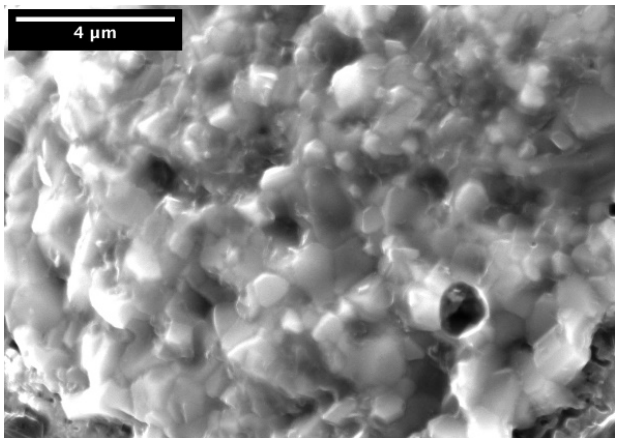

Figure 5.8. Agglomeration of small TiC particles.

The observations listed here support the mechanism proposed by Bergsma and Fruehan and possibly augment it. If TiC is representative of how Ti(C,N) performs, Ti is not replaceable by any compound with a similar stability range. The propensity to agglomerate and create scaffolds could be a previously uninvestigated but key part in how Ti additions protect the hearth.

Ti(C,N) showed similar effects as TiC, only at higher temperatures. Particles from a melt with 0.12% wt Ti began to be stable at 1476 °C, similar to that reported to by Li et al. (1468 °C) [20]. These Ti(C,N) particles had smooth surfaces, were more angular, and not as equiaxed as TiC without N_2. Observations from these experiments are shown in Figure 5.9. Ti(C,N) also coalesced immediately upon formation, forming a structure that had very little motion on the uppermost part of the droplet. This was distinct from TiC, which required a higher area fraction of particles before motion stopped. This can be understood to reflect a difference in sintering behavior: Ti(C,N) high in nitrogen appeared to sinter much better than TiC. This was apparent in the alignment and size of Ti(C,N) particles as well as on the roughness. The nano-sized TiC particles seen upon the rough surfaced TiC particles (by *ex-situ* SEM) joined but were unable to realign to make a single, larger crystal. This agrees with large Ti(C,N) being meso-crystals; i.e., crystals that grow larger by joining with smaller nano-particles rather than atom by atom growth [12]. It may be advantageous that Ti(C,N) is the dominant species in the BF because crystals more readily agglomerated and grew compared to TiC. Upon cooling, Ti(C,N) had an orange hue under the optical microscope, common of crystals high in nitrogen content.

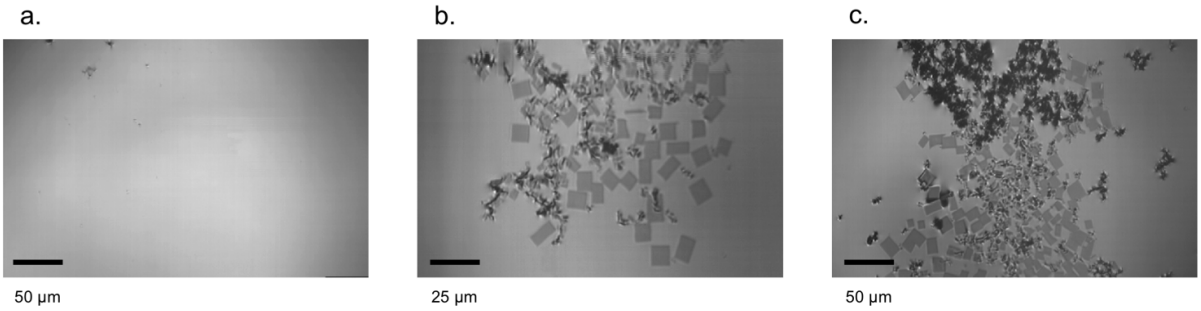

Figure 5.9. Ti(C,N) observations on Fe-C_{sat}-0.12% Ti. a.) particles forming at 1468 °C. b.) agglomerated particles at 1452 °C. c.) agglomerated particles at 1389 °C with a higher fraction having rough surfaces.

5.6 Conclusions

New results are presented to support and augment the mechanism proposed by Bergsma and Fruehan by which Ti additions reduce wear of BF hearth refractory. *In-situ* experiments showed both TiC and Ti(C,N) particles were found to agglomerate into large scaffolds and to stop particle motion on the surface of molten iron. Ti(C,N) particles were seen at temperatures similar to those reported previously. A layer of TiC was found to adhere to a graphite crucible despite the presence of a molten Fe-C_{sat} bath. The agglomeration of TiC and Ti(C,N) particles into clusters may be an additional phenomenon that assists in the protection of blast furnace hearth. This study was a qualitative, first approximation, and future studies will be needed to better quantify these results.

5.7 References

[1] J. Huo and J. Huang: *Ironmak. (In Chinese)*, 2013, vol. 32, pp. 14–6.
[2] K. Narita, M. Maekawa, T. Onoye, Y. Satoh, and M. Miyamoto: *Trans. Iron Steel Inst. Jpn.*, 1977, vol. 17, pp. 459–68.
[3] S. Street, C. Copeland, and E. Worral: in *AISTech Proceedings*, 2013, pp. 381–403.
[4] D. Bergsma and R.J. Fruehan: *60th Ironmak. Conf. Proc.*, 2001, pp. 297–312.
[5] G. Wen, Y. Yan, S. Zhao, J. Huang, G. Jiang, and X. Yang: *Iron Steel (In Chinese)*, 1996, vol. 31, pp. 6–11.
[6] Y. He, Q. Liu, J. Yang, B. Yang, M. Long, H. Zheng, C. Liu, and M. Wei: *Adv. Mater. Res.*, 2011, vol. 146–147, pp. 1911–6.
[7] S. Street, A. Cheng, and I. Cameron: in *AISTech Proceedings*, 2019, pp. 275–88.
[8] Y. Zhao: *Iron Steel Technol.*, 2014, vol. 11, 3 (March), pp. 95–103.
[9] Y. Zhao, L. Lherbier, D. Fu, Y. Chen, C. Zhou, and J. Grindey: in *AISTech Proceedings*, 2012, pp. 457–69.
[10] T. Britt and P.C. Pistorius: *Trans. AIST*, 2022, vol. 19, 3 (March), pp. 292–7.
[11] Y. Deng, J. Zhang, K. Jiao, and Z. Liu: *ISIJ Int.*, 2019, vol. 59, pp. 1–8.
[12] C. Wang, K. Jiao, J. Zhang, and S. Wu: *ISIJ Int.*, 2021, vol. 61, pp. 138–45.

[13] K. Frisk: *Calphad Comput. Coupling Phase Diagrams Thermochem.*, 2008, vol. 32, pp. 326–37.
[14] V. Ivanchenko and Materials Science International Team: *C-N-Ti Ternary Phase Diagram Evaluation*, in Springer Materials.
[15] J. Naidich: *Prog. Surf. Membr. Sci.*, 1981, vol. 14, pp. 353–484.
[16] P. Alvaredo, M. Dios, B. Ferrari, and E. Gordo: *J. Alloys Compd.*, 2019, vol. 770, pp. 17–25.
[17] P. Xiao and B. Derby: *Acta Mater.*, 1996, vol. 44, pp. 307–14.
[18] K. Datta, P. Sen, S. Gupta, and A. Chatterjee: *Steel Res.*, 1993, vol. 64, pp. 232–8.
[19] H. Inoue, M. Nitta, T. Matsui, T. Wakasa, Y. Yamagami, and T. Mochida: *United States Pat.*, Patent #8889062, Nippon Steel and Sumitomo Metal Corporation, 2014.
[20] Y. Li, Y. Li, and R.J. Fruehan: *ISIJ Int.*, 2001, vol. 41, pp. 1417–22.
[21] M. Sumito, N. Tsuchiya, K. Okabe, and K. Sanbongi: *Trans. Iron Steel Inst. Japan*, 1981, vol. 21, pp. 414–21.
[22] L.F.S. Dumitrescu and M. Hillert: *ISIJ Int.*, 1999, vol. 39, pp. 84–90.
[23] W. Straszheim, K. Younkin, R. Greer, and R. Markuszewski: *Scanning Microsc.*, 1988, vol. 2, pp. 1257–64.
[24] Y. Deng, J. Zhang, and K. Jiao: *Ironmak. Steelmak.*, 2018, vol. 45, pp. 773–7.
[25] S.T. Britt and P.C. Pistorius: *Metall. Mater. Trans. B*, DOI:10.1007/s11663-022-02515-4.
[26] K. Komiyama, B. Guo, H. Zughbi, P. Zulli, and A. Yu: *Metall. Mater. Trans. B*, 2014, vol. 45, pp. 1895–914.

6 Dissolution Kinetics of Graphite into liquid Fe-C-Ti and Fe-C-Ti-N Systems

6.1 Abstract

The charging of titanium ores is known to increase the life of carbonaceous blast furnace hearth refractory. However, it is unknown what the importance of forming Ti(C,N) is as well as which degradation mechanism it improves. High-purity graphite rods were rotated while immersed in a molten bath of either Fe-C, Fe-C-Ti, or Fe-C-Ti-N, to measure dissolution rates. The mass transfer coefficients of graphite dissolution were near 10^{-5} m/s. Compared to dissolution in Fe-C, formation of Ti(C,N) slightly reduced the isothermal dissolution kinetics of graphite into Fe-C-Ti-N. No reduction was seen by having only dissolved Ti in the hot metal. Ti(C,N) existed as large agglomerations rather than groups of distinct particles. These agglomerations were most often seen removed from the dissolution interface. While Ti(C,N) affected dissolution kinetics little, it is proposed the mechanism held by industry is still valid. These results point to the importance of cooling the refractory hot face.

6.2 Within the Narrative

The dissolution of hearth refractory is an important topic. At the end of many blast furnace campaigns, an "elephant's foot" wear profile is often observed, mainly attributed to the fluid flow of the metal. Because dissolution of graphite is mass transfer controlled, an increase in fluid velocity increases dissolution rate. Understanding the effect of Ti(C,N) on dissolution can help to adjust charge practice. Additionally, understanding the effect of Ti(C,N) on only dissolution can help to test Bergsma and Fruehan's mechanism.

The presentation of Bergsma and Fruehan's protection mechanism and the case study are vital to the contextualization of these results within blast furnaces. The explanations and supporting figures are re-presented in Ch. 6.3 due to this importance.

6.3 Introduction

The campaign life of the blast furnace has long been limited by the life of the refractory hearth. Once there is insufficient thickness in the lining, the furnace must be taken offline, often for many months to rebuild the hearth. This is a massive

expenditure both for the materials involved and for the labor to repair the furnace, and incurring lost production [1,2]. The state of the hearth is critical to operation and productivity of the blast furnace but also to its safety. Li et al. reported (in 2020) that 30% of blast furnace accidents in China were related to hearth erosion [3]. Thus, there is great motivation to study hearth wear.

The carbonaceous refractory used in the hearth can degrade by many mechanisms: attack by vapor phases (alkali metals, zinc, or oxygen), penetration of liquid metal into pores, and chemical dissolution [4,5]. Deterioration by many mechanisms, except for chemical dissolution, can be limited by controlling the pore size of refractory during manufacturing [6]. Dissolution must be limited by correct operation of the furnace. This is a challenge because thermodynamics is against a long hearth life. Liquid hot metal (HM) undersaturated with carbon will dissolve carbon brick until saturation is reached, given ample time. However, much of the dissolved carbon in HM comes from coke rather than the refractory [7]. It is when the deadman, a porous coke bed within the hearth, is either clogged or floating that wear by dissolution is expected to occur [8–10]. While maintaining near-saturated HM is ideal, other operational practices can also protect the hearth. Keeping the refractory hot face below 1150 °C solidifies a "skull" of eutectic Fe onto the hot face. This solid layer further protects the hearth refractory from liquid and vapor species [11].

Despite these precautions, wear events will occur, including those due to undersaturated metal contacting the hot face. For graphite refractory, the rate of dissolution is mass transfer limited [12,13], i.e., controlled by the rate of [C] transport through the diffusion boundary layer. Amorphous forms of carbon - more commonly used on the hot face [5] - have been reported to dissolve more slowly, a combined effect of a layer of inorganic impurities ("ash") covering the refractory-metal interface and of the higher activation energy needed to break the sp^3 bonds [4,12–16]. Whether the material is graphitic or amorphous, both show correlations between the rate of dissolution and the fluid velocity. A sitting, porous deadman is desired to decrease velocity near the refractory: metal can flow through the deadman instead of high velocity metal flowing below the deadman and circumferentially around the hot face [8–10].

Hearth wear is usually well controlled to between 3-10 mm/month through utilizing a high-quality refractory and sound operating practice [17]. However, industrial data often shows "wear events" rather than a constant decrease in thickness [18–20]. When a wear event does occur, remedial steps are taken to protect the hearth, often either by decreasing production or charging Ti bearing ore. This is exhibited in a case study at

Shougang Jingtang BF No. 2, shown in Figure 6.1. Adjusting the flow rate and temperature of the cooling water had a minimal effect to improve the refractory condition (line A) [18]. Furnace productivity was decreased to control the temperature (line B), but the temperatures at normal productivity (Line C) returned to normal only after charging ilmenite (ferrotitanium ore) (Line D).

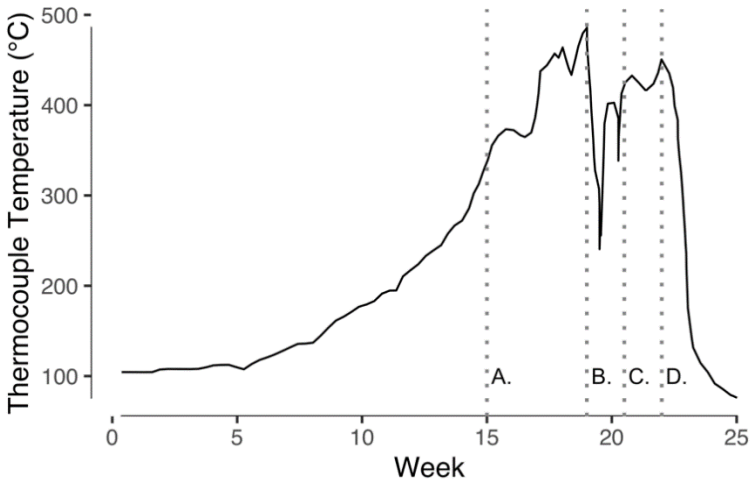

Figure 6.1. Case Study of Shougang Jingtang BF No. 2 [18]. Line A: cooling water flow rate increased. Line B: Production decrease. Line C: Production increase. Line D: Ilmenite charging initiated.

The charging of Ti-bearing ore to protect hearth refractory after wear events was documented as early as 1965 [18,21]. The commonly accepted protection mechanism was hypothesized by Bergsma and Fruehan [22] and is shown in Figure 6.2:

1. Ti ore charged into the furnace is reduced, with [Ti] dissolving in the HM.
2. Refractory is in contact with hot metal (Figure 6.2a) then lost in a wear event (Figure 6.2b). This thinner region of intact refractory has a lower thermal resistance between the hot face and the cooled outside of the hearth. The lower resistance results in a lower hot-face temperature (Figure 6.2b).
3. When the temperature is low enough (occurring after enough refractory loss), the formation of Ti(C,N) crystals is thermodynamically favorable, shown in Figure 6.2c.
4. Ti(C,N) crystals restrict the flow of metal in the region of lost refractory. Enough restriction can facilitate heat extraction so that the iron can solidify, shown in Figure 6.2d.

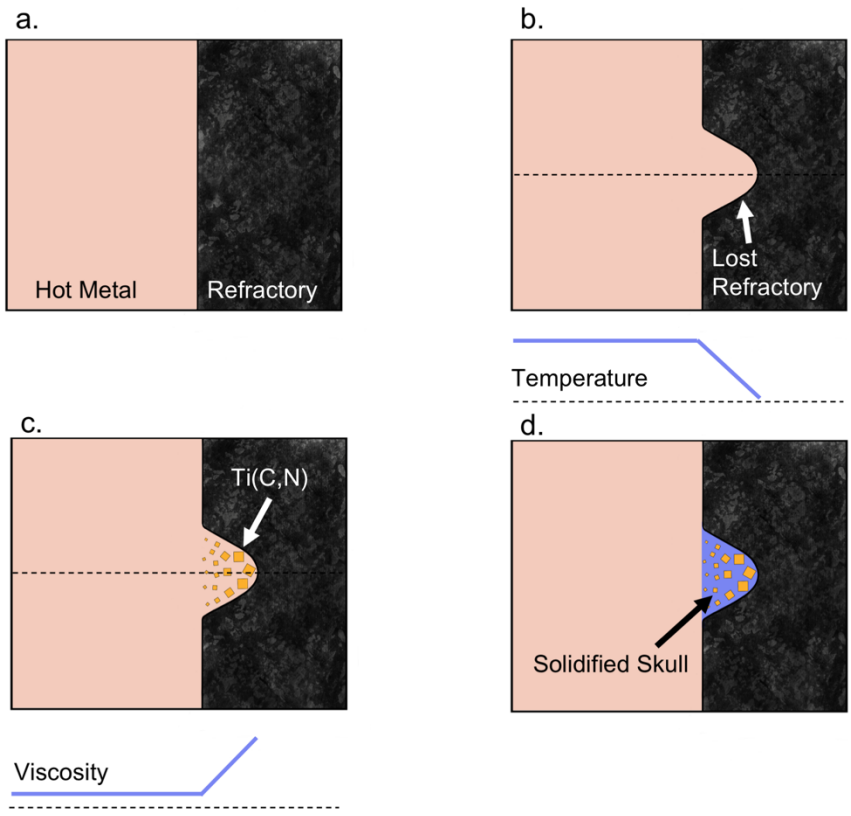

Figure 6.2. Hypothesized mechanism of Ti(C,N) protection of the hearth. a.) HM-refractory interface before wear has occurred. b.) a wear event has occurred, leaving a thinner region of refractory. The thinner region promotes a temperature drop in the hot metal in the region that was lost. c.) if the temperature is low enough, Ti(C,N) become stable. This increased solid volume increases viscosity. d.) With HM flow restricted by the solid Ti(C,N), enough heat can be extracted to solidify a skull in the region where refractory was lost.

This can be paraphrased by stating that Ti(C,N) catalyzes skull formation. This mechanism is similar to the concept of fluidity in the casting industry, where the solidification of dendrites restricts liquid metal flow. Ti(C,N) has been seen to agglomerate in liquid HM [23], and, in worn areas of the hearth, those agglomerations could act similarly to dendrites in the casting molds. Even if these agglomerations do not fully close off metal flow, an increase of the solid in a fluid increases that fluid's apparent viscosity, per the Einstein-Roscoe relation [24]. Indeed, increases of Ti content in pig iron resulted in higher viscosities once TiC or Ti(C,N) formed [25,26]. Simulation work has shown that an increase of liquid metal viscosity promotes skull formation [27], and the viscosity increase is vital to the formation of a Ti containing skull [28].

Though this mechanism is widely accepted by industry [29], there are still unknowns. While the viscosity increase of Ti(C,N) formation is vital to the proposed mechanism, a decrease in dissolution rate of hearth brick into HM has been observed when HM

contained dissolved [Ti] (without Ti(C,N) formation) [30]. Dissolved Ti has been reported to increase HM viscosity [25], and a reduction in dissolution rate is expected, since mass transfer kinetics are inversely dependent on viscosity [31]. While additions should be most effective when Ti(C,N) forms, a study has not been performed that compares the effect of [Ti] to Ti(C,N). Though hearth refractory can degrade by a number of mechanisms, dissolution is the emphasis of this work because of the prevalence of the elephant's foot. This work compares the kinetics of graphite dissolution into three HM systems: Fe-C, Fe-C-Ti, and Fe-C-Ti-N. Performing isothermal dissolution experiments also allows a check of Bergsma and Fruehan's mechanism. It is thought that formation of a metal skull is needed for protection, but an isothermal dissolution experiment will only form Ti(C,N) without Fe solidification. Should Ti(C,N) provide a large reduction in rate under these conditions, the proposed mechanism may need to be revised to lessen the focus on iron solidification.

6.4 Experimental Procedure

6.4.1 Input Materials

Ingots of Fe-C were prepared by melting electrolytic iron in graphite crucibles under argon in an induction furnace. When the metal was observed to melt, the temperature was held constant for 40 minutes at an estimated temperature of 1155 °C before cooling. The temperature was likely higher than this to enable melting, but the maximum nominal temperature measured by thermocouple was 980 °C (measured below the crucible). The graphite crucible adhered to the solidified metal, and a belt grinder was used to remove the excess graphite. Fe-C ingots were determined by combustion analysis to have carbon concentrations between 4.23% and 5.15% wt with 10 ppm of [N]. Fe-C_{sat}-N ingots were prepared as above except melting under an N_2 atmosphere. These ingots had carbon concentrations between 5.48% and 5.54% with 80-100 ppm of [N].

Graphite samples were obtained in the form of isostatically pressed, high-purity (less than 5 ppm total impurity content) rods 13.5 cm long with 1.5 cm diameter. The rods had a mass around 45 g, giving a density near 1.86 g/cm^3. The rods were machined with a flat face containing two holes at one end. A mirror side was machined onto a rod of machinable alumina so that the two could be held together with alumina fasteners. Steel fasteners were used to connect the alumina rod to a stainless-steel rod at the top of the assembly. This set up is shown in Figure 6.3a. Rubber bellows with a rotary feedthrough were used to seal the chamber from the outer atmosphere while allowing

height adjustments of the rod, shown in Figure 6.3b. This assembly was connected by vacuum fittings to the water-cooled cap of the tube furnace.

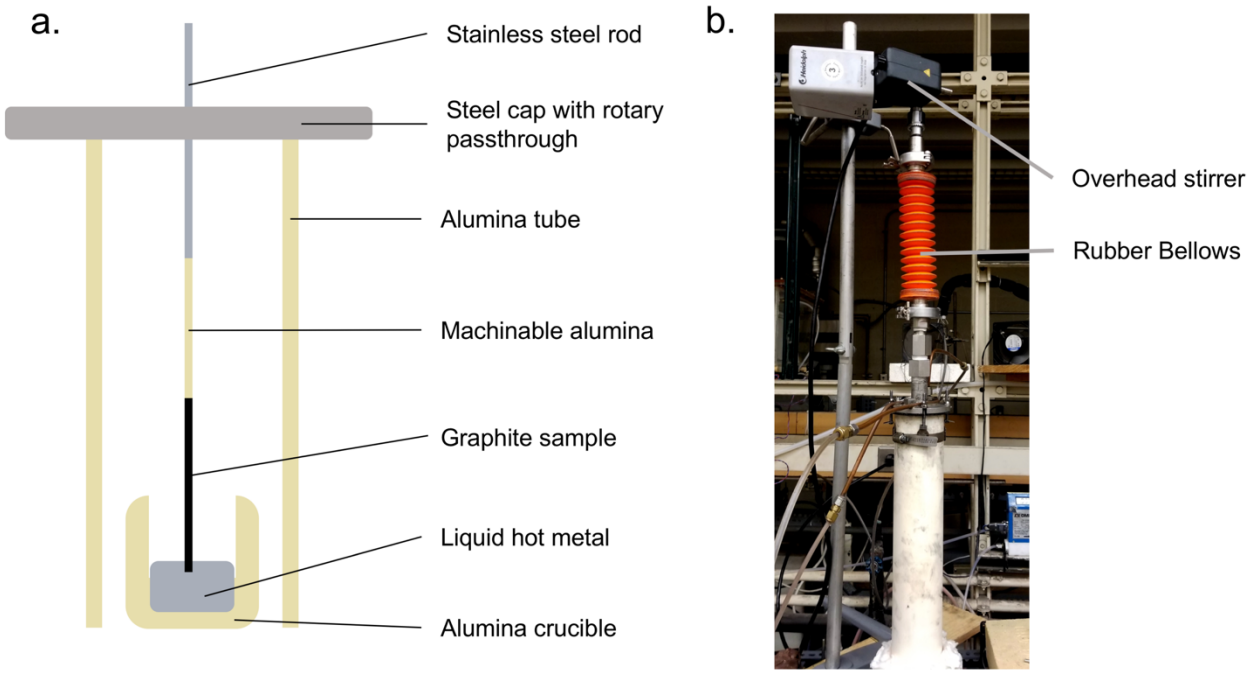

Figure 6.3. Tube furnace and stirring set-up. a.) schematic drawing of stirring apparatus b.) external view of stirring apparatus

6.4.2 Dissolution Experimental Procedure

Three groups of metal compositions were tested: Fe-C, Fe-C-Ti, and Fe-C-Ti-N. The latter was the only one expected to precipitate Ti(C,N); TiC is not expected to be stable in the chosen Fe-C-Ti ternary at the temperatures used [32]. The composition for each group is shown in Table 6.1. To prepare the experimental melts, Fe-C_{sat} ingots (Fe-C_{sat}-N for group C) were sectioned into slices (240-280 g) and mixed in an appropriate balance with electrolytic iron (~190 g), graphite (~0.6-3.6 g), and, when needed, Ti granules (~0.65 g). To introduce no new impurities, the graphite was added as pressed pieces, excess from either the carbon rods or the graphite crucibles used to carburize the precursors. This mixture was placed within an alumina crucible (49 mm ID, 96 mm height) and set within a vertical tube furnace. The furnace was capped, and the rod was lowered into the crucible so as to touch the metal within the crucible. The sample (rod) was raised approximately 12 mm from this position, to ensure that the carbon sample would be within the crucible when lowered, and not mislocated between the crucible and furnace tube. Gas - N_2 for the quaternary ingot, Ar for the others - flowed through

the furnace tube at 0.933 L/min. The furnace was heated at 5 °C/min to 1300 °C. This temperature was held for 10 minutes before manually lowering the graphite rod into the melt. About 3 cm of the sample was immersed, determined by letting the rod contact the crucible bottom before raising it by 6 mm.

Table 6.1. Initial Metal Ingot Compositions

Ingot	Group	Total mass (g)	C (% wt)	Ti (% wt)	N (ppm)
Fe-C	A	435	3.26	—	—
Fe-C-Ti	B	435	3.26	0.15	—
Fe-C-Ti-N	C	435	3.26	0.15	50

Once immersed, the rod was rotated by an overhead stirrer at 48 RPM for 30 minutes. The speed and time were chosen to have a measurable dissolution without reaching carbon saturation. After 30 minutes, rotation was stopped, and the rod assembly was raised by 75 mm to remove the rod from the melt. Upon cooling, the graphite rod was removed from the stirring assembly, and the metal ingot was broken from the crucible.

For this discussion, "group" will refer to the composition of the metal ingots, with group A being Fe-C, group B being Fe-C-Ti, and group C being Fe-C-Ti-N. The "series" gathers experiments that had the most similar precursor materials and stirring apparatus. As an example, Sample A1 and B1 (both in Series 1) used the same precursor ingot. Denoting the series is also important due to the degradation of machinable alumina, part of the stirring assembly. Series 1 and 2 were performed under similar conditions. All samples within Series 3 used alumina with one broken connection point at the stainless-steel side. This resulted in circumferential stirring around the crucible edge rather than a tight circle in the center of the crucible. Series 4 used a new alumina rod but shorter graphite samples (around 9.2 cm) and a longer stainless-steel rod. These rods were re-used from prior experiments, and any parts that had experienced dissolution were removed.

6.4.3 Experimental Considerations

The temperature of dissolution, initial carbon concentration, and rotational rate were primarily limited by the experimental apparatus, but most of these conditions can be found within the BF. The temperature of dissolution (1300 °C) was limited by the tube furnace used, but Fe beginning at 2.96% wt C (the composition at the liquidus of austenite) would dissolve over 1.68% wt C before reaching graphite saturation (4.64% wt C) [33]. The initial carbon concentration was chosen to ensure the ingot was completely melted at 1300 °C while having a driving force of 1.38% wt C for dissolution.

Ti content was at the upper end of what is intentionally used in the BF [29], chosen to exacerbate any effect that Ti would have on the dissolution kinetics. The rotation rate was limited by the stability of the apparatus, and thus the tangential velocity (0.63 cm/s) was lower than the expected flow within the BF [9].

To determine the effect of convection within the melt, one dissolution experiment was performed by immersing a graphite rod in an Fe-C melt without stirring, deemed experiment A1nr. This rod experienced an increase in mass (due to the adhered metallic droplet on the tip) and a change in surface finish, but neither the length nor the diameter experienced a measurable change. Little dissolution occurred without rotation, and the initial dip into the metal that each rod experienced did not affect the overall dissolution kinetics.

Fe-C-Ti-N metal compositions were designed to form Ti(C,N). These quaternary melts did form Ti(C,N) as evidenced by the red-purple color of the ingot surface after solidification in Figure 6.4a. The color was characteristic of N-rich Ti(C,N) [34], and energy dispersive spectroscopy confirmed the presence of Ti(C,N). Melts without N (Group A and B) did not exhibit these characteristics.

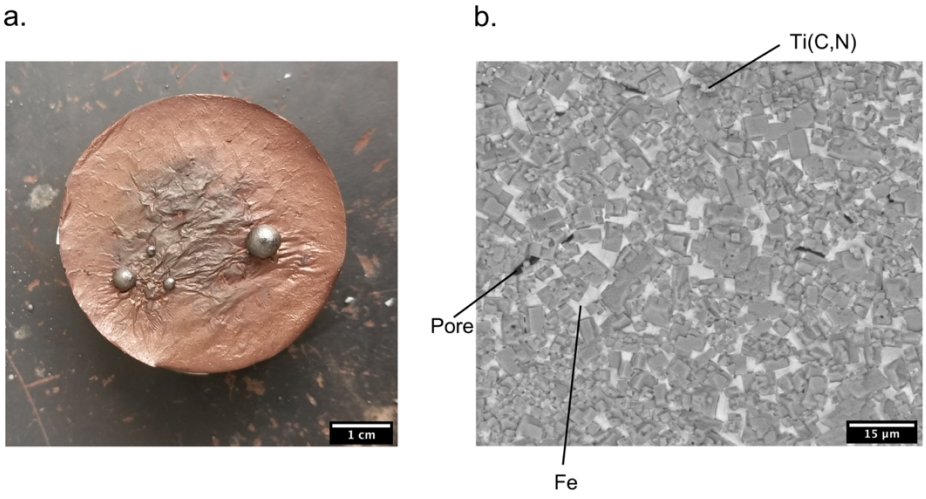

Figure 6.4. Surface of the Fe-C-Ti-N ingot (melt C1). a) Macroscopic image. Note the red-purple color characteristic of N-rich Ti(C,N). b.) Back-scattered electron micrograph of ingot surface. The dark grey, faceted particles are Ti(C,N).

6.4.4 Carbon Concentration Analysis Methods

Before and after experiments, graphite rods were weighed, measured with calipers, and photographed. Measurements of the length of the rod, the length of the adhered metal tip, and the length of the dissolved zone were taken using calipers. Each image was taken in same location with the same backdrop using an Olympus mirrorless camera to ensure that the lighting and scale between images were similar.

Multiple methods were used to determine the change in carbon concentration of the metal resulting from rod dissolution. The most straightforward, a change in rod mass, underestimated rod mass loss, due to the presence of adhered iron. Combustion analysis of the solidified melt was performed by an external laboratory for [C] in binary and ternary alloys and [C] and [N] for quaternary alloys. Issues with both of these approaches led to the use of volume-based methods. The "image-based" approach utilized photographs to obtain 2D projections of the rods, which were able to be integrated to obtain a volume. This image-based approach required processing of the images before integration could be performed. The steps are shown below:

1. Pre-processing: using ImageJ, a scale was determined for pixel to μm conversion. Images were then cropped and rotated so that the edge of the rod was horizontal, and a filter to detect edges was applied. The result of this pre-processing step is shown in Figure 6.5a.
2. Extraction: in Web-plot digitizer, point extraction was performed using the pen tool to trace the outline of the rod [35]. Automatic extraction was performed with an averaging window of 7x7 px. The points were then edited manually, including adjusting the tip curvature so that the points extracted were from the tip of the graphite, rather than the tip of metal which had more prominent edges. Points were extracted from the tip until the undissolved zone was reached. Rod C1 with extracted points is shown in Figure 6.5b.
3. Numerical Integration: in R, numerical integration was performed using the trapezoidal method. One image was used per sample, and one volume was obtained using the points above the centerline and another using the points below the centerline. Eq. 1 was used to calculate the volume (V_{tip}) of each half, where h_n was the height between the centerline and the rod edge at a point nearer the tip, h_{n+1} was the height at the adjacent point moving away from the tip, d_n was the distance from the rod tip to the point along the center line, d_{n+1} was the distance at the adjacent point moving away from the tip, and i was the total number of points on one side of the centerline.

4. Calculation of Carbon Concentration: tip volumes were an average of the two integrations performed on each image. A change in volume (ΔV) could be obtained by Eq. 2. V_i was the volume of the rod prior to dissolution, V_{bulk} was the remaining volume of the rod not examined by numerical integration (a simple cylinder). ΔV could then be converted to a change in mass, and the final composition was determined based on a mass balance.

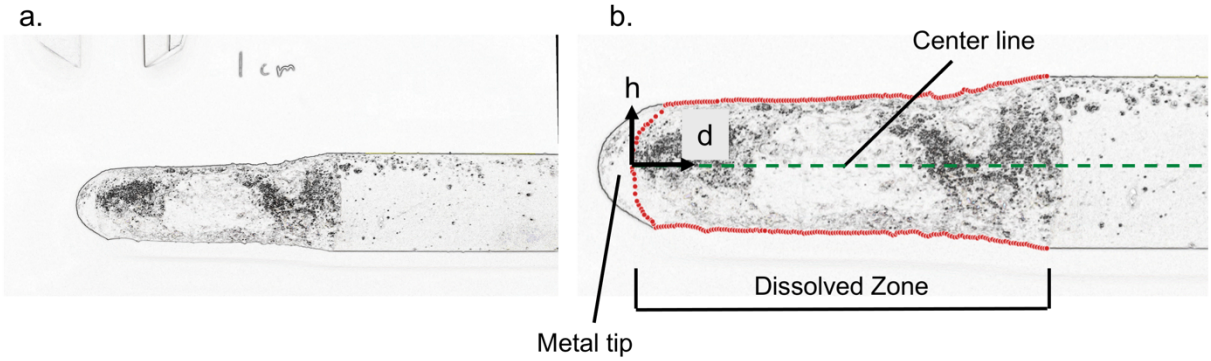

Figure 6.5. Image of rod C1 used for point extraction. a.) Image after pre-processing. The scale of the image could be determined by measuring the number of pixels between caliper edges in the top left of the image. b.) Image showing extracted points (red), centerline (green), and denoting the dissolved zone and metal tip. The axes show the direction of h and d used in the volume integration calculation (Eq.1).

$$V_{tip} = \sum_{n=1}^{i-1} \pi(d_{n+1} - d_n) * \left(\frac{1}{2}(h_n + h_{n+1})\right)^2 \quad \text{Eq. 1}$$

$$\Delta V = V_i - \left(V_{tip} + V_{bulk}\right) \quad \text{Eq. 2}$$

Two other volume-based methods were considered. The first utilized a Matter & Form MFS1V2 3D scanner to scan the dissolution zone of rods. Specifications cannot be provided due to settings being relative sliders rather than numerical parameters. An optical comparator (Master-View II MV-14Q with Quadra-Chek 200 digital readout) was used to verify the results of the image-analysis method. The comparator was used to extract the location of the sample edges; the extracted points were used in numerical integration following steps 3 and 4 above. Two projections were taken of each sample, rotating 90° between projections. The average of the four volumes was used to calculate ΔV.

6.4.5 Calculation of Mass Transfer Coefficients

Performing rotating rod dissolution experiments results in parameters that change during the experiment. Rather than assuming initial values of carbon concentration, interfacial area, and metal volume, an iterative method was used to calculate the mass transfer coefficient. The functional form used to calculate the mass transfer coefficient (k_{exp}) is shown in Eq. 3 with the interfacial area at a particular step (A_n), the volume of metal at a particular step (V_n), the carbon saturated value (C_{sat}), the carbon concentration at the particular step (C_n), the difference in carbon concentration between each step (ΔC), and the time of each step (Δt). It was assumed that the rod kept the shape of a cylinder throughout the process, and that ΔC was constant for each step of the integration. The constant ΔC was defined by Eq. 4, where C_f is the final carbon concentration in the metal, C_i was the initial carbon concentration, and N_{steps} was the number of steps used in the numerical integration.

Each calculation assumed a constant mass transfer coefficient. To obtain the correct k_{exp}, Eq. 3 was solved for Δt at every step. If the sum of the Δt for the calculation equaled 30 minutes, the assumed k_{exp} was correct. Otherwise, the calculation was repeated with a new k_{exp} until the correct value was found.

$$\frac{\Delta C}{\Delta t} = \frac{k_{exp} A_n}{V_n} (C_{Sat} - C_n) \quad \text{Eq. 3}$$

$$\Delta C = \frac{C_f - C_i}{N_{steps}} \quad \text{Eq. 4}$$

Rotating rod mass transfer experiments are well characterized in literature. A correlation from literature for the geometry used can provide a comparison to the experimental results. For the rotating rod system used, the literature mass transfer coefficient (k_{lit}) can be calculated from Eq. 5, with the cylinder diameter (d_{cyl}), the diffusivity of carbon in molten iron (D_C), the Reynolds number (Re), and the Schmidt number (Sc) [31]. Equations for the thermophysical properties that make up Re and Sc are contained in Eq. 6-8 [36–38]. In Eq. 6, The viscosity of molten iron is μ (in mPa∗s), R is the ideal gas constant (in J/mol∗K), and T is the absolute temperature in K. The density of molten iron (ρ) in g/cm^3 is defined by Eq. 7, where $\%C$ is the carbon content of the metal in weight percent. Eq. 8 defines the diffusivity of carbon in molten iron (D_C) in cm^2/s with variables in the same units as above.

Calculation of k_{lit} also used an iterative method. The rod geometry and thermophysical properties were updated at each step for 10^3 steps. Sample values for the first step in a calculation are shown in Table 6.2.

$$\frac{k_{lit} d_{cyl}}{D_C} = 0.079 * Re^{0.7} Sc^{0.356} \quad \text{Eq. 5}$$

$$\mu = 0.3147 \exp\left(\frac{46480}{RT}\right) \text{mPa·s} \quad \text{Eq. 6}$$

$$\rho = (7.1 - .0732 * \%C) - (8.28 - 0.874 * \%C) * 10^{-4}(T - 1823) \text{ g/cm}^3 \quad \text{Eq. 7}$$

$$D_C = \exp\left(\left(-\frac{12100}{T} + 2.568\right) + \left(\frac{1320}{T} - 0.554\right) * [\%C]\right) \text{cm}^2/\text{s} \quad \text{Eq. 8}$$

Table 6.2. Values from the literature mass transfer calculation of graphite dissolution into liquid Fe under initial conditions

$v\left(\frac{cm}{s}\right)$	$\rho\left(\frac{g}{cm^3}\right)$ [36]	$\mu\ (mPa * s)$ [37]	$D_C\left(\frac{m^2}{s}\right)$ [38]	*Re*	*Sc*
0.63	6.996	0.0110	8.88×10^{-9}	62	177

6.4.6 Salt Dissolution Experimental Methods

Dissolution of salt into de-ionized water is mass transfer controlled [39,40] and can be used to determine the deviation of the current experimental set-up to the ideal set-up described in literature. The methods to dissolve salt rods in water was much the as the graphite dissolution.

Salt (NaCl) was substituted for graphite rods. Pink Himalayan salt was obtained in block form from State Line Track. Blocks were cut into rectangular rods and turned on a jeweler's lathe until cylindrical. The brittleness of the salt and the size of the lathe determined the dimension of each rod. Rods were of similar length to those used in Series 4 and were turned only until cylindrical, rather than risking fracture by turning until a 1.5 cm diameter. Rod measurements are listed in Table 6.3.

Table 6.3. Initial Salt Rod Dimensions

Diameter (cm)	Length (cm)	Pre-dissolution Mass (g)
1.618	8.348	28.9894
2.099	9.112	51.6059

De-ionized water (65 mL) was added to alumina crucibles (those used in the graphite dissolution). A filled crucible was placed into the cold tube furnace. The temperature of the furnace was measured between the crucible wall and tube wall by K-type thermocouple (21.5 °C). Salt rods were attached to the stirring assembly that was used in the Series 4 dissolution. The thermocouple was removed, and the furnace was capped with the stirring assembly inserted. The salt rod was immersed into the water and stirred at 48 rpm for 30 minutes. The rod was removed, dried with compressed air and placed in a desiccator for 3 hours. The salt rod was then weighed and measured with calipers. Unlike the graphite rods, liquid did not adhere to the salt rods, and a change in mass was sufficient to capture the change in final composition. The properties used for the calculation of both experimental and literature mass transfer coefficient are provided in Table 6.4.

Table 6.4. Parameters used in Salt Rod Mass Transfer Coefficient Calculation

M(kg)	$C_{sat}^{H_2O}$(%) [41]	ρ_{H_2O} (g/cm³) [42]	ρ_{NaCl} (g/cm³)	μ_{H_2O} (mPa·s)	D_{NaCl} (m²/s) [43]
0.063	31	0.997	2.16	1	1.55×10^{-9}

6.5 Results and Discussion

6.5.1 Qualitative Dissolution Results

A composite image of the dissolved rods from Series 1-3 is shown in Figure 6.6. Prior to dissolution, samples were uniform in length and diameter. All exhibited adhered metal, though to varying degrees. For the samples dissolved in Fe-C, these adhered droplets were mostly hemispherical while the ones dissolved in the quaternary system (Fe-Ti-C-N) showed more angular adhesions. Samples dissolved in the ternary (Fe-Ti-C) gave mixed results with sample B1 having little adhered iron, B2 exhibiting mostly angular adhesions, and B3 and B4 having hemispherical adhesions. Series 3 differed from the other dissolutions: the region where dissolution occurred was shorter in length and smaller in diameter than other series. This was due to the alumina rod degrading, resulting in a stirring pattern where the rod followed the inner edge of the crucible (circumferential rotation). The density difference between the molten metal and graphite would result in buoyant force that prevented the rod from being vertical within the melt.

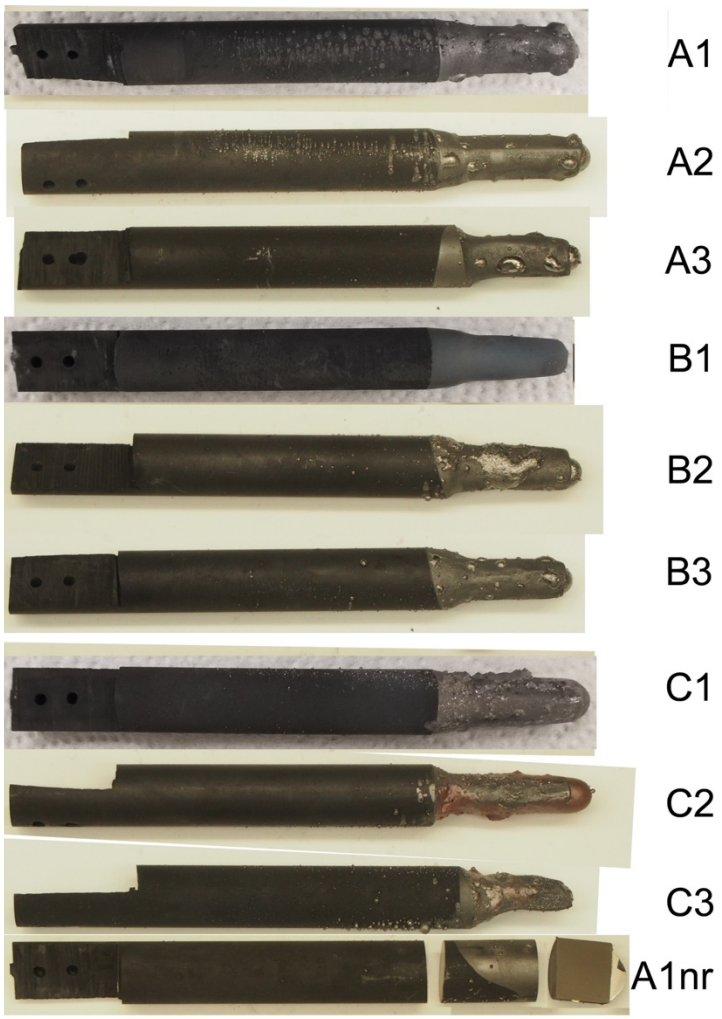

Figure 6.6. Composite image of Series 1-3 of dissolved rods. The tip of A1nr was removed and sectioned to allow for 3D scanning and microscopy.

6.5.2 Composition Analysis Validation

Analysis of composition by rod mass was the most straightforward way to determine C_f of the ingot. However, the metal adhered to the rods would result in a smaller apparent change in mass, leading to lower calculated carbon concentrations than reality. For this reason, multiple methods were compared to determine ingot compositions. Final carbon concentrations by the various methods of analysis are shown for samples A1, B1, C1, A2, and C2 in Figure 6.7. As expected, analysis by rod mass change consistently gave the lowest carbon concentrations. Determination by combustion analysis (of the metal from the crucible after the experiment) consistently gave the highest concentrations with some erroneous results (B1 and A2). Carbon saturation at 1300 °C is 4.64% wt [33], but samples B1 and A2 were analyzed as having compositions above saturation. If these numbers were true, either the metal ingot

would have to be oversaturated before dissolving the graphite rod, or the temperature of liquid would have to be greater than 1300 °C. For the former, the rod would not have experienced dissolution if the liquid was already carbon saturated (contrary to what was observed). For the latter, the temperature was confirmed to be 1300 °C by thermocouple when heating an empty crucible.

With mass loss analysis an underestimate and combustion analysis an overestimate, volume analysis methods were pursued (image-based and 3D scanner-based). Volume analysis gave values between the mass and combustion methods, did not result in values above saturation, and were consistent between methods for the samples in Figure 6.7. The image-based volume analysis method was initially chosen over the 3D scanner method due to the former's ability to account for adhered metal and to avoid the black-box method of the scanner.

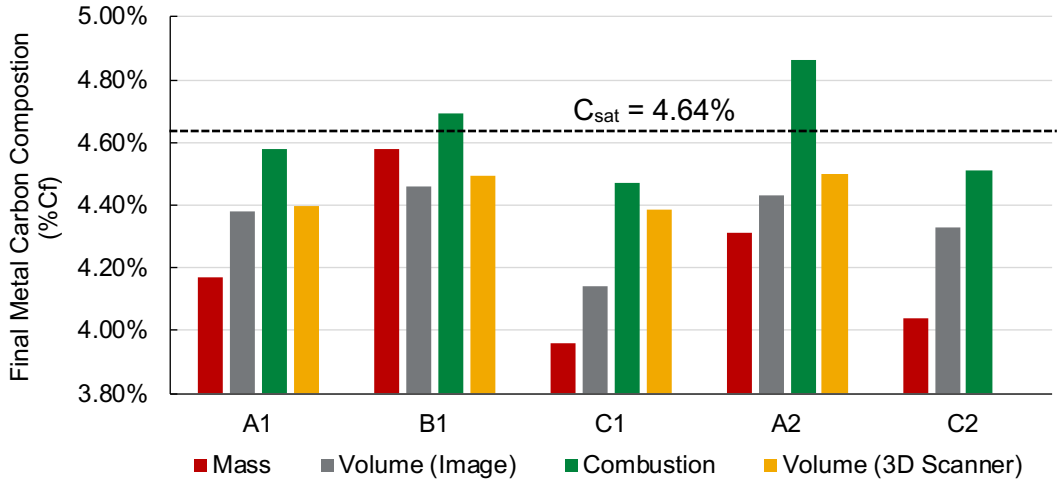

Figure 6.7. Resulting calculated or analyzed final carbon concentration for samples A1, B1, C1, A2, and C2 as determined by assorted methods. Dotted line denotes the carbon content at saturation for liquid Fe-C at 1300 °C [33].

Two additional methods were employed to further verify the results of the image-based method. Samples A3 and B3 were etched in a solution of 1 M HCl and 1 M HNO3 for 5 days, to remove adhered metal. The remaining metal that adhered to the tips was scraped away at the end of this period. Samples were dried for one week before measuring the mass and, separately, the volume by 3D scanner and optical comparator. The latter could evaluate the effectiveness of the point extraction process of the image-based method.

Figure 6.8 shows the resultant carbon concentrations of A3 and B3 as determined by the assorted metrics, both before etching and after etching. These samples also showed that a simple calculation based on mass loss (with adhered metal) gave the lowest concentrations. The compositions obtained by 3D scanner were high, whether etched or not. The etched scanner value for Sample B3 was above the carbon saturation limit. This, along with another laboratory member noting inconsistent results, excluded the 3D scanner from consideration.

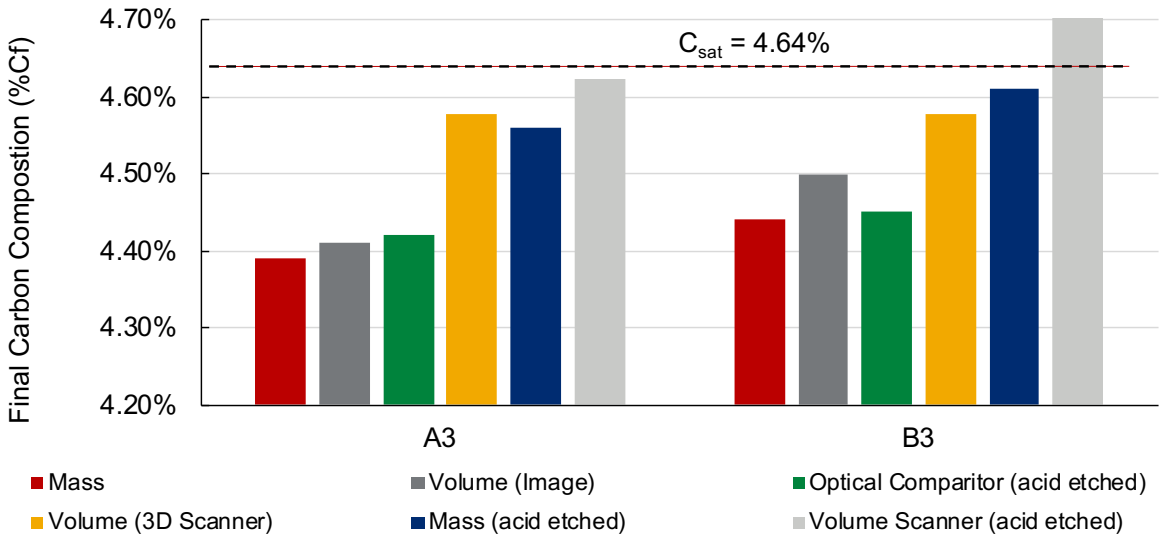

Figure 6.8. Carbon concentrations determined by mass and volume-based methods both before and after etching for samples A3 and B3. Dotted line denotes the carbon content at saturation for liquid Fe-C at 1300 °C [33].

The optical comparator and the image-based methods gave similar results, noted in Table 6.5. The difference was ≤0.05%. This serves to verify the image-based point extraction. However, those numerical integration methods differed from the mass loss of the etched sample by as much as 0.15% wt. Investigation was made into this discrepancy with no conclusion. Investigations were made on the integration code, the caliper measurements, the pixel to μm conversion, and consistency between images, but no aspect of the experimental approach could account for the difference between the volume methods and the etched mass measurements. Table 6.6 shows the resultant mass transfer coefficients, using the two volume-based techniques. The mass transfer coefficient is sensitive to the%C_f. For sample A3, a difference in 0.01% C resulted in a 0.19×10^{-5} m/s difference in k_{exp}, and the larger difference for sample B3 was even more pronounced.

Table 6.5. Final Carbon Concentrations of A3 and B3 by Different Methods

Sample	[%C_f] by Image	[%C_f] by Optical Comparator
A3	4.41	4.42
B3	4.50	4.45

Table 6.6. Mass Transfer Coefficients of A3 and B3 by Different Methods

Sample	k_{exp} (m/s) by Image	k_{exp} (m/s) by Optical Comparator
A3	6.26×10^{-5}	6.45×10^{-5}
B3	8.17×10^{-5}	6.83×10^{-5}

A decision was made to use the image-based volume method for final carbon concentration determination. It was not practical to etch all samples, nor was it practical to use the comparator for point extraction (extracting the points from a single projection took 30 minutes). As etching is destructive, a dissolved sample could be used for a dissolution data point or for microscopy but not both. A more precise method would be ideal, but one was not available. Therefore, the mass transfer coefficients reported in the following sections were calculated using final carbon concentrations determined exclusively by the image-based volume analysis method.

6.5.3 Quantitative Dissolution Results

The carbon concentrations and experimental mass transfer coefficients (k_{exp}) from the dissolution experiments are shown in Figure 6.9. The broken line denotes the literature correlation for this geometry and system. Trends between compositions varied between series: in Series 1 and Series 4, the rods dissolved in Fe-C-Ti-N had a k_{exp} near 2×10^{-5} m/s less than those dissolved into binary HM. This difference was less pronounced in Series 2 and Series 3; A3 had a smaller k_{exp} than experiment C3.

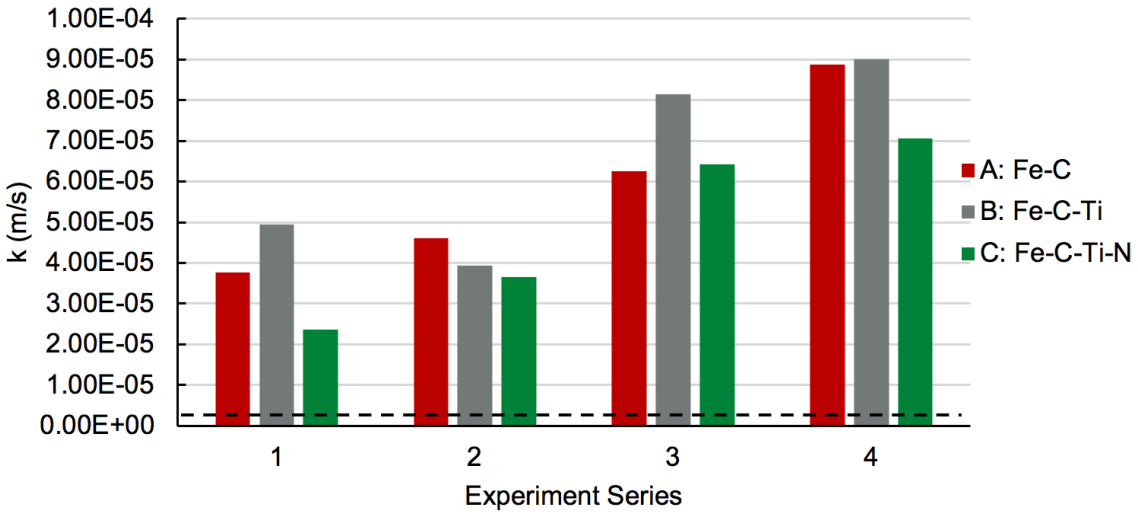

Figure 6.9. Experimental mass transfer coefficients for individual experiments, grouped by experimental series. The dashed line shows the predicted mass transfer coefficient from the literature correlation.

The dissolution experiments do not show the strong effect that Ti(C,N) was expected to have to align with industrial reports. Even for the most promising case, Series 1, k_{exp} of the rod dissolved in Fe-C-Ti-N was half of the others. While even a small reduction in mass transfer rate would become pronounced over the 20+ year blast furnace campaign, Ti additions have been have seen to promote drastic improvements in BF refractory condition (as in the case study above) rather than simply decreasing an average wear rate. Yet that is the only case showing a strong effect of Ti(C,N); in the remaining series, k_{exp} for dissolution into Fe-C-Ti-N was closer to values for samples without Ti(C,N).

The mass transfer coefficient generally increased with series number. This was attributed to changes in stirring assembly mentioned in the methods. The scatter between series made direct comparison difficult. To reduce the variation, a normalized k_{exp} was defined. This normalized value was k_{exp} of the individual experiment divided by the average k_{exp} for that series. For example, the normalized k_{exp} for C1 was taken by dividing k_{exp} of C1 by the average k_{exp} of A1, B1, and C1. The normalized k_{exp} values were averaged according to HM composition and shown with 95% confidence intervals in Figure 6.10. Normalized mass transfer coefficients for Fe-C were close to one. The mean k_{exp} for samples dissolved in Fe-Ti-C was also close to one but with more variation. The mean k_{exp} for samples dissolved in Fe-Ti-C-N was 0.828 ± 0.126. This resulted in a statistically significant difference in average k_{exp} between Fe-C and Fe-C-Ti-N but not between Fe-C and Fe-C-Ti or Fe-C-Ti and Fe-C-Ti-N.

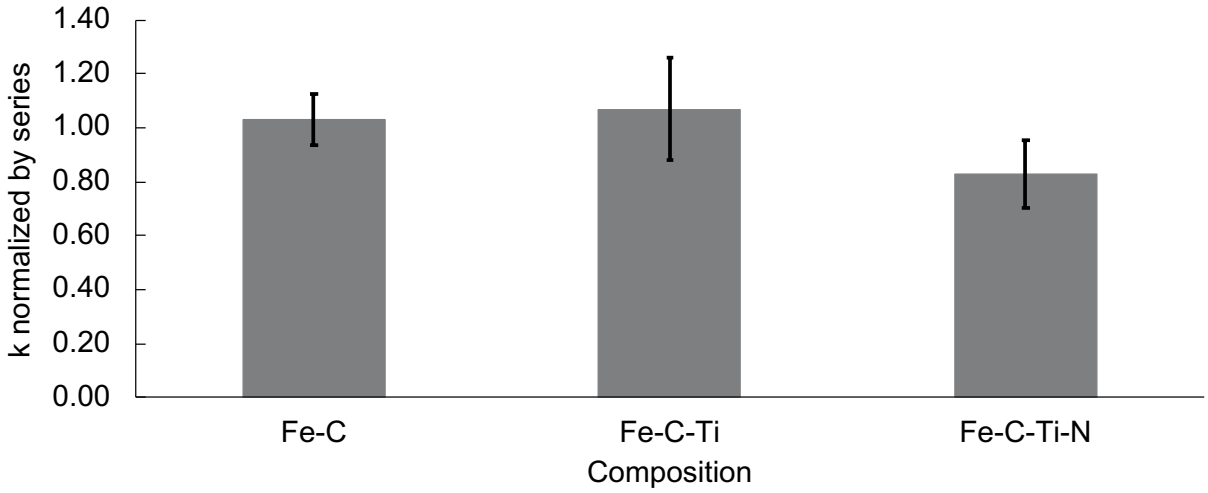

Figure 6.10. Normalized experimental mass transfer coefficients for each HM composition. Error bars show a 95% confidence interval on the mean.

Dissolution into Ti(C,N) containing HM did reduce the dissolution rate as compared to binary Fe-C, but this benefit was marginal. It was hypothesized that Ti(C,N) could form at the graphite interface, increasing the viscosity and reducing the interfacial area available for the dissolution reaction. To study this, cross-sections of the rods with adherent metal were examined. Most often micrographs appeared as that in Figure 6.11. The majority of Ti(C,N) were found in large agglomerations away from the interface. Ti(C,N) could be seen at the graphite interface but never as much as in the bulk. A second location of the sample, this time etched with nital, is shown in Figure 6.12. More Ti(C,N) particles appeared at this graphite interface, in part due to the dissolution of metal revealing more Ti(C,N). What is more telling is that Ti(C,N) agglomerations were not distinct particles but a connected network. The faceted shape of some individual Ti(C,N) particles can be seen; the cubic face was often interrupted by fusion with another particle. This morphology is consistent with the Ti(C,N) agglomerations seen in Ti bears of the BF [44]. This phenomenon could be evidence for why Ti(C,N) uniquely are able to protect the hearth. An agglomeration of solids should be better able to restrict flow than many smaller particles. This is particularly true when taking into account evidence that it is hard to localize Ti(C,N) to the hearth wall [28,45]. An accretion, having a larger mass, should require more force from liquid flow to remove it from a worn area as compared to small individual particles.

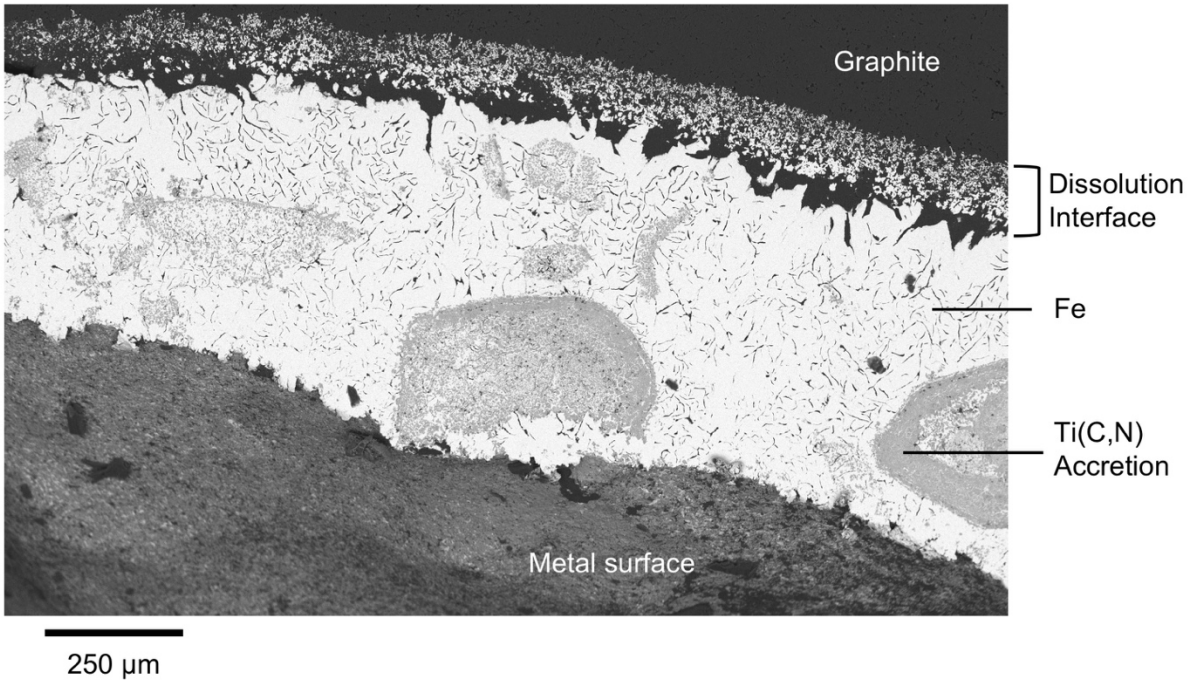

Figure 6.11. Cross-section of graphite rod C1 (dissolved in Fe-C-Ti-N)

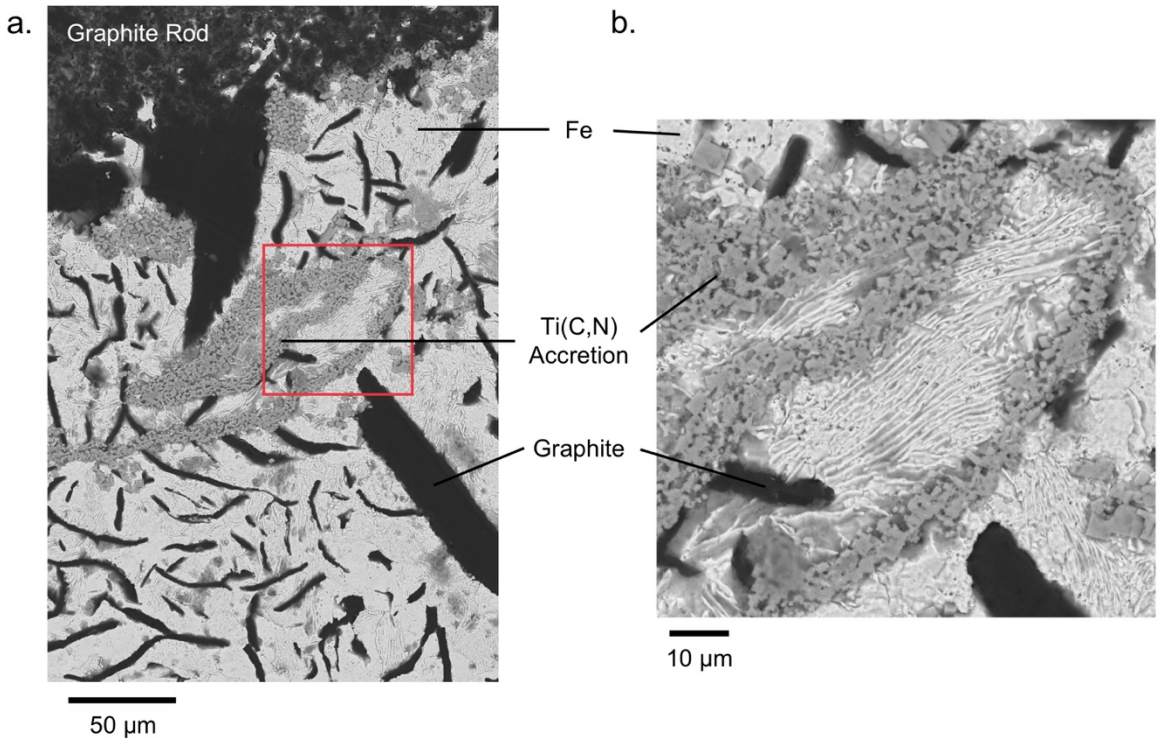

Figure 6.12. Back-scattered electron micrograph of a cross-section of graphite rod C1 etched with nital. a.) etched micrograph showing accretions in relation to graphite interface. b.) higher magnification view of the red box showing the Ti(C,N) agglomerations.

Bergsma and Fruehan's protection mechanism is an intersection of thermodynamics, heat transfer, and fluid dynamics [22]. Despite the findings here (that additions of Ti to HM minimally affect carbon dissolution), the strong evidence that Ti additions facilitate better refractory condition within the BF warrants more complex experimental investigation [18,19,46].

There were a number of simplifications contained in these experiments. BF HM contains more elements than just C, Ti, and N; carbon refractories have a more amorphous structure and contain impurities and binder material. Refractory is subject to a myriad of wear mechanisms besides dissolution, and the BF has larger thermal gradients. Heat transfer differences are expected to be the most important component missing in this study. These dissolution experiments were isothermal, but, according to Bergsma and Fruehan, a lower temperature is vital not just for the stability of Ti(C,N) but for the subsequent heat extraction needed to form the skull [22].

Of the various hearth degradation mechanisms, dissolution was the most likely to benefit from Ti additions without skull solidification. Dissolution rate is inversely related to viscosity for mass transfer-controlled dissolution, but the rate of degradation by gaseous species is unlikely to be reduced without formation of a protective layer. This points to the importance of heat extraction away from the hot face. Some of the retellings of Bergsma and Fruehan's protection mechanism minimize the effect of heat transfer, assuming that the hearth lining will be thin enough for this mechanism to activate [28,47]. Yet operators cannot wait until that occurs. Extracting heat from the hot face is vital. This has implications for choice of refractory at the start of the campaign, condition of refractory (prevention of an embrittled zone), and operation of cooling systems. The hypothesized method of protection needs adequate cooling to occur.

The small effect on dissolution and the behavior of Ti(C,N) particles should inform future work on this topic. Guo et al. have performed simulations of a BF during tapping to determine where Ti solids are expected to form [47]. Their 2D global simulations showed that Ti(C,N) primarily formed in the low velocity region opposite the taphole during tapping. A useful follow-up to this would be simulating local regions in 3D. A wear zone could be added to the hearth geometry to study how Ti injections through different tuyeres affect the solidification at the worn region.

6.5.4 Comparison of Dissolution to Literature Correlations

Mass transfer experiments are well characterized in literature. The literature mass transfer coefficient was between 2.80×10^{-6} and 2.81×10^{-6} m/s over the course of the

simulated dissolution. This was an order of magnitude smaller than the mass transfer coefficient determined by the experiments. For kinetics this was odd: a reaction cannot proceed faster than its slowest (rate-limiting) step. One likely explanation for this was the stirring assembly used. The mass transfer correlation assumed no rod movement other than axial rotation, i.e., there should be no pendulum-like motion or "wobble". There was around 110 cm between the stirrer and the bottom of the sample, and without perfect alignment (impractical with the current set-up), there was sure to be some wobbling of the sample. Extra motion of the sample should result in higher mass transfer rates due to the increased velocity and turbulence of the fluid. Series 3 and Series 4, those farthest from perfect rotational axial motion, had the highest k_{exp}, supporting this conclusion. A cold experiment dissolving salt rods in water was performed to test that the high k_{exp} was due to these non-idealities and not due to unexpected phenomena in the materials system.

Dissolution of salt (NaCl) into de-ionized water is mass transfer controlled [39,40] and can be used to compare the current set-up to the ideal characterized in literature. The procedure followed the graphite experiments only with the material substitution and lower temperature. The resultant dissolved salt rods are shown in Figure 6.13. Mass transfer coefficients (experimental and literature) from the salt dissolution experiments are shown in Table 6.7.

Figure 6.13. Photograph of salt rods after dissolution into deionized H_2O

Table 6.7. Mass Transfer Coefficients of Salt Rods

Initial Diameter (cm)	Post-dissolution Mass (g)	k_{exp} (m/s) [Eq. 2]	k_{lit} (m/s) [Eq. 4]
1.6	17.0944	2.14×10^{-5}	1.30×10^{-6}
2.1	33.7313	2.91×10^{-5}	1.45×10^{-6}

The literature correlation for an ideal rotating rod set-up was on the order of 10^{-6} m/s for the salt dissolution, but the k_{exp} values were an order of magnitude larger at 10^{-5} m/s. This order of magnitude difference is similar to that seen with graphite dissolution. The salt rods wobbled while stirring in the same way the graphite rods did. Rather than the higher graphite dissolution rates being an effect of porosity, microstructure, or another materials property, the higher k_{exp} can logically be attributed to the non-ideality of the stirring pattern. The grain size of the salt was large, resulting in a slightly faceted appearance, which may suggest some influence of interfacial control. However, partial interfacial control would only further slow the kinetics. It remains that k_{exp} was an order of magnitude larger than k_{lit}.

6.6 Conclusions

Dissolution of graphite rods into liquid hot metal of Fe-C, Fe-C-Ti, and Fe-C-Ti-N ingots was performed. A normalized mass transfer coefficient was defined to compare the dissolution rates between compositions. The average normalized mass transfer coefficient for dissolution into Fe-C-Ti-N was statistically significant compared to that of Fe-C, but no other pairs were significant. Even so, the reduction in dissolution rate from the formation of Ti(C,N) was small. Likewise, the reduction of dissolution by Ti(C,N) under isothermal conditions within the BF should be small.

These findings reinforce Bergsma and Fruehan's proposed mechanism. For isothermal dissolution, Ti(C,N) reduces the rate little. However, these experiments did not allow a skull to solidify, demonstrating that the importance of heat extraction to protecting the hearth with Ti.

6.7 Hypothesis Revisited

The formation of Ti(C,N) will decrease the dissolution rate of pure graphite 70% compared to a binary alloy and 30% compared to dissolved Ti alone.

This hypothesis was not supported. Dissolved Ti had no effect on the dissolution kinetics. The average normalized mass transfer coefficient of metal containing Ti(C,N) had a mean value 20% less than that dissolved in the binary alloy.

6.8 References

[1] A.J. Dzermejko: *Iron Steel Technol.*, 2015, vol. 12, 3 (March), pp. 58–70.
[2] V. Vogl, O. Olsson, and B. Nykvist: *Joule*, 2021, vol. 5, pp. 2646–62.
[3] Y. Li, T. Jian, T. Ma, M. Hu, L. Gao, and Y. Yang: *Metall. Res. Technol.*, 2020, vol. 117, p. 409.
[4] S. Silva, F. Vernilli, S. Justus, O. Marques, A. Mazine, J. Baldo, E. Longo, and J. Varela: *Ironmak. Steelmak.*, 2005, vol. 32, pp. 459–67.
[5] S. Biswas and D. Sarkar: in *Introduction to Refractories for Iron- and Steelmaking*, 2020, pp. 147–218.
[6] J. Stec, R. Smulski, S. Nagy, K. Szyszkiewicz-Warzecha, J. Tomala, and R. Filipek: *Ceram. Int.*, 2021, vol. 47, pp. 16538–46.
[7] M. Sun, J. Zhang, K. Li, S. Ren, Z. Wang, C. Jiang, and H. Li: *JOM*, 2019, vol. 71, pp. 4305–10.
[8] A. Preuer, J. Winter, and H. Hlebler: *Steel Res.*, 1992, vol. 63, pp. 139–46.
[9] K. Komiyama, B. Guo, H. Zughbi, P. Zulli, and A. Yu: *Metall. Mater. Trans. B*, 2014, vol. 45, pp. 1895–914.
[10] K. Shibata, Y. Kimura, M. Shimizu, and S. Inaba: *ISIJ Int.*, 1990, vol. 30, pp. 208–15.
[11] A. Dzermejko: *Iron Steel Technol.*, 2014, vol. 11, 3 (March),pp. 41–56.
[12] D. Jang, Y. Kim, M. Shin, and J. Lee: *Metall. Mater. Trans. B*, 2012, vol. 43B, pp. 1308–14.
[13] C. Wu and V. Sahajwalla: *Metall. Mater. Trans. B*, 2000, vol. 31B, pp. 243–51.
[14] X. Xing, S. Jahanshahi, J. Yang, and O. Ostrovski: *Arch. Mater. Sci. Eng.*, 2018, vol. 92, pp. 22–7.
[15] M. Sun, J. Zhang, K. Li, H. Li, Z. Wang, C. Jiang, S. Ren, L. Wang, and H. Zhang: *JOM*, 2020, vol. 72, pp. 2174–83.
[16] R. Wiblen, V. Sahajwalla, and C. Wu: *Ironmak. Conf. Proc.*, 2001, pp. 1005–13.
[17] S. Rao, R. Anand, L. Mallikarjun, L.R. Singh, Y. Gordon, M. Henstock, and W. Ying: in *AISTech Proceedings*, 2019, pp. 311–20.
[18] J. Huo and J. Huang: *Ironmak. (In Chinese)*, 2013, vol. 32, pp. 14–6.
[19] J.W. Entwistle, J. Grindey, R. Albanese, D. Lee, B. Rogers, T. Schrenk, M. McCoy, I. Cameron, M. Sukhram, M. Bodley, R. Midha, M. Al-Dojayli, K. Chomyn, Y. Ghobara, J. Busser, and P. Towsey: *Iron Steel Technol.*, 2020, vol. 17, 3 (March) ,pp. 64–74.
[20] Y. Zhao, D. Fu, L.W. Lherbier, Y. Chen, C.Q. Zhou, and J.G. Grindey: *Steel Res. Int.*, 2014, vol. 85, pp. 891–901.
[21] Y. Jomoto, B. Eto, Y. Kanayama, Y. Okuno, and M. Isoyama: *Tetsu-to-Hagane (In Japanese)*, 1965, vol. 51, pp. 1713–22.
[22] D. Bergsma and R.J. Fruehan: *60th Ironmak. Conf. Proc.*, 2001, pp. 297–312.
[23] T. Britt and P.C. Pistorius: *Trans. AIST*, 2022, vol. 19, 3 (March), pp. 292–7.
[24] R. Roscoe: *Br. J. Appl. Phys.*, 1952, vol. 3, pp. 267–9.
[25] J. Diao, L. Liu, W. Gu, P. Gu, G. Wang, and B. Xie: *Steel Res. Int.*, 2019, vol. 90, pp. 1–8.
[26] Y. He, Q. Liu, J. Yang, B. Yang, M. Long, H. Zheng, C. Liu, and M. Wei: *Adv. Mater. Res.*, 2011, vol. 146–147, pp. 1911–6.
[27] Y. Zhao, L. Lherbier, D. Fu, Y. Chen, C. Zhou, and J. Grindey: in *AISTech Proceedings*, 2012, pp. 457–69.
[28] Y. Zhao: *Iron Steel Technol.*, 2014, vol. 11, 3 (March) pp. 95–103.
[29] S. Street, A. Cheng, and I. Cameron: in *AISTech Proceedings*, 2019, pp. 275–88.
[30] Y. Deng, J. Zhang, K. Jiao, and Z. Liu: *ISIJ Int.*, 2019, vol. 59, pp. 1–8.
[31] D.R. Gabe, G.D. Wilcox, J. Gonzalez-Garcia, and F.C. Walsh: *J. Appl. Electrochem.*, 1998,

vol. 28, pp. 759–80.
[32] Y. Li, Y. Li, and R.J. Fruehan: *ISIJ Int.*, 2001, vol. 41, pp. 1417–22.
[33] F. Neumann, H. Schenck, and W. Patterson: *Giesserei*, 1960, vol. 47, pp. 25–32.
[34] K. Narita, M. Maekawa, T. Onoye, Y. Satoh, and M. Miyamoto: *Trans. Iron Steel Inst. Jpn.*, 1977, vol. 17, pp. 459–68.
[35] A. Rohatgi: *Webplotdigitizer: Version 4.5*, 2021.
[36] I. Jimbo and A.W. Cramb: *Metall. Mater. Trans. B*, 1993, vol. 24, pp. 5–10.
[37] Y. Kawai, Y. Shiraishi, N.T. Kyokai, N.G.S. Committee, and 140th Committee: *Handbook of Physico-Chemical Properties at High Temperatures*, 41st edn., Iron and Steel Institute of Japan, 1988.
[38] Y. Wanibe, S. Takai, T. Fujisawa, and Sakao: *ISIJ Int.*, 1982, pp. 560–5.
[39] C.J. De Blaey and H. Van der Graaff: *J. Pharm. Sci.*, 1977, vol. 66, pp. 1696–9.
[40] A. Tamas, R. Martagiu, and R. Minea: *Chem. Bull. "POLITEHNICA" Univ. Timisoara*, 2007, vol. 52, pp. 1–2.
[41] S.M. Badawy: *Desalin. Water Treat.*, 2016, vol. 57, pp. 11040–7.
[42] R.H. Perry: *Perry's Chemical Engineers' Handbook*, 7th edn., McGraw-Hill, New York, 1997.
[43] E.A. Guggenheim: *Trans. Faraday Soc.*, 1954, vol. 50, pp. 1048–51.
[44] C. Wang, K. Jiao, J. Zhang, and S. Wu: *ISIJ Int.*, 2021, vol. 61, pp. 138–45.
[45] B. Korthas, J. Hunger, V. Pschebezin, J. Adam, G. Harp, S. Kallio, R. Hurme, J.-O. Wikström, P. Hahlin, S. Wiedner, and others: *Eur. Comm. Dir. Res. Innov.*, 2007, pp. 1–140.
[46] K. Datta, P. Sen, S. Gupta, and A. Chatterjee: *Steel Res.*, 1993, vol. 64, pp. 232–8.
[47] B. Guo, P. Zulli, D. Maldonado, and A. Yu: *Metall. Mater. Trans. B*, 2010, vol. 41, pp. 876–85.

7 The effect of TiC, TiN, and Ti(C,N) dopants on the solidification of liquid Fe-C onto carbon refractory

7.1 Abstract

The blast furnace is the most productive way to reduce iron ore into hot metal. However, this method is limited by the performance of the hearth refractory. Industry has proposed and implemented the doping of carbonaceous hearth refractory with Ti containing materials, but the specific compound added may have implications for refractory performance. The literature lacks reports comparing the performance of TiC, TiN, and Ti(C,N). In this work, graphite rods coated with a coke analog and doped with TiC, TiN, or Ti(C,N) were dipped into a stagnant hot-metal bath to see if dopant affects the diameter and structure of solidified shells. Rods doped with TiN had the lowest average shell diameter, but rods doped with Ti(C,N) and TiC had average diameters not statistically distinct from one another. No interaction between HM and the dopants was observed, and it was unclear why rods doped with TiN performed differently. Excepting rods with TiN, the formation of the shell was fully heat transfer controlled.

7.2 Within the Narrative

Following the results of the previous chapter, it was determined that the next investigation of HM-graphite-Ti(C,N) interactions needed to be non-isothermal to more accurately reflect the conditions for Bergsma and Fruehan's mechanism to occur. This chapter shifts the frame of reference. Rather than directly investigating the protection mechanism, this investigation looks at the performance of different dopants in hearth refractory to improve skull formation. The composition of Ti(C,N) added to bricks may have an effect on hearth performance, but no reports have been made confirming or denying this. Observations from the skull formation behavior taken with the results from Ch. 6 are used to propose the kinetic limitations to BF skull formation.

The motivation to study the effect of Ti(C,N) composition on skull formation is due to differing properties between the pure forms: TiC and TiN. The solubility of components in HM is one of these differences. Therefore, the solubility plot is again included to provide support for this reasoning. The brief history of hearth refractory in the introduction of this section is also provided, similar to that contained in the literature review.

7.3 Introduction

In 2020, blast furnaces produced over 92% of the world's reduced iron [1]. Despite the rise in direct reduction techniques and the drive for carbon-free ironmaking, the blast furnace remains the most productive route globally to obtain iron. Yet even with the centuries of knowledge and research about utilizing the BF, challenges still exist. One such challenge is keeping the refractory in a good condition over the campaign life of the blast furnace. As the BF is a continuously operating counter-current reactor, the challenges to refractory systems are great. Refractory in the throat degrades mostly from abrasion, while refractory in the belly, bosh, and hearth are subject to degradation by thermal shock, chemical interactions, and vapor penetration [2]. Of these, the hearth is the most significant constraint on the campaign life of a blast furnace [2,3].

Prior to the 1960s, hearth bricks were made of chamotte, an aluminum silicate, and yielded a campaign life of around 10 years [2,4]. Modern blast furnaces use carbonaceous hearth refractories to achieve campaign lives over 30 years [2,5–7]. The use of carbon refractory was a major improvement due to its limited susceptibility to thermal shock, resistance to slag, ability to control porosity, and high thermal conductivity [2,4]. The latter is important because modern BF operational practice is to keep the hot face temperature below 1150 °C, so that a layer of iron (termed a skull) forms to protect the refractory [8]. While hearth refractory is best protected by this solidification, carbon brick developments have also improved degradation resistance. Beginning in 1981, metallic Si was added to limit the pore size within refractories [4]. This limited the penetration of the brick by liquid Fe and vaporous alkali species, thus minimizing the embrittlement of refractory. The industry also moved to using artificial graphite in carbon brick, due to the higher thermal conductivity [4]. All of these improvements extended the campaign life of BFs from 10 years to 20-30 years [9]. However, further improvements are possible, and initial findings show that doping carbon blocks with Ti or TiC can further improve the refractory life [9]. Ti materials were chosen based on the evidence that the hearth condition is improved when a small concentration of Ti content present in the hot metal in the hearth [10,11]. Bergsma and Fruehan proposed a mechanism that is commonly accepted by industry, which is detailed in Ch. 2 and Ch. 6. In brief, Ti additions can catalyze the solidification of a protective iron skull on the refractory hot face.

The success of Ti additions to improve the hearth longevity has led to experimentation with how Ti is introduced in the hearth. Street et al. reported seven ways to add Ti to the furnace, including charging TiO_2 through the bell, mixing TiO_2 with taphole clay, and adding Ti through the tuyeres [12]. This experimentation with

charge location revealed that there is an unanswered question of "how should Ti be charged to see improvements in the worn zone?". Korthas et al. investigated this question and found that the answer depended on the tapping schedule and location of the taphole [13]. They recommended that to maximize the effectiveness of TiO_2 addition during tapping, it should be added mid to late tap and upstream of the hot spot. Yet even after this collaboration of producers, there remain questions about the most effective location to add Ti in each scenario.

One location of particularly high refractory wear is the taphole. The taphole is one of the places of highest wear within the blast furnace, due to the high metal velocity and turbulence as metal exits the furnace [13,14]. This makes Ti-doped taphole clay an interesting case: Ti is introduced directly to the region where wear is occurring. Street reported improvements to hearth temperatures near the taphole during a trial of Ti-doped clay [11]. Korthas et al. and Oliveira et al. have also seen benefits of using Ti-doped taphole clay [13,15].

Ti-doped taphole clay is useful but – of course – can only be used at tapholes. However, this premise - that Ti materials can be added directly to the refractory at the location that needs protection - is useful and can be applied to the hearth brick. Nippon Steel has implemented this idea into hearth brick and has reported success, though the true test will be at the conclusion of the blast furnace campaign (that is, after several decades). Excepting Nippon Steel, little has been published on doping carbon blocks with Ti. There has been no report investigating which form of Ti results in the best refractory performance. Nippon Steel's patent reports doping bricks with either TiC or metallic Ti (which presumably carburizes to TiC or Ti(C,N) during processing) [16]. Utilizing TiC is interesting because TiC particles are not stable in the BF [17]; Ti(C,N) is the stable form [10,18]. The composition of these carbonitrides, as well the non-stoichiometry of pure TiC or TiN, could have implications for the refractory performance. This composition matters for two reasons: the first is thermodynamic stability, and the second is the differences in surface energy.

Ti(C,N) is a solid solution of TiC and TiN [19,20], and properties will change due to the wide variations in composition. Figure 7.1 shows the solubility of Ti in liquid Fe calculated by FactSage 8.1 [21]. Calculations were performed so that HM was saturated with nitrogen (for Ti(C,N) and TiN)) and carbon at all temperatures. Above the represented lines, the compound is stable where below only dissolved [Ti] will exist. In the BF, operating around 1 atm p_{N_2}, pure TiC is unlikely to form [22]. Ti(C,N) is the most thermodynamically stable, but TiN has similar stability (less than 0.05% wt Ti at

TiN saturation) at temperatures less than 1370 °C. Studies on excavated blast furnaces have confirmed that Ti(C,N) is the stable form within furnaces. The compositional differences have implication for interactions with both the refractory and the HM. Liquid iron wets TiC extremely well but will not wet stoichiometric TiN [23,24]. These differences in behavior reflect differences in surface energy. Different surface energies could also affect interactions with the refractory when processing. The ideal dopant would likely involve a compromise between surface energy and thermodynamic stability.

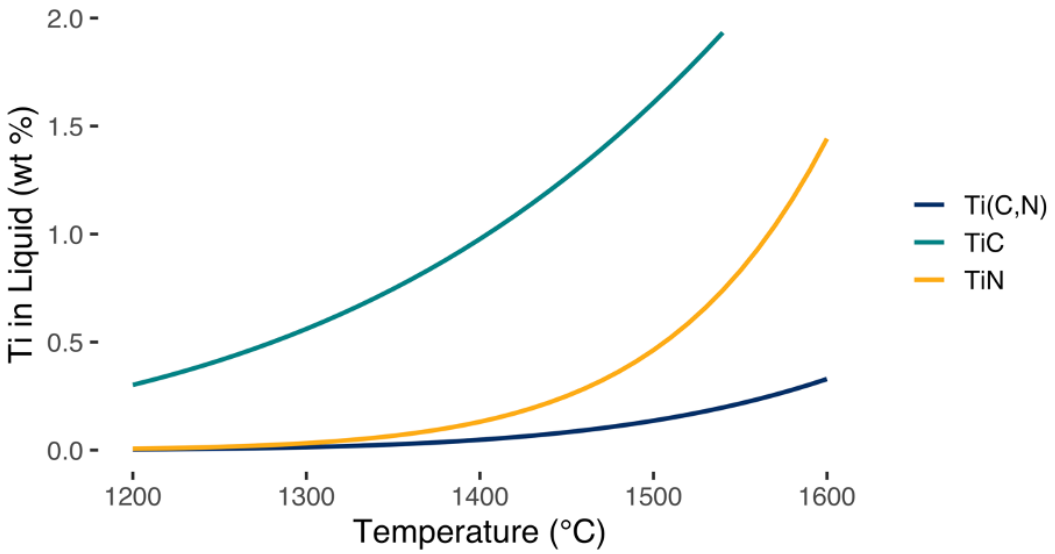

Figure 7.1. Stability of TiC, TiN, and Ti(C,N) as calculated by FactSage 8.1 [21]. Calculations were performed with 1 atm N_2 (for TiN and Ti(C,N)) and carbon concentration to ensure that the liquid was saturated with graphite. The equilibrium composition of Ti(C,N) varied from 50% at. TiN to 80% over the temperature range.

The role of Ti(C,N) in hearth protection is hypothesized to happen at the intersection of heat transfer, thermodynamics, and fluid dynamics [25]. Benefits would occur whether Ti(C,N) comes from the refractory or the HM [12]. The experiments presented here tested the ability of TiC, TiN, and Ti(C,N) to assist in iron shell formation on coated graphite rods. The expectation is that coated rods containing dopants (TiC, TiN, and Ti(C,N)) will solidify thicker shells than undoped rods. Out of the doped rods, the Ti(C,N)-containing one may form the thickest shell due to the greater stability of that compound.

7.4 Methods

7.4.1 Carbon Rod Dip Methods

Graphite rods of nominal 12.7 mm (0.5 in) diameter, 0.61 m (2 ft) long of grade "ME" were acquired from MWI, Inc. This grade was reported to have a density of 1.8 g/cm^3 with less than 0.6% wt ash content. Rods had an average diameter of 12.92 ± 0.03 mm. The rods were prepared with coatings as described below. Fe-C_{sat} was prepared by using an induction furnace to melt electrolytic iron in a graphite crucible under N_2. Fe-C_{sat} had composition near 5% wt [C] and 10 ppm [N] as detected by combustion analysis. To start the rod-dipping tests, pieces of Fe-C_{sat} (430 g) were placed in an Al_2O_3 crucible in a vertical tube furnace. The furnace was heated at 5 °C/min to 1200 °C under 0.93 L/min of gettered N_2. After reaching 1200 °C, the temperature was held for between 15 minutes and 2 hours, until CO gas was no longer detected by Dräger X-am 1700 handheld gas monitor. The furnace cap was removed, and the carbon rod was lowered to be immersed in the melt, touching the bottom of the crucible. After 45 s it was removed from the furnace and air cooled to room temperature. Dips with multiple rods were performed during a single melt, but the furnace cap was replaced between dips to restrict O_2 entrance to the furnace. A total of four melts were performed, with up to six rods immersed in a single melt.

Upon cooling, the diameter of the solidified shells was measured at 15 mm bellow the upper lip of the shell. This is shown in Figure 7.2. Four measurements were taken on each shell, each a 90° rotation from the last. The upper lip had slight variations in height, and measuring from the top lip at each side resulted in a different vertical position which helped to capture variations in the shell diameter, important due to the large curvature in this region.

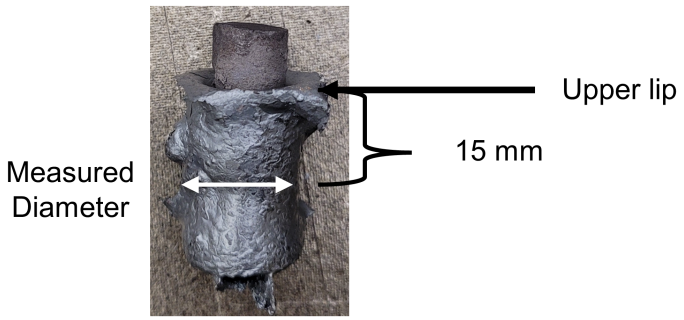

Figure 7.2. Example of solidified shell on a dipped graphite rod. The shell diameter was measured at a location 15 mm below the upper lip of the shell.

7.4.2 Experimental Considerations

It is unknown what amount of Ti(C,N) (in the solidified metal) would be needed to affect skull formation, but it was assumed to be small enough as to not affect the bulk thermal conductivity of solidified metal. Without an effect on bulk thermal conductivity, skull thickness should be the same for different coating compositions if thermal equilibrium is reached. Therefore, carbon rods must be immersed for a short enough time to capture any thickness differences resulting from transient interactions with the dopants. The dip also must be long enough to minimize differences in the initial transient, variable because the rods were manually immersed into the bath. Simulations were performed in QuikCAST to inform the choice of HM temperature and immersion time. Table 7.1 details the parameters used for the simulation. The latent heat of Fe was 271.7 kJ/kg, and the liquidus was 1148 °C, following that of the provided parameters for cast iron in QuikCAST. Simulations showed shell formation was highly sensitive to temperature; 1200 °C was chosen to enable a metal shell of measurable thickness to form without the shell impeding removal of the rod from the furnace. Figure 7.3 shows the simulated solidification at 1200 °C for time steps 15 s, 30 s, 45 s, and 100 s after immersion. The region in black is the solidified eutectic iron.

Table 7.1. Properties for QuikCAST Simulation

	Heat Capacity at Constant Pressure (J/kgK)	**Density (g/cm^3)**	**k at 1000 °C (W/m*K)**
Graphite	1575	1.50	41.4 [26]
Alumina	1149	3.99	6.15
Fe-C (eutectic)	830	750	27

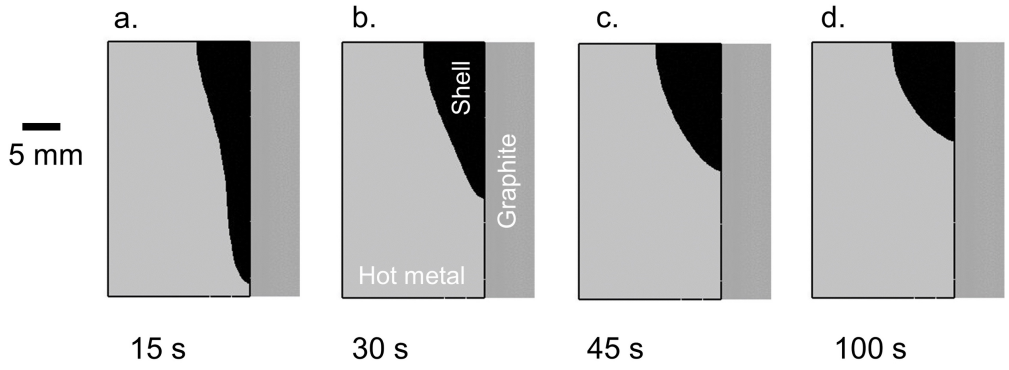

Figure 7.3. Results of QuikCAST simulation of the skull solidification. a.) solidification after 15s. b.) solidification after 30s. c.) solidification after 45s. d.) solidification after 100s.

The solid portion was elongated at short times (see the example at 15s) before partially remelting, becoming shorter and wider near 30s. This evolution continued to 45s, before remaining relatively consistent to 100s, the maximum time of the simulation. An immersion time of 45 s was chosen as a compromise, allowing enough to time to minimize the effects of the transient dip while not reaching the steady-state profile shown in Figure 7.3d. When trialing these experiments, many of the coated rods showed shells that extended the full immersed length of the rod, more similar to 15 s in the simulation. This can be attributed to the insulative properties of the coating, discussed in the following section. While the response of the shell was slower than the simulations, the comparison indicates that steady-state conditions were not reached during immersion. Immersion of 45 s was enough time to minimize the initial transient while not reaching thermal equilibrium.

7.4.3 Carbon Rod Preparation

Previous researchers developed coke analogs to have density, reactivity with CO_2, and dissolutive properties similar to that of industrial coke samples while being reproducible, homogeneous, and laboratory controllable – and hence able to be mixed with additives [27–30]. The coke analog formula from literature was modified to coat the graphite rods. These coatings were doped with TiC, TiN, and Ti(C,N) to test the propensity of the dopants to facilitate skull formation. This experiment was developed to test the effect of refractory doping. A trial where Ti-bearing materials were added directly to the melt resulted in a semi-solid cap on the melt, that could not be penetrated by the graphite rod.

The components used to make the coke analog are shown in Table 7.2 [29]. For the carbon mixture, 44% wt PolyFast - a phenolic resin base with graphite filler - was mixed with 56% wt graphite particles. For the liquid mixture, 45% wt Novolac was dissolved in 1-methoxy-2-propanol with magnetic stir bar over 7 days. The carbon mixture and liquid mixture were prepared for storage, rather than weighing each component on the day the analog was prepared. Propylene glycol methyl ether (1-methoxy-2-propanol) was expected to pyrolyze similarly to propylene glycol, despite having an extra alkane group and one less alcohol group per molecule. While pyrolysis reactions are complex to predict, the slight change in bonding is not expected to hinder these experiments.

The original coke analog formula was for pressed pellets; to more evenly coat the graphite rods, the formula needed to have a higher liquid fraction. Adjustments to the formula were based on changes in the volume fraction of the components. Table 7.3 shows the density values used in the mass to volume conversion. Values were from the

manufacture unless otherwise noted. The liquid was assumed to have the same density as base propylene glycol methyl ether, and densified values were used for solid materials. The density of the carbon mixture was obtained using a weighted average of graphite and PolyFast.

Longbottom's formula for pressed analogs had 50% liquid volume using the listed densities [27]. This formula was adjusted to 60% liquid volume to facilitate a more even coating. When including a dopant (TiC, TiN, or Ti(C,N)), less solid carbon mixture (PolyFast and graphite) was used to maintain a constant 60% liquid volume. Nippon Steel's patent for doping carbon refractories with Ti or TiC states that improvement happened when additions were between 5% and 20% by mass [16]. Thus, dopants were added in the range 8-13% wt.

Table 7.2. Mixtures for coke analog components

Component	% weight within class	Supplier
1-Methoxy-2-propanol	55% (of liquid)	Thermo Scientific
Novolac (solid)	45% (of liquid)	Sumitomo Bakelite Co.
Hexamethylenetetramine (HTMA)	3% (of total liquid)	Thermo Scientific
Graphite	56% (of carbon mixture)	Fisher
PolyFast (Bakelite)	44% (of carbon mixture)	Struers
TiC / TiN / Ti(C,N)	8-13% (of the total mixture)	Alpha / Alpha / Millipore Sigma

Table 7.3. Density of Coke Analog Materials for Volume Calculation

Component	Density (g/cm^3)
Bakelite (cured)	1.6
Graphite Particles	1.8
Solid Mixture	1.71
Liquid Mixture	0.926
TiC [31]	4.93
TiN [31]	5.43

To prepare the coke analog, the carbon mixture was weighed and, when applicable, mixed with a dopant. Liquid Novolac was weighed separately, and HTMA was added to an amount of 3% wt of the liquid. (HTMA dissolved and was not included in volume ratio calculations.) The solid components were mixed with the liquid components. This mixture was kneaded for 5 minutes to homogenize the mixture. SiC grinding paper (80 grit) was used to roughen the flanks and tips of the graphite rods. The coating was applied by taking the lump of kneaded material in the palm and rolling the end of the rod (~ 4 cm) in one direction into the coating, until the coating thickness appeared

homogeneous by eye around the rod circumference and over the coated length. This method was unable to create a perfectly homogenous coating, but measuring three coated rods for a total of 15 measurements resulted in an average diameter of 13.2 mm with a maximum of 14.2 mm.

The rods with green coatings were placed within a tube furnace and heated to 200 °C for 2 hr under Ar flowing at 0.93 L/min. The temperature was subsequently increased at 5 °C/min to 1200 °C and held for one hour before cooling at 5 °C/min to room temperature. This heat treating process followed that of Reid et al., who utilized a lower graphitization temperature than prior coke analog studies [28]. This temperature did affect densification: for trials of pressed samples (50% volume liquid), a maximum temperature of 1200 °C resulted in samples with 80% of the mass of the green mixture, rather than 58% when using a maximum temperature of 1600 °C [27].

A Panalytical Empyrean X-ray diffractometer was used to determine the lattice parameters of TiC, TiN, and Ti(C,N) based on the location of Cu Kα1 (1.5405 Å) and Kα2 (1.5444 Å) peaks. Scans were performed from 30° to 115° 2θ with step size of 0.0167° 2θ. Calculated lattice parameters were 4.3285 Å, 4.2802 Å, and 4.2401 Å for TiC, TiN, and Ti(C,N), respectively. This corresponded to near stoichiometric TiC and TiN, and $TiC_{0.5}N_{0.5}$ [32–35]. Raman spectroscopy was performed with an NT-MDT Ntegra Spectra and 532 nm laser, calibrated to a polyethylene sample with peak at 1001.4 cm^{-1}. Spectra were acquired with 600/600 grating and a 200 µm pinhole.

Changes to the coke analog formula included forgoing ball milling and pressing as well as the use of dopants and a slightly different resin. Without pressing (impractical to perform for these coatings), the coating contained porosity. This porosity created an increased thermal resistance. This, combined with a presumed interfacial contact resistance between the coating and the rod, can account for the slower solidification rate as compared to the QuikCAST simulations.

Use of the substitute resin and adjustment of the liquid proportion necessitated characterization of the coatings. Following the characterization of previous coke analog characterization, analogs are described by two characteristic ratios: I_V/I_G and I_D/I_G. I_G is the intensity of the G-band (around 1360 cm^{-1}), I_D is the intensity of D-band (around 1580 cm^{-1}), and I_V is minimum between bands [30]. Figure 7.4 shows these characteristic ratios for the rod coatings in this study and compares them to both metallurgical cokes and coke analogs presented by Aladejebi, and to the glassy carbon spectrum presented in Ch. 8 [30].

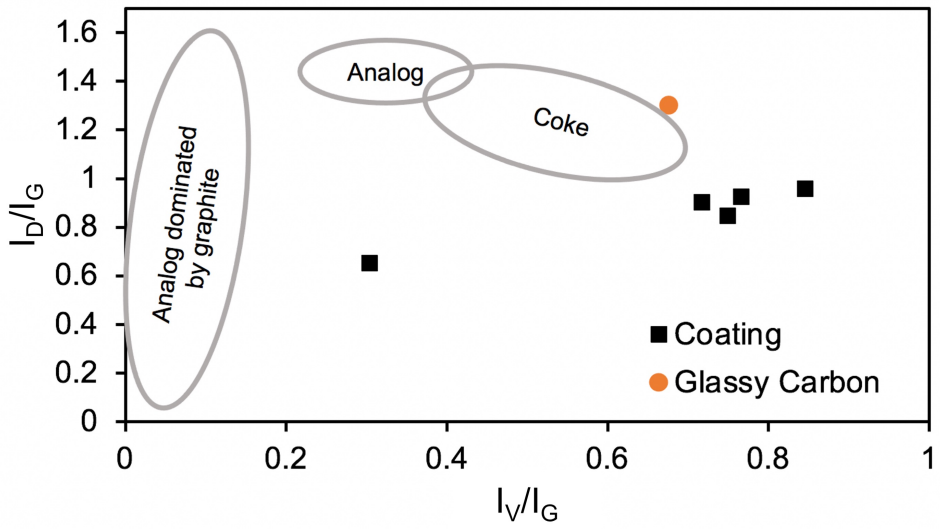

Figure 7.4. Characteristic ratios of Raman spectra of carbon coatings, glassy carbon, coke analogs, and metallurgical coke. The literature data are presented as ranges denoted by the circled regions [30].

I_D/I_G were less in coatings than seen in analogs , and I_V/I_G was higher for the coatings than previously observed. The former ratio is related to the annealing of graphite, with higher being more ordered [30]. I_D/I_G of the coating being less than the analogs can be attributed to the different heat treatments. The treatment here followed Reid et al. [28], but Aladajebi's process had an additional one hour hold at 1000 °C [30]. The longer time should allow more annealing of graphite, increasing the I_D/I_G compared to the present work. The I_V/I_G ratio is indicative of disorder in bonding. The higher ratio than coke analogs seems reasonable, as disorder would increase with an increase of pyrolyzed resin. These coatings had some inhomogeneity, and the isolated point is likely due to the sensor obtaining information from resin and a graphite particle at once. The characteristic ratios are outside of those previously measured coke analogs, but this is expected to affect the experiments minimally due to the lack of an observed interaction between the metal and the coating.

7.5 Results and Discussion

Figure 7.4 shows a macroscopic image of select rods. The solidified iron shells had many perturbations. Rods containing different dopants appeared similar with two exceptions. Rods doped with Ti(C,N) had a yellow color after dipping in the hot metal; rods doped with TiN generally had a red color after dipping. The second exception was the formation of shells. Shells consistently formed on uncoated rods, coated but undoped rods, and rods doped with TiC or Ti(C,N). However, shells were not observed on rods doped with TiN. Presumably, the shell did solidify but fell off upon removal from the HM. This was not observed visually, only inferred. To test this, a notch was

machined into the graphite rod before coating with a TiN-doped analog. This notched rod, shown in Figure 7.6a, rod resulted in a measurable shell (Figure 7.6b) but was the only TiN-containing rod to do so. Another notched rod coated with a Ti(C,N) containing analog was immersed in HM; conversely to the TiN result, this notched rod was the only Ti(C,N)-containing one that did not have an adherent shell upon removal from the furnace.

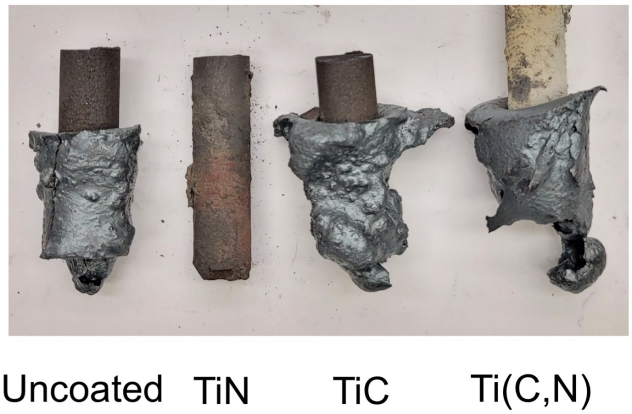

Figure 7.5. Macroscopic images of rods with solidified shells. Dopants are listed below the rod. Rod diameter is 12.92 mm.

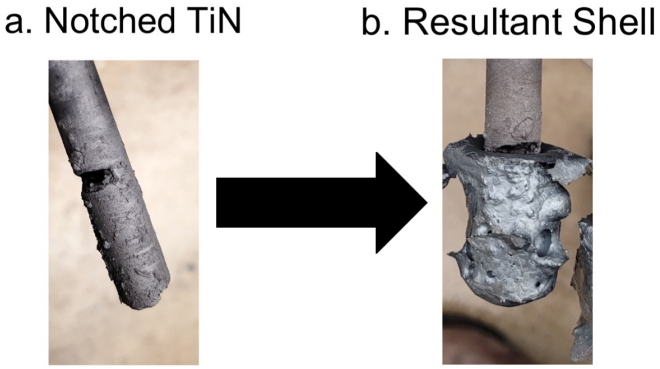

Figure 7.6. Result of the notched TiN-doped rod experiment. a.) Prior to immersion. b.) after immersion.

Figure 7.7 shows two representative cross-sections of the interfaces of the solidified shell and coating. The first (Figure 7.7a) shows a gap between the coating containing Ti(C,N) and the shell. At this location, the metal did not interact with the coating. Figure 7.7b shows contact between the coating containing TiC and shell at one point, surrounded by a gap. Most often, contact occurred at small areas rather than having large interfacial regions. While the region of coating directly contacting Fe appeared lighter, this was an effect of sample topography on backscattered electron imaging, rather than any compositional variation. These gaps would create a barrier to heat

extraction from the metal, providing more support for why the shell profile should deviate from the QuikCAST simulations.

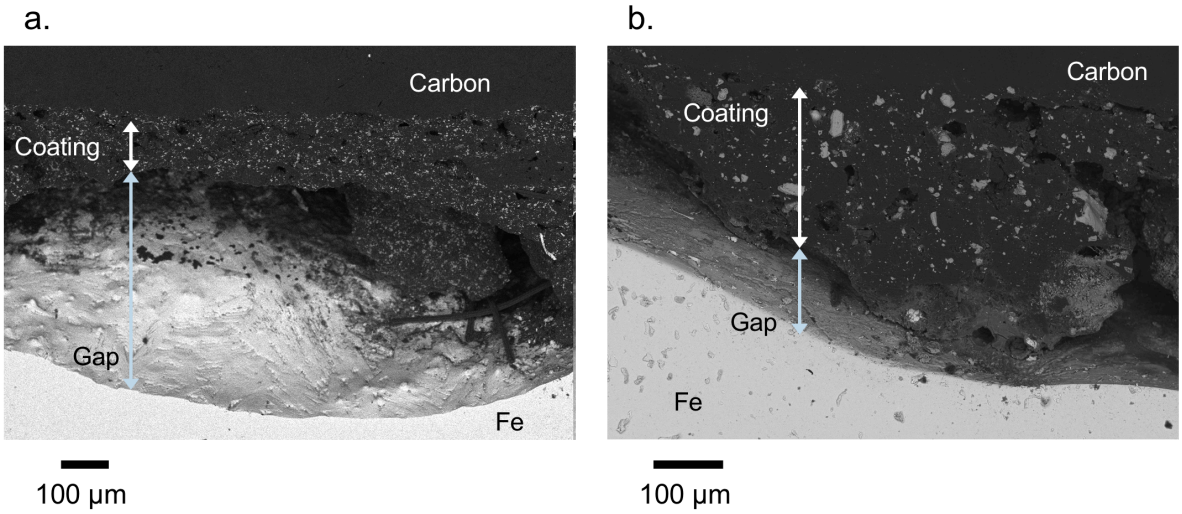

Figure 7.7. Back-scattered electron micrograph of cross-sections showing the two types of interactions between the coating-metal interfaces. a.) interface with a gap between the metal and Ti(C,N) coating. b.) interface with the metal contacting the TiC coating at one point. Both of these interfaces were present on each rod that solidified a shell, regardless of the dopant.

Table 7.4 shows the average diameter of shells formed after 45 s of immersion in HM. Measurements assumed homogeneous coatings, but some measurements were excluded because they appeared to be over a trapped gas pocket. The number of samples and measurements included are listed due to those exclusions. Figure 7.8 shows the average diameter of shells grouped by coating type. Error bars represent a 95% confidence interval on the mean.

Table 7.4. Rod Shell Diameters

Coating Type	Average Diameter ± 95% C.I. (mm)	Samples	Total Measurements
Uncoated	19.20 ± 0.49	1	4
Undoped	18.18 ± 0.90	3	10
TiC	18.28 ± 0.99	3	12
TiN*	15.01 ± 1.83	4*	16
Ti(C,N)*	17.35 ± 2.25	3*	11

* Denotes that a notched rod was included in the measurement

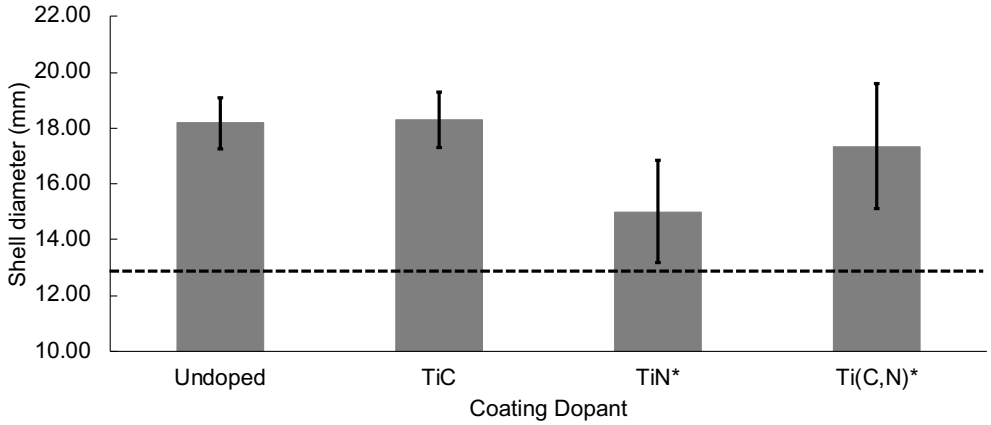

Figure 7.8. Average diameters of shells formed after immersion for 45 sec in molten carbon-saturated iron. Error bars are 95% confidence intervals. The rod diameter prior to coating and immersion was 12.92 mm and is shown by the notched line. Asterisk (*) denotes that a notched rod was included in the results.

Excepting coatings with TiN, shell diameters were similar between coating types. It was thought that rods doped with Ti(C,N) would result in shells with larger diameters than uncoated or undoped rods. However, the rod to form the shell with largest diameter was the uncoated rod. This supports the idea that the coatings slow heat transfer, due to the effects discussed earlier, though only a single uncoated rod was tested. Considering coated rods only, the difference in average diameter was statistically significant only between the TiC and TiN pair and the undoped and TiN pair, determined by t-test. There was no significant difference between the average diameters of the TiC:Ti(C,N) pair or the TiN:Ti(C,N) pair. TiN was so distinct because only one immersion test resulted an adherent shell. The rods with TiN are thought to form shells, but the shells fall off upon removal from the melt, evidenced by the notched rod result with TiN. Why those shells fell off was unclear. Figure 7.9 shows back-scattered electron micrographs of the rod-coating-metal interface for rods of three different dopants. If an interaction between the metal and dopant was affecting the shell thickness, there should be evidence of the metal interacting with the dopant particles at the microscopic level. Yet this was not seen for any of the dopants. Despite the strong wetting reported between liquid Fe and Ti(C,N) [23], no interaction was seen between these particles and the metal, nor in the cases of TiC and TiN. Rather, the dopants appeared to remain embedded in the analog coating without contacting the metal. These micrographs show little reason why shells should remain on TiC and Ti(C,N) containing rods while falling off of TiN containing rods. In the context of Nippon Steel's bricks containing TiC [4,16], these micrographs suggest that the reported benefit in refractory life may not occur from HM wetting TiC.

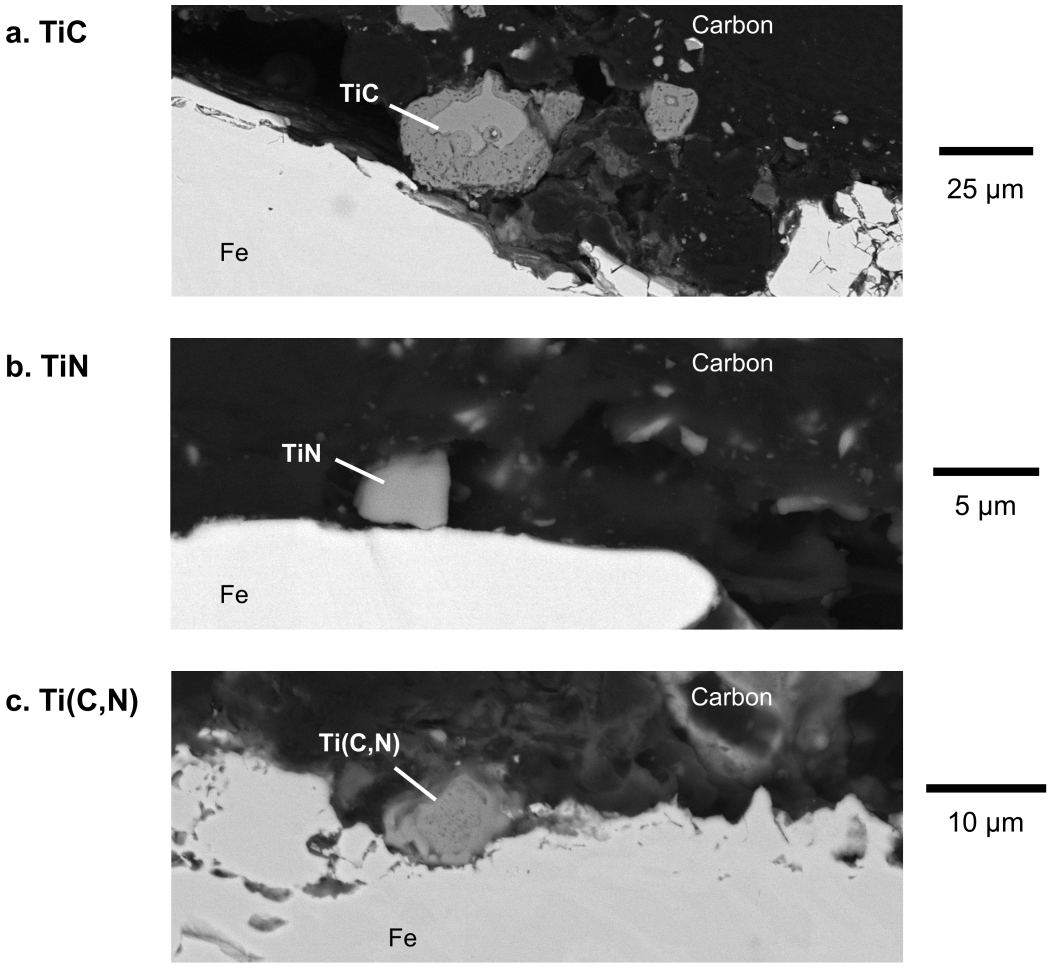

Figure 7.9. Backscattered electron micrographs of the rod-coating-metal interface. The metal does not contact the TiC (a.), TiN (b.), or Ti(C,N) (c.) particles. Note that the TiN particle was observed in the experiment using a notched rod, the only one to form a measurable shell.

With the present understanding, doping hearth refractory with TiN should be avoided. If Bergsma and Fruehan's mechanism is correct (with Ti(C,N) filling in worn places within the furnace and helping a shell to solidify) the shell must stay in place to protect the hearth. If the shell formed on TiN-doped carbon slid off the refractory, the hearth would be left unprotected. It is a possibility that an interaction between TiN and the coating occurred during firing (changing the composition of the dopant), but no evidence of such interaction was seen with microscopy. Such an interaction would be relevant to industry, since similar reactions may occur between dopants and the carbonaceous binder in hearth bricks. Regardless of the reason for poor shell adherence to TiN, it represents an additional obstacle to localizing the shell in the hearth region, and obstacle that could be best avoided by using TiC or Ti(C,N) instead – especially given the already reported practical difficulties with localizing the effects of Ti additions in the hearth region [13].

Excepting TiN, it cannot be said that one dopant was better at forming shells than another. It was thought that the varying properties of the dopants would have an effect on the shell thickness, but that was not observed. Despite Ti(C,N) being the most stable form in the BF, no statistically significant difference was seen between the shells on rods doped with Ti(C,N) versus those doped with TiC or even those undoped. However, the lack of significance between those undoped and those doped reveals the limitation of these experiments: formation of the shell was heat transfer controlled. That is, the slowest step to solidify metal was the time needed to extract heat (by conduction into the graphite rod). This is probably a departure from BF conditions, at least when Ti is present.

The present experiments contained thermal gradients and conditions that ensured stability of the dopants, but the melt was stagnant. In the dissolution experiments of Ch. 6, a graphite rod that was immersed in undersaturated iron, but not rotated, did not exhibit measurable dissolution. Because graphite dissolution is mass transfer controlled [36,37], little dissolution resulted from limited fluid motion. Bergsma and Fruehan's hypothesized protection mechanism is a complex intersection of heat transfer, thermodynamics, and fluid dynamics [25]. The lack of flow in these experiments was important: the formation of an iron skull based solely on heat transfer can be expected to be different from skull formation with imposed flow; in the latter case, the flow restriction provided by precipitated Ti(C,N) would be expected to aid skull formation.

In the BF, solidification of an iron skull is heat transfer controlled. When including Ti, the rate-limiting step is not clear. Ti-assisted skull formation could be heat transfer limited, but it could also be under mixed control, limited by both heat extraction and the formation of Ti(C,N) at the hot face. A more explicit statement of the second case is that skull formation is "limited by the presence of enough Ti(C,N) at the hot face to restrict metal flow". By the Einstein-Roscoe relation, a higher concentration of solid (Ti(C,N)) would increase the effective viscosity, thus restricting metal flow [38]. Not just concentration but also morphology is important: larger clusters of Ti(C,N) would more effectively restrict flow to the hot face than would a random distribution of unconnected particles. Obtaining the "critical concentration" and morphology of Ti(C,N) is complicated due to the dynamic nature of the BF. Ti(C,N) could form in the bulk HM and move to the hot face or could form directly at the hot face. Even if a critical concentration formed at the hot face, Ti(C,N) could be carried away by HM flow until the time the skull actually solidifies. Independent of where Ti(C,N) forms, the critical concentration must remain at the hot face until the skull solidifies. For this

reason, it is likely that Ti-assisted formation of a skull (termed a titanium "bear" by industry) is under mixed control.

While not proven, Ti bear formation being under mixed control could shed light on the questions raised by blast-furnace operators. Zhao questioned why Ti(C,N) should form in proximity to the refractory hot face [17]. The possibility of chemical adhesion was discussed in Ch. 5. If adhesion does not occur, formation under mixed control can explain why forming a bear is difficult. Buoyancy of Ti(C,N) particles and rapid HM flow can continually remove Ti(C,N) from the hot face if a bear has not already formed, even if the hot face temperature is low enough to form Ti(C,N). The velocity of HM is one reason why Korthas et al. recommended charging Ti upstream of the worn region when tapping [13].

Whether the formation of a Ti bear is heat transfer controlled, controlled by reaching a critical concentration of Ti(C,N), or a mixture of these, each of these scenarios can be expedited by increasing heat extraction at the hot face. During the campaign, this is not so much "increasing heat extraction" as it is ensuring that the cooling systems in place are functioning correctly. Problems with grouting, cooling systems, and the loss of thermal conductivity due to embrittled zones in the refractory can all limit heat extraction, reducing the ability to protect the refractory [4,14]. Enough heat must be able to be extracted to reach a critical concentration of Ti-based precipitates, which would reduce flow so that iron can then be solidified.

7.6 Conclusions

Graphite rods were coated with coke analogs that were either undoped or doped with TiN, TiC, or Ti(C,N). These rods were immersed in liquid hot metal to test the propensity of each dopant to help in solidifying an iron shell. There was no statistically significant difference in the average shell diameter between undoped rods and those doped with TiC or Ti(C,N). However, the average shell thickness of rods doped with TiN was distinct from that of TiC. Rods doped with TiN often had no shell when removed from the melt. These were thought to solidify shells within the melt that fell off upon removal from the liquid. Based on this result, industry should avoid doping hearth refractory with TiN without further investigation. Why these shells fell off remains unclear; microscopy of the interfaces showed no interaction between the hot metal and any of the dopant particles (not just with TiN). The formation of shells in these stagnant melts was heat transfer controlled, but a discussion is presented that the rate of Ti bear solidification in the BF is plausibly under mixed control: a combination of

heat transfer and reaching a critical concentration of Ti(C,N). Regardless of the rate limiting step, effective heat extraction from the refractory hot face is vital.

7.7 Hypothesis Revisited

Doping coke analog coated graphite rods with 10% TiC will result in the formation of statistically significantly thicker solid iron shells, compared with undoped coatings or those containing Ti(C,N) or TiN.

Partially Supported: the shell diameter for coatings containing TiC were statistically significantly larger only compared with TiN, not compared with those undoped or containing Ti(C,N).

7.8 References

[1] Worldsteel: *World Steel in Figures Report 2021*, 2021.
[2] S. Biswas and D. Sarkar: in *Introduction to Refractories for Iron- and Steelmaking*, 2020, pp. 147–218.
[3] A. Dzermejko: *Iron Steel Technol.*, 2014, vol. 11, 3 (March), pp. 41–56.
[4] M. Nitta and K. Hatakeyama: *Nippon Steel Tech. Rep.*, 2020, pp. 40–4.
[5] S. Filatov, I.F. Kurunov, Y. Gordon, A. Sadri, and W. Ying: in *AISTech Proc.*, 2016, pp. 695–704.
[6] F. Kerkhoven, J. Stuurwold, G. Tijhuis, B. Nugteren, and R. van Laar: *Iron Steel Technol.*, 2022, vol. 19, pp. 70–9.
[7] V. Vogl, O. Olsson, and B. Nykvist: *Joule*, 2021, vol. 5, pp. 2646–62.
[8] A. Dzermejko: *Iron Steel Technol.*, 2014, vol. 11, 3 (March), pp. 41–56.
[9] M. Nitta, H. Nakamura, and A. Ishii: *Nippon Steel Tech. Rep.*, 2008, vol. 388, pp. 49–54.
[10] K. Narita, M. Maekawa, T. Onoye, Y. Satoh, and M. Miyamoto: *Trans. Iron Steel Inst. Jpn.*, 1977, vol. 17, pp. 459–68.
[11] S. Street, C. Copeland, and E. Worral: in *AISTech Proceedings*, 2013, pp. 381–403.
[12] S. Street, A. Cheng, and I. Cameron: in *AISTech Proceedings*, 2019, pp. 275–88.
[13] B. Korthas, J. Hunger, V. Pschebezin, J. Adam, G. Harp, S. Kallio, R. Hurme, J.-O. Wikström, P. Hahlin, S. Wiedner, and others: *Eur. Comm. Dir. Res. Innov.*, 2007, pp. 1–140.
[14] S. Silva, F. Vernilli, S. Justus, O. Marques, A. Mazine, J. Baldo, E. Longo, and J. Varela: *Ironmak. Steelmak.*, 2005, vol. 32, pp. 459–67.
[15] T. Moreira de Oliveira, W. Headrick Jr., F. Nonaka, and A. Simões Ribeiro: in *AISTech Proceedings*, 2022, pp. 1495–501.
[16] H. Inoue, M. Nitta, T. Matsui, T. Wakasa, Y. Yamagami, and T. Mochida: *United States Pat.*, Patent #8889062, Nippon Steel and Sumitomo Metal Corporation, 2014.
[17] Y. Zhao: *Iron Steel Technol.*, 2014, vol. 11, 3 (March) ,pp. 95–103.
[18] C. Wang, K. Jiao, J. Zhang, and S. Wu: *ISIJ Int.*, 2021, vol. 61, pp. 138–45.
[19] K. Frisk: *Calphad Comput. Coupling Phase Diagrams Thermochem.*, 2008, vol. 32, pp. 326–37.

[20] V. Ivanchenko and Materials Science International Team: *C-N-Ti Ternary Phase Diagram Evaluation*, in Springer Materials.
[21] C.W. Bale, E. Bélisle, P. Chartrand, S.A. Decterov, G. Eriksson, A.E. Gheribi, K. Hack, I.H. Jung, Y.B. Kang, J. Melançon, A.D. Pelton, S. Petersen, C. Robelin, J. Sangster, P. Spencer, and M.-A. Van Ende: *Calphad*, 2016, 54, vol. 54.
[22] K. Datta, P. Sen, S. Gupta, and A. Chatterjee: *Steel Res.*, 1993, vol. 64, pp. 232–8.
[23] P. Alvaredo, M. Dios, B. Ferrari, and E. Gordo: *J. Alloys Compd.*, 2019, vol. 770, pp. 17–25.
[24] I. Chumanov and A. Anikeev: *Russ. Metall.*, 2016, vol. 2016, pp. 1145–7.
[25] D. Bergsma and R.J. Fruehan: *60th Ironmak. Conf. Proc.*, 2001, pp. 297–312.
[26] W.D. Kingery, J. Francl, R.L. Coble, and T. Vasilos: *J. Am. Ceram. Soc.*, 1954, vol. 37, pp. 107–10.
[27] R.J. Longbottom, B.J. Monaghan, M.W. Chapman, S.A. Nightingale, J.G. Mathieson, and R.J. Nightingale: *Steel Res. Int.*, 2011, vol. 82, pp. 505–11.
[28] M.H. Reid, M.R. Mahoney, and B.J. Monaghan: *ISIJ Int.*, 2014, vol. 54, pp. 628–33.
[29] M.W. Chapman: *Insoluble oxide product formation and its effect on coke dissolution in liquid iron*, University of Wollongong, 2009.
[30] O.A. Aladejebi: *Effect of Minerals on Coke Analogue Carbon Bonding and Reactivity*, University of Wollongong, 2017.
[31] J. Shackelford, Y. Han, S. Kim, and S. Kwon: *CRC Materials Science and Engineering Handbook*, 4th edn., CRC Press, 2016.
[32] N. Frage, N. Froumin, M. Aizenshtein, L. Kutsenko, D. Fuks, and M. Dariel: *Solid State Mater. Sci.*, 2006, vol. 9, pp. 189–95.
[33] Y.F. Yang, H.Y. Wang, J. Zhang, R.Y. Zhao, Y.H. Liang, and Q.C. Jiang: *J. Am. Ceram. Soc.*, 2008, vol. 91, pp. 2736–9.
[34] J.H. Kang and K.J. Kim: *J. Appl. Phys.*, 1999, vol. 86, pp. 346–50.
[35] G. Neumann, R. Kieffer, and P. Ettmayer: *Monatshefte fur Chemie*, 1972, vol. 103, pp. 1130–7.
[36] D. Jang, Y. Kim, M. Shin, and J. Lee: *Metall. Mater. Trans. B*, 2012, vol. 43B, pp. 1308–14.
[37] C. Wu and V. Sahajwalla: *Metall. Mater. Trans. B*, 2000, vol. 31B, pp. 243–51.
[38] R. Roscoe: *Br. J. Appl. Phys.*, 1952, vol. 3, pp. 267–9.

8 Catalytic Graphitization of Glassy Carbon and Coke Analogs by Molten Fe-C_{sat}

This chapter modified from its original form in the journal
Metallurgical and Materials Transactions B:

T. Britt and P. C. Pistorius, "Catalytic Graphitization of Glassy Carbon by Molten Fe-C_{sat}," *Metall. Mater. Trans. B*, vol. 52, no. 1, pp. 1–5, Feb. 2021.
DOI: 10.1007/s11663-020-02003-7.

8.1 Abstract

The campaign life of blast furnaces can be greatly limited by the interactions of carbon walls with liquid Fe-C_{sat}. Numerous carbon forms have been investigated but not glassy carbon. In this work, liquid Fe-C_{sat} catalyzed the graphitization of glassy carbon crucibles heated in a high-temperature confocal scanning laser microscope. Graphitization created readily wetted pores into which the hot metal penetrated, possibly similar to the embrittlement layer seen in blast furnace hearth refractory.

8.2 Within the Narrative

It is proven that the crystallinity of carbonaceous hearth refractory affects performance over campaign life. The interaction of glassy carbon with Fe-C_{sat} has not been studied previously. Depending on how the two phases interact, glassy carbon could see potential use as either a laboratory coke analog or a thin cladding for protection of industrial hearth refractory. Glassy carbon, despite the economic flaws mentioned, was thought to be beneficial due to a low gas permeability. Laboratory coke analogs have been seen to contain glassy carbon, and this structure might contribute to the catalytic graphitization of cokes. The catalytic graphitization of cokes has also been observed in industry, and a discussion is made comparing the graphitization of coke and glassy carbon. Finally, though not documented in Ch. 10, it was hypothesized that the use of these crucibles could be used to observe TiC precipitation within the CSLM.

8.3 Introduction

Long blast furnace (BF) campaign lives (of greater than 20 years) rely on careful choice of the carbon refractory materials that are used to construct the blast furnace hearth [1]. A common design philosophy is to ensure that the hot-face temperature of the refractory is below 1150 °C (the eutectic temperature in the iron-carbon system), to ensure solidification of a protective iron-carbon skull between the refractory and the liquid hot metal [1]. Low hot-face temperatures are achieved by cooling the hearth wall and using higher-conductivity, graphitic carbonaceous refractory [2]. However, some wall wear does occur, particularly in areas of higher flow rate near tap holes, where the elevated heat transfer rate can cause temporary loss of the solidified skull during tapping. While the rate at which the exposed carbon dissolves into undersaturated hot metal is often assumed to be under liquid-phase mass transfer control [3], the structure of the carbonaceous refractory is also considered to affect its dissolution rate: graphitic material is generally not used at the hot face because of its higher dissolution rate in molten iron than less-crystalline materials such as semi-graphitized carbon [2]. An effect of the crystallinity of coals and graphite on their dissolution rate in liquid iron was reported [4], though differences in mineral and sulfur content (of the carbonaceous material) strongly affect dissolution rates [5,6].

Given the possibly confounding effect of inorganic material when studying the dissolution of less-crystalline carbons, glassy carbon (vitreous carbon) is a potentially interesting material. Glassy carbon would not be practical as a large-scale refractory lining (given its high cost, low fracture toughness, and low thermal conductivity). However, its high purity and less-crystalline structure would be expected to affect its dissolution behavior, and so could serve to test the proposed link between crystallinity and dissolution.

The density of glassy carbon is approximately 35% lower than that of graphite [7]. While most of the bonds in glassy carbon are sp^2 (as in graphite), glassy carbon is thought to be comprised of small, single graphite-like sheets which entangle due to curvature from non-6-member rings [8,9]. The structural difference results in a higher Gibbs free energy of carbon in glassy carbon than in graphite, causing higher solubility of glassy carbon than graphite in liquid nickel [10] (and in other liquid metals). The solubility difference was found to cause destruction of glassy carbon in contact with various liquid metals [11]: the glassy carbon dissolved in the liquid metal, and then reprecipitated as graphite (in a process termed "catalytic graphitization").

In addition to constraints imposed by the cost, low toughness and low thermal conductivity of glassy carbon, catalytic graphitization of the material by graphite-saturated liquid iron would preclude its use as a practical refractory. The results presented here were used to test whether graphite-saturated liquid iron does catalyze graphitization of glassy carbon, and whether the large density difference between glassy carbon and graphite affects the nature of the interaction.

8.4 Methods

Graphite-saturated iron was first prepared by melting electrolytic iron in a graphite crucible (internal diameter 50 mm) with an induction furnace, sampling the metal after 10 minutes at 1550 °C (using a fused-quartz tube with an internal diameter of 4 mm). This holding time was sufficient to saturate the metal with carbon, as illustrated by the presence of primary cementite in the solidified microstructure (Figure 8.1).

In each graphitization test, approximately 0.15 g of the alloy was sectioned and placed in a dense type-B glassy carbon crucible provided by Sigradur (outer diameter 5 mm, height 8 mm, thickness 0.5 mm), within a thick-walled (3 mm) alumina crucible placed on a B-type thermocouple in a high-temperature confocal scanning laser microscope (CSLM). Four melting tests were performed with maximum temperatures and holding times as in Table 8.1. The samples were heated to 300 °C at 50 °C/min, held for 1 minute, and heated at 400 °C/min to 1350°C (or to 1235 °C for the "LT" test); samples in "HT" tests were then heated at 150 °C/min to 1485 °C. All samples were heated in an argon atmosphere with p_{O_2} less than 10^{-21} atm. The metal for sample HTc was pre-melted in a graphite crucible, by heating in the CSLM to 1550 °C for 15 minutes; this caused the metal to consolidate into a near-spherical droplet that could subsequently be melted in a glassy-carbon crucible without the metal touching the crucible walls.

Table 8.1. Experimental Parameters

Sample	Maximum Temperature (°C)	Hold Time (min)	Notes
HT	1485	10	High temperature
HTe	1485	10	High temperature; crucible heated empty (without metal)
HTc	1485	10	Pre-carburized droplet at high temperature
LT	1235	30	Low temperature

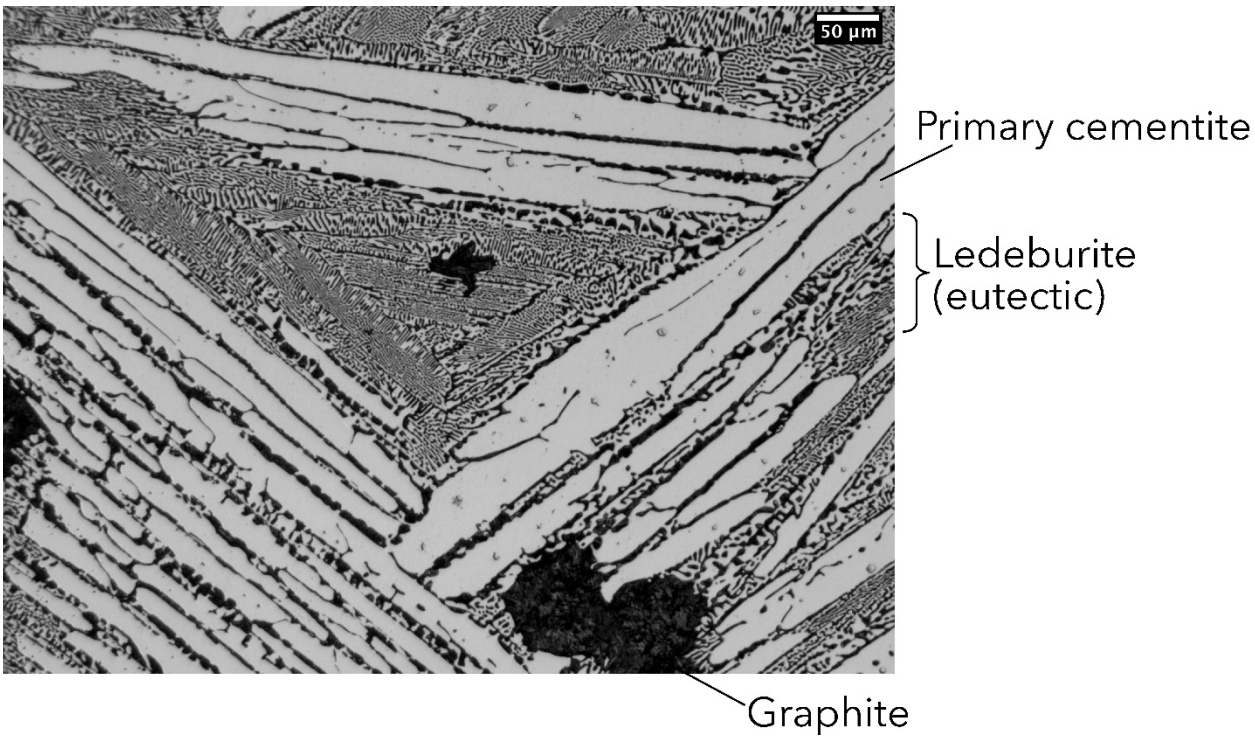

Figure 8.1. Room-temperature microstructure of the carbon-saturated iron used in the graphitization experiments (optical micrograph; etched with nital).

The temperature of the CSLM is normally calibrated by recording the temperature at which pure metals melt, but interactions between carbonaceous crucibles and most metals prevent the melt of a pure metal. Pure copper (melting point 1085 °C) was seen to melt at 1085 °C within a glassy-carbon crucible.

X-ray diffraction (XRD) was performed with a PANalytical X'Pert Pro MPD (Cu anode) to characterize the transformation from glassy carbon to graphite. Scans were performed from 14-50° 2θ with a step size of 0.0262° 2θ. The crucibles were mounted horizontally in a clay holder with their long axis perpendicular to the incident beam. Carbon bonding in the crucible was characterized with Raman spectroscopy, using an NT-MDT Ntegra Spectra, 532 nm laser, and 200 nm pinhole, calibrated to a polyethylene sample with peak at 1001.4 cm^{-1}.

8.5 Results and Discussion

Every crucible heated while containing Fe-C_{sat} showed a visible change upon removal from the heating chamber. The previously dark, glossy outside of the crucibles

became lighter and less reflective, as seen in Figure 8.2. The top surfaces of the used crucibles appeared etched compared to the smooth surface of the unused crucibles as shown in Figure 8.3. The crucible heated empty (HTe) was used to verify that the change was not due to chamber contamination or oxidation, and this resulted in a crucible that appeared like those in the as-received condition. The change in surface roughness was only seen to occur in the presence of molten iron. Iron was visible by BSE on most surfaces, including the top edge.

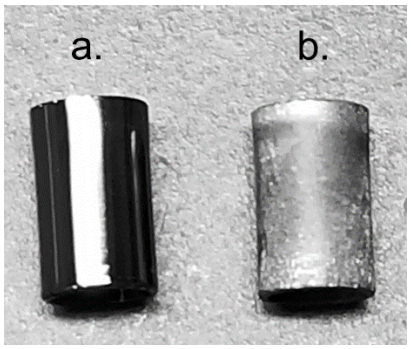

Figure 8.2. (a) Unused crucible next to (b) crucible heated with molten Fe-C_{sat} (crucible diameter = 5 mm)

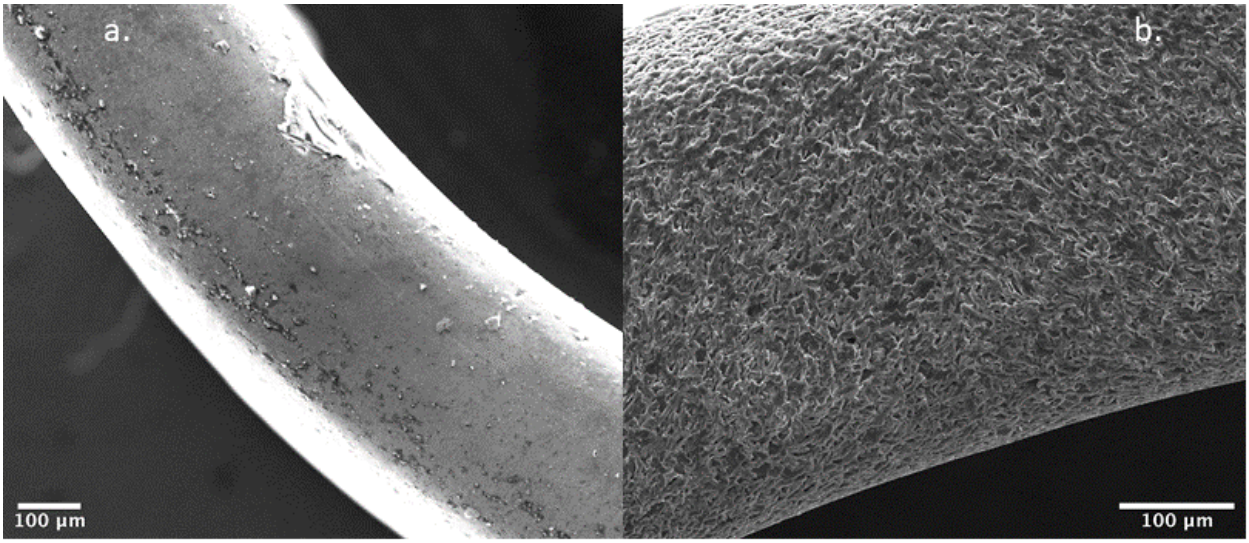

Figure 8.3. Secondary electron images of the top surfaces of glassy carbon crucibles: unused (a.) and heated with Fe-C_{sat} (b.)

Sample HTc (spherical iron-carbon droplet due to pre-melting) was placed on the crucible bottom without contacting the walls. During heating, penetration of the metal into the crucible was evident, as the focal point of the microscope had to be continually lowered to keep the sample surface - mostly covered by graphite flakes - in focus. The other iron samples, HT and LT, touched the crucible walls before heating, and were absorbed into the walls. The capillary force was strong enough to suspend the metal

above the bottom of the crucible, as shown in Figure 8.4. Mapping by EDS revealed that iron had permeated the walls of the crucible despite the droplet being graphite-saturated. In contrast with the iron-permeated structure after the experiments, before exposure to iron the glassy-carbon crucibles were free of porosity, appearing quite featureless in scanning electron micrographs.

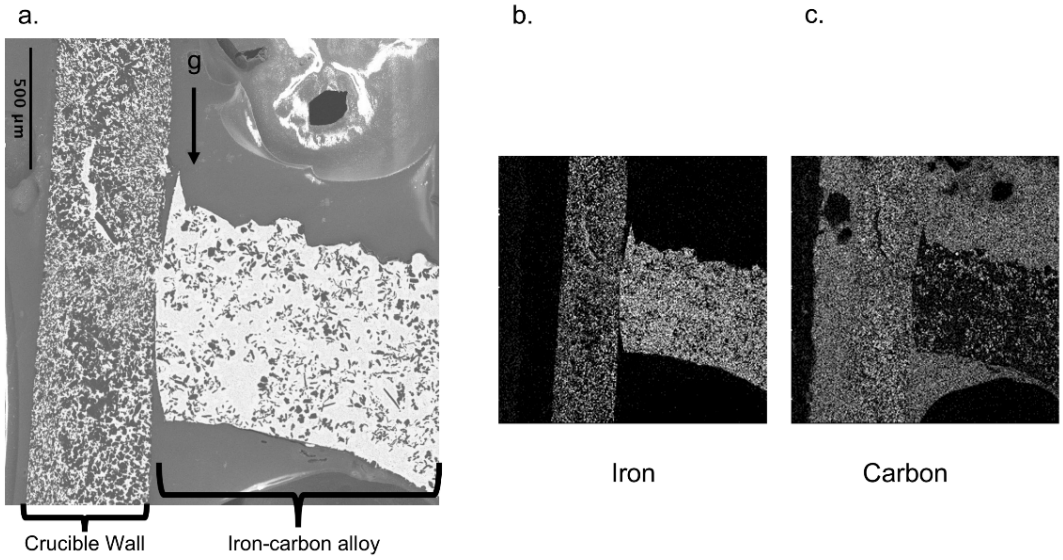

Figure 8.4. Fe-C_{sat} permeating the glassy carbon wall (sample HT). The direction of gravity (g) is shown by the arrow. (a) BSE image, with EDS maps of (b) iron and (c) carbon.

The XRD results shown in Figure 8.5 support a transformation of glassy carbon to graphite. The as-received crucible shows a similar diffraction pattern to the one heated without metal (HTe), whereas those which contained molten iron show sharp peaks around 26° 2θ and 45° 2θ, characteristic of graphite [12]. Carbonaceous materials are often characterized by average crystallite size (L_c) determined by the Scherrer equation in Eq. 1, in which λ is the wavelength of the X-ray source, β is the full width at half maximum of the 002 peak (radians), and θ is the angular location of the 002 peak [13]. Based on this equation, the average crystallite size of the as-received crucible was 15.4 Å whereas sample HT had an average crystallite size of 542 Å – confirming a large structural change during melting.

$$L_c = 0.89\lambda \div \beta cos\theta \qquad \text{Eq. 1}$$

Raman spectroscopy, seen in Figure 8.6, similarly showed that the as-received glassy carbon exhibited broader peaks compared to the crucibles that contained molten iron. The D band at 1360 cm^{-1}, characteristic of edge effects in crystallites [14], is more prominent in the as-received sample, which is expected due to the small crystallite size.

Position 2 (nearer the top edge of HTc) exhibited peaks between 0-750 cm^{-1}, characteristic of single-walled carbon nanotubes [15].

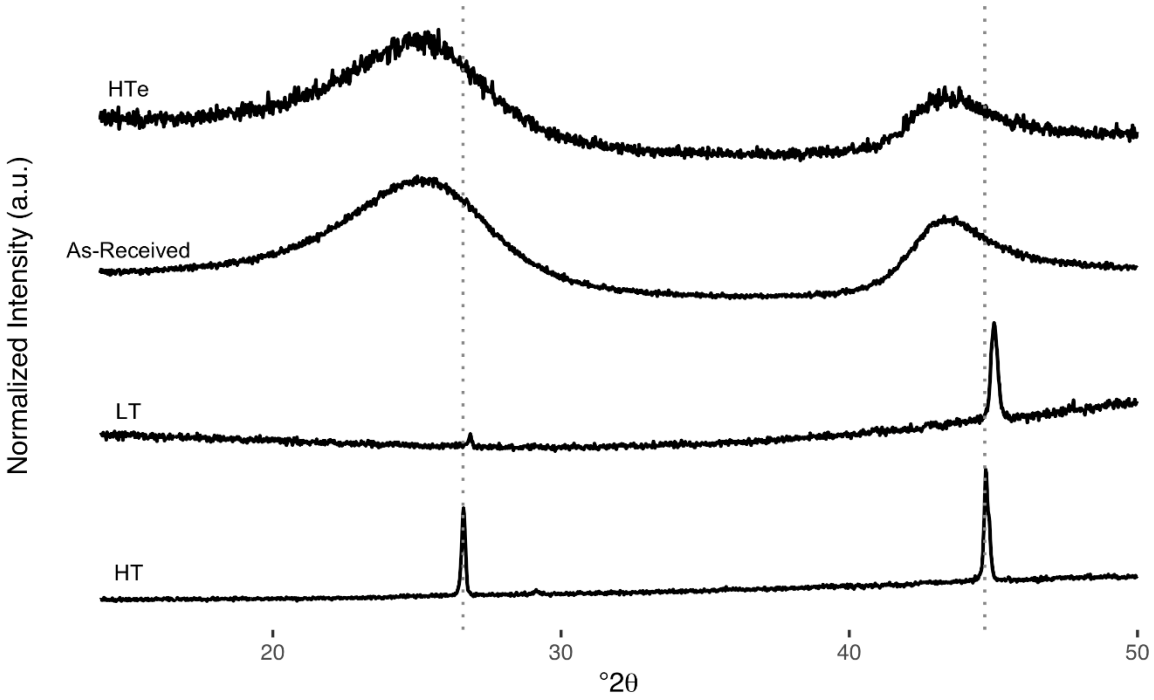

Figure 8.5. XRD results of the glassy carbon crucibles. Graphite peak locations (vertical lines) taken from [12].

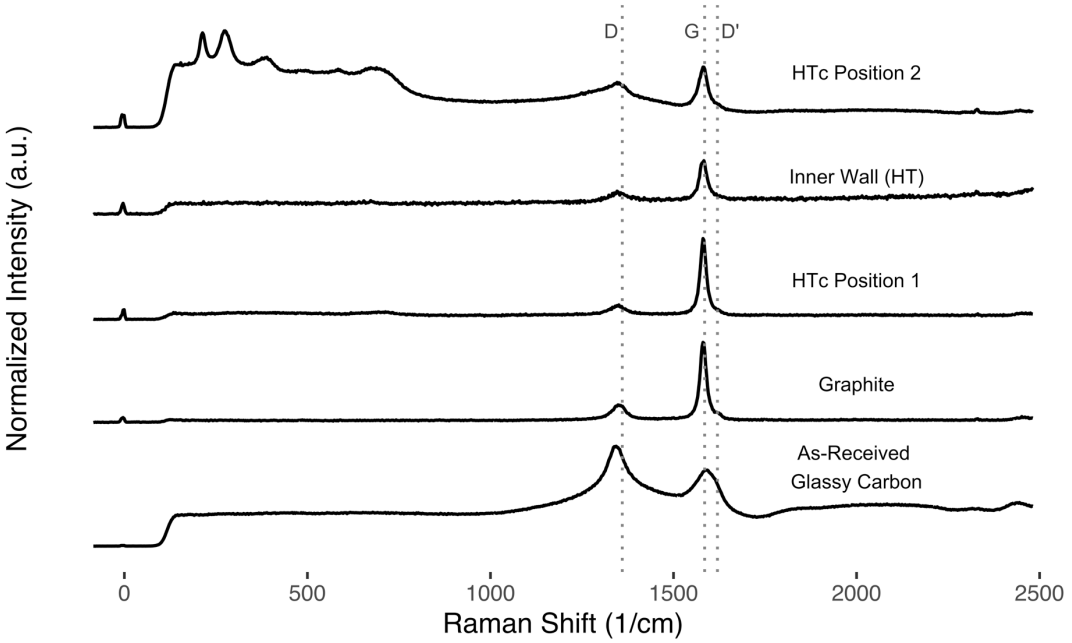

Figure 8.6. Raman results of the glassy carbon crucibles and a graphite crucible. Graphite band locations (vertical lines) taken from [14].

Penetration of iron into the crucible (Figure 8.4) was similar to the "reaction zone" shown by Weisweiler et al. [11]. This reaction zone consisted of small carbon particles within a metal matrix. This microstructure may be similar to embrittled zone seen in BF hearth walls [16], though the microstructure here has been penetrated to a greater extent, and crystallites are a smaller size. Two factors appear to contribute to penetration of the transformed carbon: reactive wetting of the carbon by the metal, and porosity created by graphitization. The porosity forms in the initially void-free glassy carbon because of the large density increase of carbon upon graphitization and can be estimated by Eq. 2. The density of glassy carbon (ρ_{glassy}) is 1.42 g/cm^3 (as listed by the manufacturer) and that of graphite ($\rho_{graphite}$) is 2.27 g/cm^3 [17], resulting in a predicted porosity of 35% for complete transformation. If the transformation is complete, and metal filled all pores, the area fraction of metal observed on a cross-section of the crucible wall would be equal to the porosity. The BSE image in Figure 8.7 has an area fraction of 37% iron, in line with the prediction. Formation of porosity during graphitization, which was not mentioned in previous studies, likely allows pathways for iron penetration, and so allows the reaction to propagate.

$$\text{Porosity} = 1-\rho_{glassy}/\rho_{graphite} \qquad \text{Eq. 2}$$

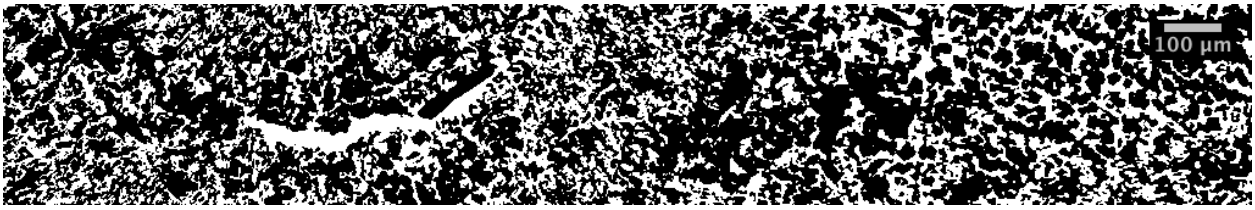

Figure 8.7. Back-scattered electron image of a cross-section of the crucible wall, used for porosity calculation. This image was taken from the micrograph in Figure 8.4a.

8.6 Comparison to Coke Analogs

Coke, the material used both as a fuel and a reductant within the blast furnace, has also been seen to be catalytically graphitized within the BF [18–22]. When looking at either Raman spectra or XRD data presented in the literature [18–20], this graphitization appeared to be both slower and less extensive compared to the above results with glassy carbon. While the ash content does slow this process, even cokes without ash have not exhibited the same drastic penetration and transformation that was seen with the glassy carbon [23].

Coke analogs have already been discussed in Ch. 7 as a way to produce controllable, homogenous coke-like materials for laboratory studies. These analogs perform similar to industrial cokes in reactivity tests and dissolution tests [24–26]. However, Longbottom et al. has observed the presence of glassy carbon within some coke analogs [24]. It is worth repeating the above experiments using a coke analog to see if there is preferential penetration along the glassy carbon regions of the analog.

Coke analogs were prepared according to the procedure detailed by Longbottom et al. [24]. The only deviations were the use of propylene glycol methyl ether (rather than propylene glycol), and the solid mixture was not ball milled. Details of the precursor materials can be found in Ch. 7. Samples were pressed into cylinders 17 mm tall with 11 mm diameter under 15 kPa for 10 minutes. Samples were then fired according to Reid et al. [26]. From these, samples of roughly 3.5 mm x 3.5 mm x 2.5 mm were cut to fit within an alumina crucible with 6.6 mm ID and 8 mm OD and 4.5 mm height.

Propylene glycol methyl ether was expected to pyrolyze similarly to propylene glycol, despite having an extra alkane group and one less alcohol group per molecule. Pyrolysis reactions are complex, but the small difference between resins was not expected to significantly change the bonding. Figure 8.8 show the measured characteristic ratios of the analogs and glassy carbon compared to literature values for coke analogs and metallurgical cokes [32]. Ch. 7.4.3 includes a more detailed discussion. Some regions give spectra similar to those of glassy carbon, supporting the presence of glassy carbon within these analogs.

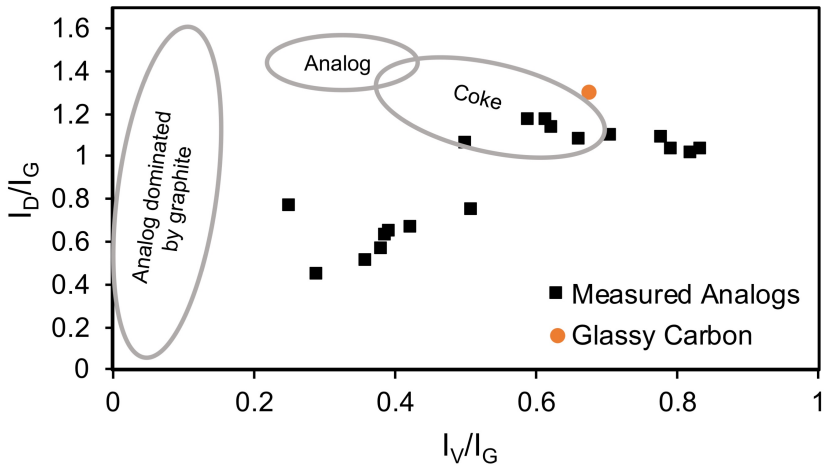

Figure 8.8. Characteristic ratios of Raman spectra of the present coke analogs and glassy carbon compared with coke analogs in literature, and metallurgical coke. The literature data are presented as ranges denoted by the circled regions [32].

The substrate of coke analog was placed within the alumina crucible. Fe-C_{sat}, prepared as documented above and having similar weight (0.15 g), was placed on top of the analog. This sample was then placed within the CSLM and heated according to the profile "HT" above. p_{O_2} was recorded as less than 10^{-21} atm at the beginning of heating. The results of two samples are shown in Figure 8.9. Compared to those heated in glassy carbon, the metal showed little interaction with the analog, and the coke analogs appeared visually similar before and after melting Fe-C. This is in contrast to the visual differences between heated glassy carbon crucibles in Figure 8.2. The micrographs of two analogs heated with Fe-C are shown in Figure 8.10. Neither sample showed much penetration with the analog, and both had a high angle of wetting. In Figure 8.10c, the Fe-analog interface can be seen more clearly. The analog was not homogenous: there were large pores (filled by epoxy during the mounting procedure), regions of small particles, and regions of larger particles. Despite the presence of these different features, the liquid iron did not seem to preferentially penetrate the analog, even the pores.

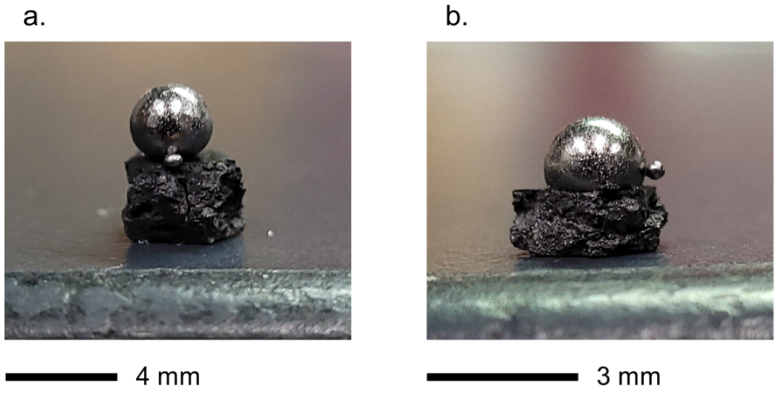

Figure 8.9. Macroscopic view of two Fe-C_{sat} samples (a./b.) heated in contact with coke analogs.

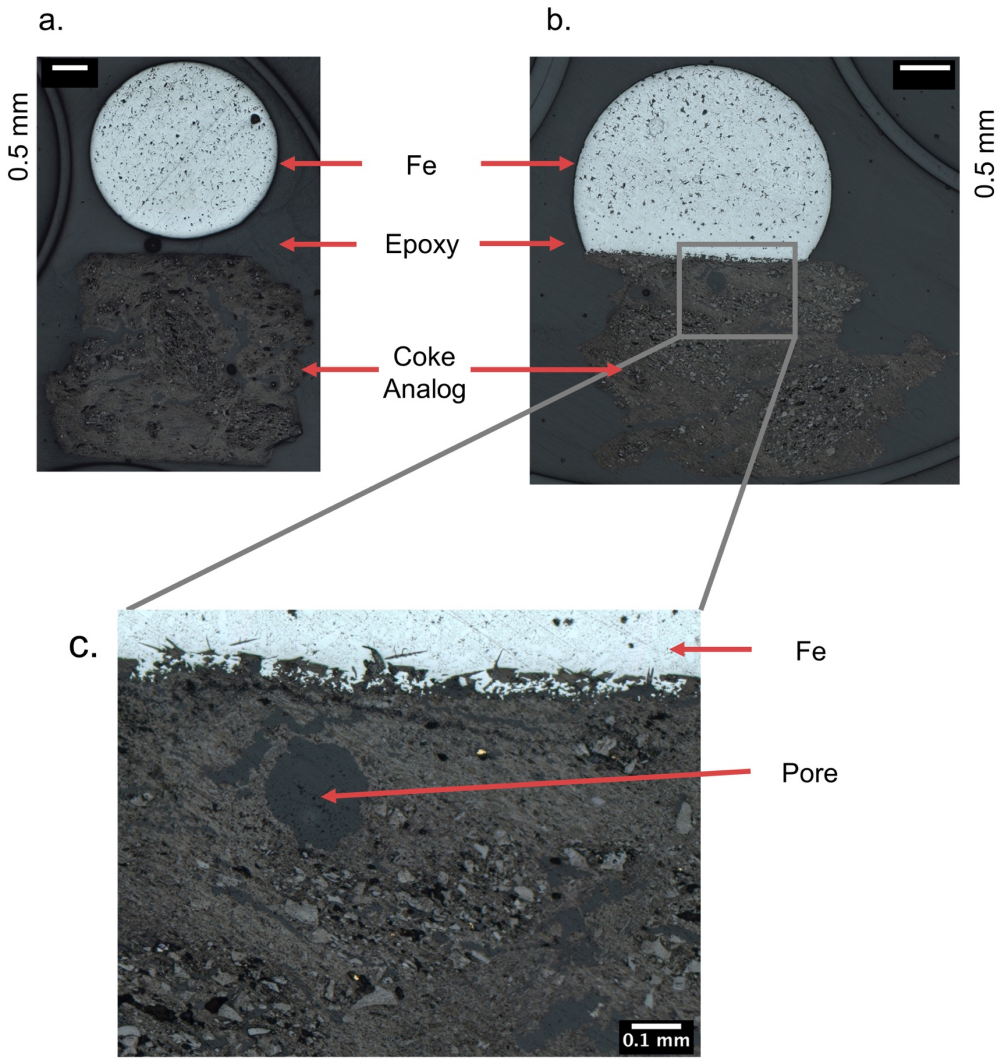

Figure 8.10. Optical microscopic images of two Fe-C_{sat} samples heated in contact with coke analogs (a./b.). A higher magnification section is shown in c.

The catalyzed graphitization of coke in the BF is well-established by literature. However, when the reaction of a coke analog is compared to that of glassy carbon, the interactions were quite different in rate. For a high-temperature exposure of relatively short duration, the reactive wetting and extensive penetration by liquid Fe-C of the glassy carbon crucible was not seen with the coke analog substrate. Rather, the interaction between liquid Fe-C and the analog was more similar to the non-wetting behavior of liquid interaction with graphite (Ch. 10), as informed by the high angle of wetting between the liquid and the analog [27]. However, this phenomenon is not just with Fe-C and a coke analog: the non-wetting and lack of penetration observed with the analog was also similar the interaction of Fe-C with a low impurity, pressed coke substrate from Sun et al. [23].

Catalytic graphitization occurs when liquid Fe dissolves carbon (of higher free energy than graphite) and, when supersaturated with respect to graphite, reprecipitates the excess carbon as graphite [11]. An important kinetic limitation to this process is the speed of dissolution. Coke dissolves more slowly than graphite and glassy carbon, even in the absence of ash [3,23,28]. Because the dissolution of coke is slower, the graphitization kinetics of coke (and coke analogs) are also slower. Chang et al. compared coke taken from the cohesive zone of a quenched BF to the feed coke and saw only a slight degree of graphitization of the used coke compared with the feed coke [20]. Guo et al. compared coke taken at multiple vertical positions within the deadman; they saw an increase in crystallite size from 2.3 nm to as high as 83 nm [19]. The temperature of the coke would be dependent on vertical position within the BF, with higher temperature regions resulting in larger crystallite sizes. Yet, despite the long time in contact with HM, the crystallite size growth of cokes within the BF was less than was seen in the glassy carbon (an increase to 542 nm in 10 minutes). The reaction of liquid Fe-C with a coke analog did not occur with the speed nor extent that it did with glassy carbon, and it can be presumed that the slow dissolution of coke (in addition to interfacial ash limitations) is partly to blame.

While the behavior of coke in blast furnace is relatively clear, the interactions of the coke analog in these laboratory experiments were less clear. As the analog had regions of glassy carbon, it was predicted that the HM would preferentially penetrate into the glassy carbon, but that did not occur. One explanation is the difference in precursor materials. Glassy carbon is formed by pyrolyzing organic compounds. For the analog, the glassy carbon should stem from pyrolysis of the phenolic resin. Literature reports glassy carbons can be produced by pyrolyzing either furfuryl alcohol, polyvinylidene chloride, or a phenol-formaldehyde resin [8,29–31]. The manufacturer does not specify the precursor used but does specify a heat-treating temperature of over 2000 °C. The precursor of the glassy-carbon crucibles may be different from that of the coke analog, and coke itself: Aladejebi recorded Raman spectra for both coke analogs and industrial cokes [32]. The results were reported with two characteristic ratios. The first was the intensity ratio of the D and G peaks. The second was the minimum intensity between the D and G peaks compared to that of the G peak. While the former was in-line with both coke and coke analogs, the later had a higher ratio, which could denote differences causing the different interactions. Neutron diffraction techniques and transmission electron microscopy can be more effective in distinguishing variations between glassy carbons [33], but the techniques were not able to be pursued in the present work. Why the glassy carbon within the analog is not preferentially penetrated remains an unanswered question.

8.7 Conclusions

Catalytic graphitization did occur when graphite-saturated liquid iron contacted glassy carbon. Because of the higher activity of carbon in glassy carbon than in graphite [34], carbon solubility is higher in the metal in contact with glassy carbon: even though the metal is graphite saturated, it is undersaturated with respect to glassy carbon. This means that glassy carbon can dissolve into liquid iron that has been saturated in contact with graphite. Dissolution of glassy carbon into graphite saturated iron, results in the precipitation of graphite. The net effect is transformation of glassy carbon to the stable phase, graphite. This mechanism has been established in previous work [10,11]. Similar to the previous work, transformation of the glassy carbon to graphite occurs within minutes [10]. The cost, low fracture toughness and low thermal conductivity of glassy carbon limits its practical use as a furnace lining; in addition, rapid transformation of glassy carbon would preclude its use as a blast furnace refractory.

Coke analogs did not react with Fe-C_{sat} to the same extent that glassy carbon did under the experimental conditions. In theory, the graphitization of coke could reflect that of glassy carbon, given enough time. However, the dissolution of coke is limited by sp^3 bonding, and, because graphitization relies on dissolution, the process of graphitizing cokes is much slower.

8.8 Hypotheses Revisited

Liquid Fe-C_{sat} will not react with or wet glassy carbon. The angle of contact of the metal with the glassy carbon should be greater than 90°.

This was unsupported. Liquid Fe-C_{sat} reactively wetted glassy carbon reactively as the liquid catalyzed a phase transformation of glassy carbon to the lower energy graphite.

8.9 References

[1] A. Dzermejko: *Iron Steel Technol.*, 2014, vol. 11, pp. 41–56.
[2] A. Dzermejko: in *Refractories Handbook*, C. Schacht, ed., Marcel Dekker, New York, 2004, pp. 201–14.
[3] D. Jang, Y. Kim, M. Shin, and J. Lee: *Metall. Mater. Trans. B*, 2012, vol. 43B, pp. 1308–14.
[4] C. Wu and V. Sahajwalla: *Metall. Mater. Trans. B*, 2000, vol. 31B, pp. 215–6.
[5] C. Wu and V. Sahajwalla: *Metall. Mater. Trans. B*, 2000, vol. 31B, pp. 243–51.
[6] H. Gudenau, J. Mulanza, and D. Sharma: *Steel Res.*, 1990, vol. 61, pp. 97–104.
[7] J. Robertson: *Adv. Phys.*, 1986, vol. 35, pp. 317–74.
[8] P. Harris and S. Tsang: *Philos. Mag. A*, 1997, vol. 76, pp. 667–77.

[9] K. Jurkiewicz, S. Duber, H.E. Fischer, and A. Burian: *J. Appl. Crystallogr.*, 2017, vol. 50, pp. 36–48.
[10] W. Weisweiler and V. Mahadevan: *High Temp. High Press.*, 1971, vol. 3, pp. 111–9.
[11] W. Weisweiler, N. Subramanian, and B. Terwiesch: *Carbon N. Y.*, 1971, vol. 9, pp. 755–61.
[12] J. Lukesh and L. Pauling: *Am. Mineral.*, 1950, vol. 35, p. 125.
[13] ASTM D5187-10, *Standard Test Method for Determination of Crystallite Size (L_c) of Calcined Petroleum Coke by X-Ray Diffraction*, 2015.
[14] S. Sze, N. Siddique, J. Sloan, and R. Escribano: *Atmos. Environ.*, 2001, vol. 35, pp. 561–8.
[15] K. Jurkiewicz, M. Pawlyta, D. Zygadło, D. Chrobak, S. Duber, R. Wrzalik, A. Ratuszna, and A. Burian: *J. Mater. Sci.*, 2018, vol. 53, pp. 3509–23.
[16] Y. Deng, J. liang Zhang, and K. xin Jiao: *ISIJ Int.*, 2018, vol. 58, pp. 1198–203.
[17] J. Shackelford, Y. Han, S. Kim, and S. Kwon: *CRC Materials Science and Engineering Handbook*, 4th edn., CRC Press, 2016.
[18] W. Wang, K.M. Thomas, R.M. Poultney, and R.R. Willmers: *Carbon N. Y.*, 1995, vol. 33, pp. 1525–35.
[19] Z. Guo, K. Jiao, J. Zhang, H. Ma, S. Meng, Z. Wang, J. Zhang, and Y. Zong: *ACS Omega*, 2021, vol. 6, pp. 25430–9.
[20] Z.Y. Chang, K. Jiao, and J. Zhang: *Metall. Mater. Trans. B*, 2018, vol. 49, pp. 2956–62.
[21] S.S. Gornostayev and J.J. Härkki: *Carbon N. Y.*, 2007, vol. 45, pp. 1145–51.
[22] Y. Li, T. Jian, T. Ma, M. Hu, L. Gao, and Y. Yang: *Metall. Res. Technol.*, 2020, vol. 117, p. 409.
[23] M. Sun, J. Zhang, K. Li, H. Li, Z. Wang, C. Jiang, S. Ren, L. Wang, and H. Zhang: *JOM*, 2020, vol. 72, pp. 2174–83.
[24] R.J. Longbottom, B.J. Monaghan, M.W. Chapman, S.A. Nightingale, J.G. Mathieson, and R.J. Nightingale: *Steel Res. Int.*, 2011, vol. 82, pp. 505–11.
[25] M. Chapman, R. Nightingale, and B. Monaghan: *CHEMECA 2011 Australas. Conf. Chem. Eng.*, 2011, pp. 1–14.
[26] M.H. Reid, M.R. Mahoney, and B.J. Monaghan: *ISIJ Int.*, 2014, vol. 54, pp. 628–33.
[27] S.T. Britt and P.C. Pistorius: *Steel Res. Int.*, 2022, vol. 93, p. 2100068.
[28] X. Xing, S. Jahanshahi, J. Yang, and O. Ostrovski: *Arch. Mater. Sci. Eng.*, 2018, vol. 92, pp. 22–7.
[29] C. Moreno-Castilla, O.P. Mahajan, P.L. Walker, H.J. Jung, and M.A. Vannice: *Carbon N. Y.*, 1980, vol. 18, pp. 271–6.
[30] A. Oya, R. Yamashita, and S. Otani: *Fuel*, 1979, vol. 58, pp. 495–500.
[31] R. Kammereck, M. Nakamizo, and P.L. Walker: *Carbon N. Y.*, 1974, vol. 12, pp. 281–9.
[32] O.A. Aladejebi: *Effect of Minerals on Coke Analogue Carbon Bonding and Reactivity*, University of Wollongong, 2017.
[33] T.B. Shiell, S. Wong, W. Yang, C.A. Tanner, B. Haberl, R.G. Elliman, D.R. McKenzie, D.G. McCulloch, and J.E. Bradby: *J. Non. Cryst. Solids*, 2019, vol. 522, p. 119561.
[34] B. Terry and X. Yu: *Ironmak. Steelmak.*, 1991, vol. 18, pp. 27–32.

9 Precipitation of TiC in molten Fe-C_{sat} observed with the CSLM

9.1 Abstract

The thermodynamics of the Fe-C-Ti system are reviewed from literature and compared to experiments performed with the high temperature confocal scanning laser microscope (CSLM). The present method observed TiC particles at temperatures higher and [Ti] lower than previous results. The method was found to be inconsistent, giving confidence intervals of above 100 °C. Coupled with the work showing the uncertainty of the temperature of the metal sample, it is proposed that the current procedure was unable to produce quantitative results, but some qualitative trends were observed. TiC particles were observed at temperatures above those predicted previously, and the cooling rate was found to affect the observation temperature, with observations shifted 100 °C cooler when higher cooling rates were used.

9.2 Within the Narrative

With the proposed mechanism that Ti(C,N) catalyzes skull formation for hearth wear reduction, knowledge of the stability of Ti(C,N) and its components TiN and TiC are vital. TiN has been investigated thoroughly, but few studies document the formation of TiC in Fe-C_{sat}. This work attempted to extend the observations of TiC with the CSLM, providing further data on the stability of TiC in liquid Fe-C_{sat}. This is particularly important when deciding what Ti compound to add to hearth refractory.

The experiments of this chapter were performed using similar methods to those of Ch. 5. These experiments use the same precursor materials, and the preparation instructions are repeated in this chapter, along with the other relevant methods.

9.3 Introduction[1]

The charging of titanium bearing ore in blast furnaces has long been known to prevent blast furnace (BF) hearth wear and to extend the campaign life of the blast furnace (BF) [1–3]. Despite Ti additions being "operationally effective" in protecting the furnace, much is still unknown about the exact mechanism of prevention. Furnace operators have guidelines for how much to charge (15-20 lb/ NTHM [7.5-10 kg/tonne

[1] This section is a concise version of the more detailed discussion in the literature survey.

HM] for remedial cases) [4]. The desired [Ti] in hot metal (HM) is between 0.07% wt and 0.15% wt Ti [5]. The bottom limit follows the observation of TiC particles by Li et al. [6]. Ironmakers have set the higher limit based on observed issues downstream including nozzle clogging and viscosity issues [5]. While the results are well correlated to the industrial practice, more work is needed to study TiC particles, that is, in absence of N_2.

As protection of the hearth refractory likely stems from the presence of Ti(C,N) particles, understanding the thermodynamics of Ti(C,N) and the constituent compounds (TiC and TiN) in HM is important. This chapter probes the thermodynamics of TiC in Fe-C_{sat}. Ti(C,N) is the most stable species within the blast furnace [6], but a starting point is the study of TiC. TiC was chosen due to reported solubilities being dependent on experimental method. Figure 9.1 shows three results of TiC stability from the literature. Li et al. observed particles using the CSLM [6]. Sumito et al. and Yuehua & Xinsheng performed sampling experiments [7,8]. The CSLM results found TiC to form at temperatures approximately 50 °C higher than in the sampling experiments. It is important to understand this disagreement to establish the minimum [Ti] needed for TiC stability in HM.

There is additional reason to investigate the stability of TiC. TiC was the compound Nippon Steel chose to add to hearth refractory to provide additional protection against wear [9]. If the protection of refractory required TiC stability, the TiC should be investigated. However, the protective effects could come from Ti being localized at the hot face when wear occurs. Here, TiC may dissolve into the more stable Ti(C,N) phase. Nevertheless, both hypotheticals benefit from knowing the solubility.

The TiC equilibrium experiments from Li et al. [6] are revisited here to add to the compositions observed, and to investigate the differences between results with the CSLM and the sampling results by Sumito et al. and Yuehua & Xinsheng [7,8].

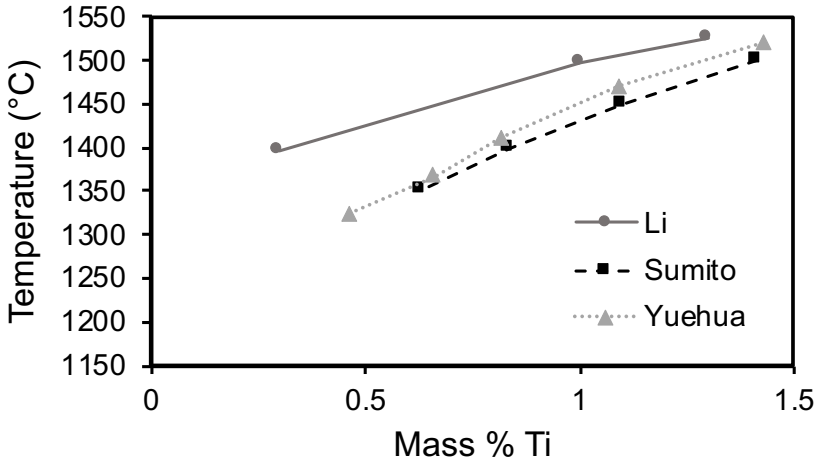

Figure 9.1. Comparison of TiC equilibrium literature [6–8], showing the reported TiC precipitation temperature in graphite-saturated iron.

9.4 Experimental *In-situ* Methods

Fe-C_{sat} was prepared by melting electrolytic iron in a graphite crucible with an induction furnace and sampling after 5 minutes at 1550 °C. This was enough to ensure saturation [10]. A binary Fe-Ti alloy was prepared by adding electrolytic iron and 4% wt titanium sponge to an alumina crucible and melting in an induction furnace. The furnace was stopped soon after melting due to an air leak into the furnace. To account for the possible loss of [Ti] from oxidation, the composition was determined as 3.6% wt Ti by energy dispersive spectroscopy on a polished section. Sections of Fe-C_{sat} and the binary alloy were weighed to have a sample mass of 0.11 g. The metal precursors were added to MgO crucibles (70 µL), and the crucibles were placed on the CSLM B-type thermocouple holder. The initial heating followed the nominal parameters from Table 9.1. After 5 minutes at 1550 °C, the temperature was decreased at a rate of 5 °C/ min. The temperature measurement in the CSLM furnace was calibrated with pure Cu (melting point 1085°C) and pure Fe (melting point 1538 °C) in MgO crucibles, giving apparent melting points of 1137°C and 1553°C respectively. Samples were heated in argon with p_{O_2} monitored and less than 10^{-18} atm. Multiple samples of the same composition and heats were used to obtain the presented date.

The CSLM used a 20× objective lens for a compromise between magnification and field of view. Images were recorded at 10 frames per second with a resolution of 4.6 pixel/µm with a window of 204 × 157 µm. The intensity method described in Ch. 11 was used to obtain focus when the molten surface was clear. The precipitation temperature denoted the temperature at which the first particle was seen. Cooling was continued unimpeded to record the temperature at which the next particle was seen.

Table 9.1. Nominal Experimental Heating Parameters

Temperature (°C)	Rate (°C/min)	Holding Time (sec)
300	50	60
1350	400	0
1550	100	300
1225	-5	0
	Heat off	

9.5 Results & Discussion

The precipitation temperatures of the particles are shown in Table 9.2 and plotted with 95% confidence interval against literature values in Figure 9.2. Multiple observations of the same samples did not give consistent results, evidenced by the wide confidence intervals. For the sample containing 0.39% Ti, the first particle was seen in one melt at 1407 °C but at 1320 °C in a different melt. For the sample containing 0.90% Ti, particles appeared during the hold at 1549 °C, indicating not enough superheat was available to dissolve all TiC particles; that is, TiC was stable at 1550 °C in liquid Fe-C_{sat} with 0.90% Ti.

The appearance of the first TiC particle varied greatly and was not able to be linked to a single temperature. The wide confidence interval of the sample with 0.39% Ti points to this, but further evidence can be seen in Table 9.3, which records the temperatures at which any particle was observed during a single heat. For 0.49% Ti, the first particle was observed at 1408 °C and soon disappeared; the next particle was not seen until 1384 °C before disappearing, and a third was not seen until 1360 °C. An image representative of the first observation is shown in Figure 9.3. The problem of repeatability is not the only issue of these experiments; these experiments should also suffer the difficulties of knowing the temperature offset between the thermocouple and the metal sample, discussed later in Ch 11.

Table 9.2. Equilibrium Experiment Results

Ti (%wt)	Temperature (°C) at which particles were observed
0.39	1337, 1320,1407
0.49	1408
0.90	1460 @ 1470 hold, 1507 @ 1523 hold, 1549 @ 1549 hold

*Commas denote separate runs

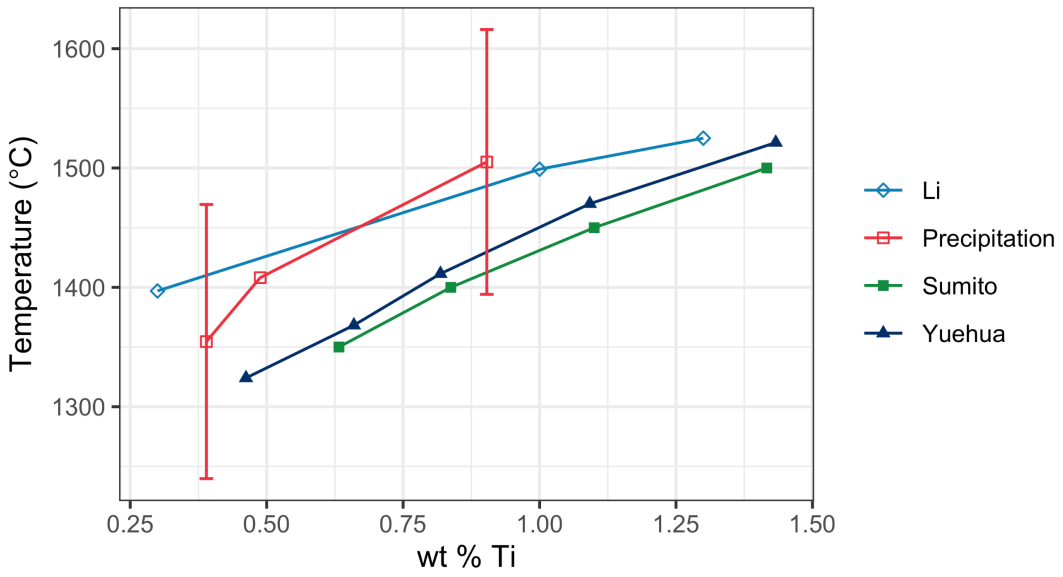

Figure 9.2. Comparison of precipitation temperatures to literature TiC solubility literature [6–8]. Error bars represent 95% confidence intervals.

Table 9.3. Temperature of Particles Seen on a Single Run

Ti (%wt)	Temperature (°C) at which Particles were Observed
0.39	1337, 1312
0.49	1408, 1384, 1360

Figure 9.3. Typical observation from equilibrium experiment.

One additional importance to this experiment was the cooling rate used. Table 9.4 shows the particle observation results when cooling was controlled manually by a hold

function. The cooling rate when manually controlling was between 30-40 °C/min. Particles were observed around 100 °C lower than the slow cooled method. Presumably, the faster cooling rate did not allow the particles enough time to nucleate and grow enough for optical detection.

Table 9.4. Results of Equilibrium Experiments using faster (30-40 °C/min) cooling rate

Ti (%wt)	Precipitation Temperature (°C)
0.30	1172, 1183, 1211, 1235
0.39	1233, 1244, 1250, 1250
0.49	1272, 1278, 1278
0.90	1446, 1455, 1468

The issues with repeatability means this work should not be used as quantitative results. However, there are some trends that could be used as qualitative results. Using this method, particles were seen at higher temperatures than previously observed by either CSLM or sampling. A small fraction of particles could be stable at temperatures higher than what the sampling method is able to detect.

The disconnect between sampling methods and CSLM methods remain. Rather than confirming one of the methods, these results exaggerate the disconnect. As observed in this study, a small fraction of particles could be stable at temperatures higher than what the sampling method is able to detect. The repeatability problem of these experiments should not be ignored. Particle appearance seemed to be stochastic, possibly following a distribution based on the superheat used and the time to form particles.

9.6 Conclusions

- *In-situ* observations of TiC on liquid Fe-C were performed. Observations had high variance, but average precipitation temperatures were similar to that previously by CSLM. However, there remains a disconnect between temperatures of stability observed this way as compared to traditional sampling methods, with the CSLM able to observe particles at temperatures higher than expected by sampling methods.
- Precipitation experiments with lower cooling rates saw particles visible at 100 °C above those seen in the more rapidly cooled experiments.

9.7 References

[1] J. Huo and J. Huang: *Ironmak. (In Chinese)*, 2013, vol. 32, pp. 14–6.
[2] K. Narita, M. Maekawa, T. Onoye, Y. Satoh, and M. Miyamoto: *Trans. Iron Steel Inst. Jpn.*, 1977, vol. 17, pp. 459–68.
[3] S. Street, C. Copeland, and E. Worral: in *AISTech Proceedings*, 2013, pp. 381–403.
[4] S. Street, A. Cheng, and I. Cameron: in *AISTech Proceedings*, 2019, pp. 275–88.
[5] Y. Zhao, L. Lherbier, D. Fu, Y. Chen, C. Zhou, and J. Grindey: in *AISTech Proceedings*, 2012, pp. 457–69.
[6] Y. Li, Y. Li, and R.J. Fruehan: *ISIJ Int.*, 2001, vol. 41, pp. 1417–22.
[7] M. Sumito, N. Tsuchiya, K. Okabe, and K. Sanbongi: *Trans. Iron Steel Inst. Japan*, 1981, vol. 21, pp. 414–21.
[8] D. Yuehua and L. Xinsheng: *Iron Steel Vanadium Titan. (In Chinese)*.
[9] H. Inoue, M. Nitta, T. Matsui, T. Wakasa, Y. Yamagami, and T. Mochida: *United States Pat.*
[10] T. Britt and P.C. Pistorius: *Metall. Mater. Trans. B*, 2021, vol. 52, pp. 1–5.

10 Flux-mediated Wetting of Alumina by Liquid Fe-Ti-C_{sat}

This chapter modified from its original form in the journal *Steel Research International*:

S. T. Britt and P. C. Pistorius, "Flux-Mediated Wetting of Alumina by Liquid Fe–Ti–C_{sat}," *Steel Res. Int.*, p. 2100068, Jun. 2022. DOI: 10.1002/srin.202100068.

10.1 Abstract

Metals do not wet oxides as a general rule. Exceptions to this occur in the presence of dissolved species or chemical reactions. Fe-C_{sat}-Ti was seen to wet alumina crucibles but not crucibles of graphite or MgO. This was determined to be macroscopically due to reactive wetting of the ternary alloy with Al_2O_3; microscopically, the reaction formed a nano-scale layer of TiC on Al_2O_3, with the hot metal wetting the TiC substrate. Molten fluxes offered a way to mitigate the wetting of the alumina crucible by preventing the reaction. The liquid Al_2O_3-CaF_2 flux wetted the Al_2O_3 crucible, coating both the crucible bottom walls and bottom. This was effective in preventing wetting despite alumina activity being unity in the initial components. The volatilization of fluorine resulted in a calcium aluminate coating on the original crucible. Using the molten flux was more effective than sintering CA particles onto the crucible bottom because the liquid flux coated the crucible walls. Though wetting is a problem in industry, this offers practical mitigation of wetting by utilizing a flux coating.

10.2 Within the Narrative

This chapter supports the work to view the formation of TiC on molten metal (Ch. 5, 9). In brief, viewing those particles would not have been possible without the work documented in this chapter. Additionally, the time spent considering the surface energy of TiC led to the hypothesis tested in Ch. 7, that the composition of Ti(C,N) and therefore the surface energy would dictate performance in skull formation.

10.3 Introduction

Much of ironmaking and steelmaking relies on interfacial reactions or interactions. In the blast furnace, the slow solid-solid interaction of coke and solid iron limits the carbon content within the metal to less than 1% wt [1]. Sulfur is removed from steel through contact with the ladle slag [2]. In the blast furnace, hot metal undersaturated in carbon contacts the carbonaceous hearth refractory contributing to hearth wear [3]. Reduction

of direct reduced iron is limited by the ability of the reducing gas to permeate the pellet [4]. Interfacial regions are particularly important at solid-liquid interfaces. These interactions are often denoted as wetting, with a contact angle smaller than 90°, or non-wetting with an angle of contact greater than 90°. This is related to the surface energies of the two substrates by Young's equation, shown below in Eq. 1. In Figure 10.1, The surface energy of the liquid is denoted as γ_{lv}, the surface energy of the solid substrate as γ_{sv}, the surface energy between the liquid and solid as γ_{sl}, and the equilibrium angle of contact as θ. This equation allows a relatively simple experiment to measure a liquid with unknown surface energy. One need only observe the angle of contact the liquid makes with the substrate and use Eq. 1 to determine the unknown liquid surface energy. The simplicity of this approach means it is easy to qualitatively determine if a liquid is wetting or non-wetting even on large scales such as in steel shops.

$$\gamma_{sv} = \gamma_{sl} + \gamma_{lv}\cos(\theta) \qquad \text{Eq. 1}$$

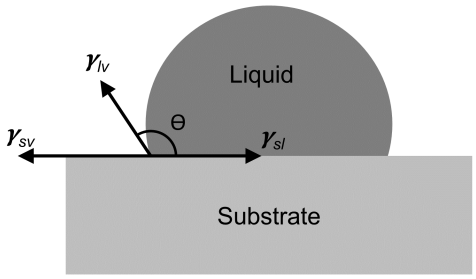

Figure 10.1. Schematic of Young's equation

Many of the solid-liquid interfaces within a steel shop are non-wetting. This is by design as the liquid must be continually transferred from one container to another. The general rule of wetting is "like wets like;" i.e., metal is likely to wet a metal substrate but not wet an oxide substrate [5]. An exception to this rule is when reactive wetting occurs [6], such as when pure molten iron contacts a graphite substrate. As documented by Wu et al., the molten iron initially did not wet the carbon substrate initially (θ greater than 90°), but within 10 seconds the angle decreased to above 60° then stabilized at 100° after 100 seconds [7]. When using pre-carburized iron (greater than 3.7 % wt), the reaction is not strong enough to cause wetting [8].

Wetting does not have to be transient to be characterized as reactive. The primary features are that it is enabled by chemical reaction and the time to reach the equilibrium contact angle is 10^1-10^4 s [6]. Dissolved species can also strongly affect the surface

tension. This is prevalent with sulfur and oxygen, the later requiring monitoring of furnace P_{O_2} when performing sessile drop experiments [9].

Metallic systems with dissolved Ti are beneficial to the ironmaking process, problematic in the steel industry, and of interest for fundamental wetting experiments. Clogging of the submerged entry nozzle is often an issue when steels are Ti bearing [10]. It is thought that TiN inclusions agglomerate within the nozzle, restricting the flow through. This is one of the hypothesized reasons why charging ilmenite (ferrotitanium ore) is effective in protecting the blast furnace hearth: the agglomeration of Ti(C,N) can restrict flow to the refractory hot face [11]. These species are also interesting from a fundamental standpoint. As pure TiC or TiN, rather than the solid solution Ti(C,N), both are non-wetting to Ag and Cu when stoichiometric. However, when TiC or TiN is more anion deficient, Ag and Cu begin to wet the non-stoichiometric substrate [12]. Additionally, metal-ceramic systems that are usually non-wetting can become wetting with as little as 1% at. Ti [5].

In seeking to expand the work of Li et al. observing TiC in molten Fe-C_{sat} [13], the Fe-C_{sat}-Ti system repeatedly wetted the alumina crucibles used to contain the metal. It has previously not been documented that a carbon saturated Fe-C-Ti alloy wets an Al_2O_3 substrate, nor have mitigation techniques been explored to prevent this wetting.

10.4 Experimental Methods

Fe-C_{sat} was prepared by heating electrolytic iron in a graphite crucible to 1550 °C with an induction furnace. The melt was sampled after 10 minutes, a long enough time to reach carbon saturation [14], and the sampled rod was sectioned to yield a sample mass of around 0.2 g for CSLM melting in Al_2O_3 and graphite crucibles or 0.065 g for MgO crucibles. The sectioned rod and Ti granules (around 1% wt; 0.5% wt for graphite crucibles) were placed in crucibles of Al_2O_3 (crucible capacity 137 µL), MgO (70 µL), and graphite (90 µL). The amount of dissolved Ti was enough to ensure TiC stability at some temperature range between the liquidus and the maximum temperature, but the thermodynamic predictions from Li et al. and Sumito et al. do not agree as to the temperature below which TiC would be stable [13,15]. To protect the platinum B-type thermocouple holder (TC), graphite and fluxed crucibles were not placed directly on the TC. Rather, graphite crucibles were placed within thick-walled (3 mm) alumina crucibles and fluxed crucibles were placed on platinum foil. These crucible-specific protections are shown in Figure 10.2.

For wetting tests – those to obtain the angle of contact – the crucibles containing Fe-C_{sat} and Ti were heated according to the profile shown in Figure 10.3 to a nominal 1560°C, holding for 15 minutes before quenching at a cooling rate of around 1000 °C/min. It should be noted that these are not equilibrium angles of contact: those have been extensively tabulated for many systems [5,16]. Rather this is an *ex-situ* method to compare the different metal-crucible interactions and to determine the effectiveness of the mitigation technique. Though the metal is contained in crucibles rather than flat substrates, this procedure is not dissimilar to the quenching method used by Nguyen et al. [17]. Upon cooling, samples were sectioned in half vertically, mounted in epoxy, and polished to measure the angle of contact between the metal and crucible. Representative measurements are shown in Figure 10.4. of the metal with graphite crucibles and MgO. ImageJ was used to manually measure the angles of contact. The angles were measured in a similar way to that in the literature [17,18]. Because the MgO crucibles were filled with metal, the angle measured was between the top surface of the metal and the crucible wall. Scanning electron microscope (SEM) images were obtained with an FEI Quanta 600 equipped with Oxford EDS detector.

Two coatings applied to Al_2O_3 crucibles were used to test a mitigation technique. For experiments using flux to coat crucible, Al_2O_3 and CaF_2 powders were mixed in a 28-72% wt ratio, and 0.008 g of the mixture was added to an Al_2O_3 crucible (6.8 mg/cm^2 of inner surface area). Calcium aluminate (equimolar CaO-Al_2O_3, referred to as CA) was also tested as a coating; the 0.0116 g of powder was a mixture of $CaAl_2O_4$ and other calcium aluminate phases [19]. Powders were added to the alumina crucibles, and the crucibles were half-filled with isopropyl alcohol to create a slurry, to evenly distribute particles upon stirring. Crucibles containing the slurry were heated to 1560 °C for 10 minutes according to the "coating" profile in Figure 10.3 which included a hold at 100 °C for 90 seconds to evaporate the alcohol. After cooling, metal was added to these coated crucibles which were then heated as above.

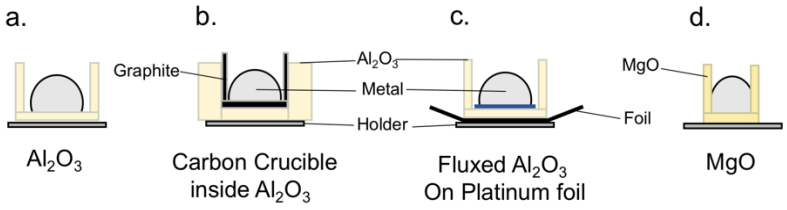

Figure 10.2. Sample holder protection schematics for crucibles of a.) Al_2O_3, b.) carbon crucibles, c.) coated Al_2O_3, and d.) MgO.

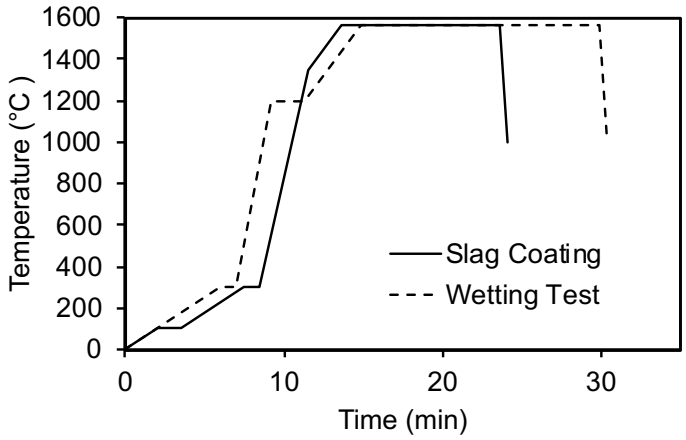

Figure 10.3. Heating profile for wetting experiments and slag coating.

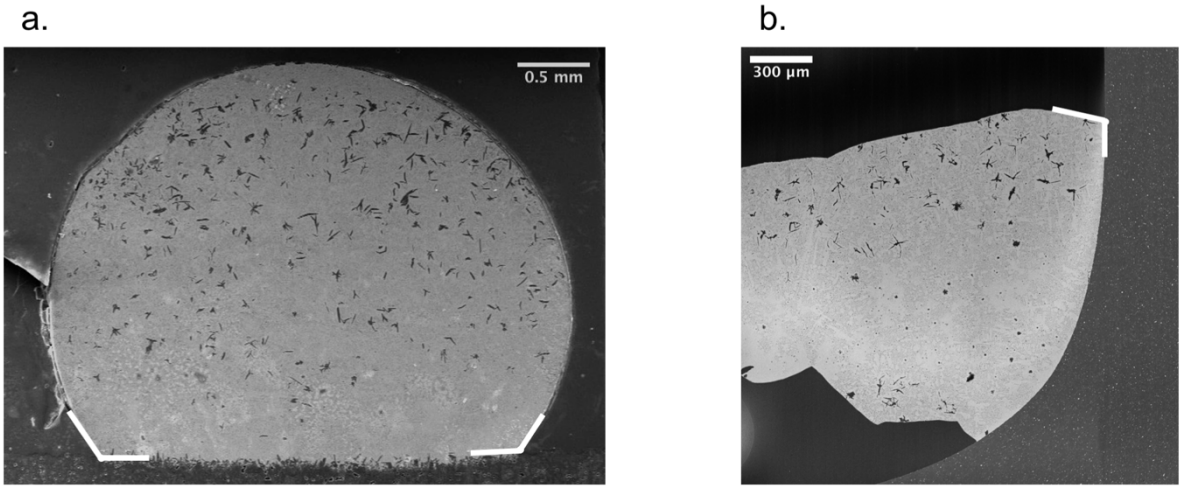

Figure 10.4. Measured contact angles from scanning electron micrographs. a.) metal within carbon crucible. b.) metal within MgO crucible, measured from the wall of the crucible. Metals that adhered to crucible walls were also measured in this way in addition to measurement of the angle with the crucible bottom.

10.5 Results and Discussion

Crucible interactions were used to determine if other crucibles were wetted by Fe-C_{sat}-Ti. The effects of crucible-metal interactions are quantified by the contact angles in Table 10.1. The numbers denote the minimum and maximum angles measured. Droplets within Al_2O_3 crucibles and the sintered CA crucible saw the metal adhere to the crucible wall, shown in Figure 10.5. The minimum angles were measured from the wall in similar fashion to MgO.

The angles are not from equilibrium conditions and will have changed somewhat upon cooling. The contact angles on different sides of the droplet could vary greatly.

This was particularly prevalent with graphite crucibles, due both to the inhomogeneity of the crystallite structure [20] and the dynamic variations that a system with Marangoni driven flow can experience [21].

Table 10.1. Contact angles between metal and crucibles

	Al_2O_3	MgO	Graphite	Al_2O_3 with CaF_2	Al_2O_3 with CA
Range of Contact Angles [°]	89 [a)]- 95	98 [a)]-100[a)]	119-127	120- 131	86[a)]-162

[a)]Measured from the top surface

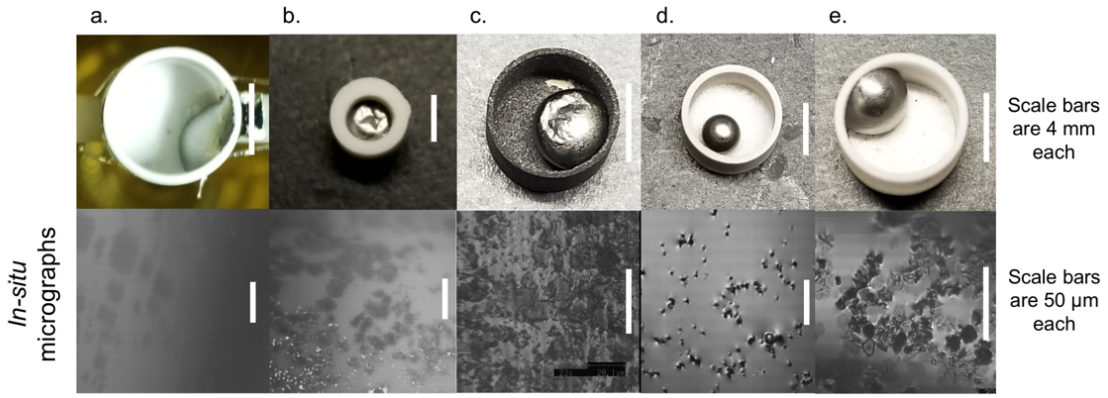

Figure 10.5. Images of wetting results (upper row) with in-situ CSLM micrographs (lower row). a.) Alumina b.) MgO c.) Graphite d.) Fluxed alumina. e.) Sintered CA crucible. The precursor material was the same for each, about 5.7% wt C with about 1% wt Ti (0.5% wt Ti).

Though the most important indication of wetting was the location of the metal at the end of the melt, the contact angle can be used in a semi-quantitative fashion to compare the crucible interactions. Metal melted in Al_2O_3 resulted in angles around 90°, and the droplets contained were unable to be removed from the crucible by hand. By comparison, the smallest angle of MgO differed from the largest of the Al_2O_3 by 3°. The angles for metal contained within graphite and the flux-coated crucible were even higher at minimum angles of 119° and 127°, respectively. The droplet within the sintered CA crucible, shown in Figure 10.6, had the widest range of contact angles. While the lowest angle with the CA crucible was 86°, however, this was measured from the top of the droplet, i.e., the interface with crucible wall. The angle measured from the vapor-CA-metal interface was higher at 162°. Droplets contained within the graphite crucible and fluxed crucible were able to be removed easily by hand. The metal contained within the sintered CA coating crucible could be removed with a bit more difficulty as the droplet adhered to the wall but not the coated surface. Metal was

unable to be removed from the MgO crucibles, but based on the wetting angles, this is likely a practical problem as the metal completely filled the smaller crucibles.

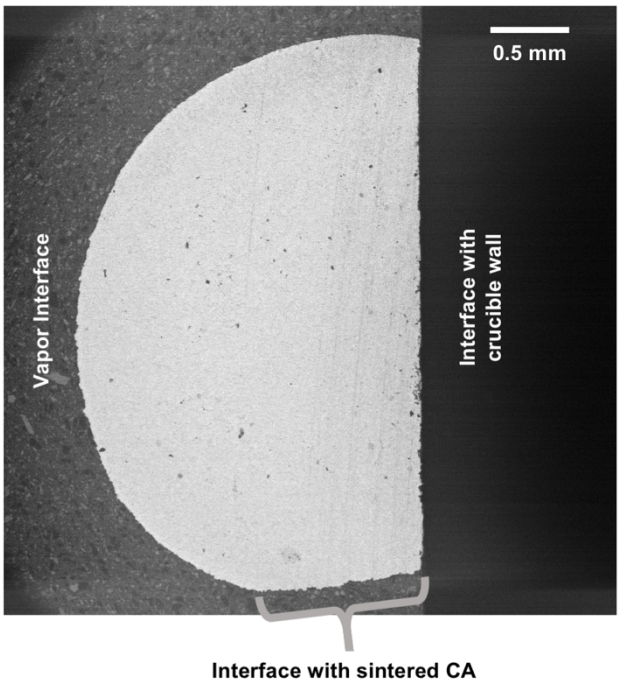

Figure 10.6. Vertical cross-section of sintered CA crucible

Despite being non-equilibrium, the wetting angles correlate with practical measures when using the CSLM: focus on the surface of the droplet is easier to achieve because the droplet has less curvature near its highest point. This can be seen in the resultant in-situ micrographs are coupled with the macroscopic images of the crucibles in Figure 10.5. For the droplet which wetted Al_2O_3, the curvature made it so that only a sliver of the image was in-focus. The others, which contained more spherical droplets, resulted in higher quality micrographs. This qualitative correlation can be explained by Figure 10.7: A planar solid (Figure 10.7a.) can have the entire sample surface at the focal plane. A non-wetting droplet (Figure 10.7b.) has a relatively flat surface at the top, which can be close to the focal plane. When the droplet wets the crucible walls (Figure 10.7c.), only a sliver of the image is in-focus as the droplet surface is aslant. It should be noted that, while quality, in-focus micrographs could be achieved by using a graphite crucible, graphite flakes obscured the metal surface over time, eliminating the usefulness of graphite crucibles for many in-situ experiments in the CSLM.

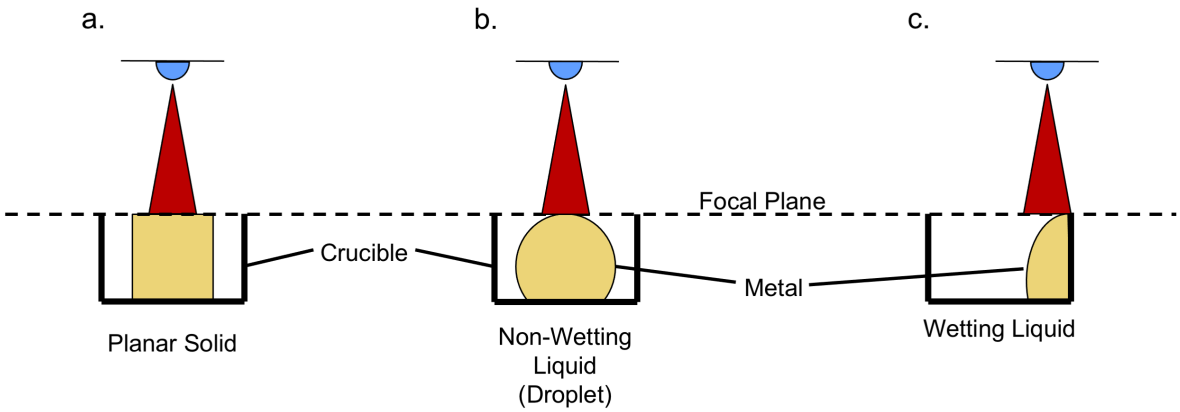

Figure 10.7. Schematic illustration of the focal plane and different sample shapes in the CSLM.

While the results give a practical solution to the problem of wetting and deteriorating micrograph quality, they do not explain why the wetting of alumina occurred. Though the metal wetted Al_2O_3, it did not wet the CaF_2-fluxed crucible, which had a composition that resulted in the activity of Al_2O_3 equal to 1 while the flux was liquid. The wetting of an oxide by metal, especially when well documented that primary pure metal does not wet, could mean either of two things: the influence of dissolved species or the presence of an interfacial reaction. P_{O_2} was well controlled to below 10^{-16} atm in the CSLM chamber for each experiment, eliminating this as the reason.

Some metals with dissolved Ti are reported to wet oxides when a certain Ti content is reached, but Fe is not one [5]. Shown in Figure 10.8, the two binary alloys Fe-C_{sat} and Fe-4% wt Ti were melted following the above procedure but did not wet the crucible. Because only the ternary (Fe-Ti-C) system wetted alumina, a layer of TiC was expected as the cause of wetting, as previously seen in a low carbon iron alloy [22]. A vertical cross-section of the Fe-C_{sat}-Ti system melted in an alumina crucible is shown in Figure 10.9. TiC particles adhered to the alumina, and this interaction was strong enough to pull Al_2O_3 grains away from the crucible upon solidification shrinkage, evidenced by the gap filled with epoxy. Though only a few TiC particles are seen in the cross-section, when viewing the part of the droplet that was in contact with the Al_2O_3 wall (Figure 10.10), a near complete layer of TiC can be seen with some attached Al_2O_3 grains. The carbide-oxide reaction layer was not thick enough to be seen by SEM, but it is reported that TiC and Al_2O_3 react to form a nano-scale Al-Ti oxycarbide layer at their interface [22,23]. The reported reaction mechanism includes the creation of CO at the interface, giving one indication why the binary Fe-Ti alloy did not wet though binary systems like Cu-Ti and Sn-Ti do wet Al_2O_3 [5].

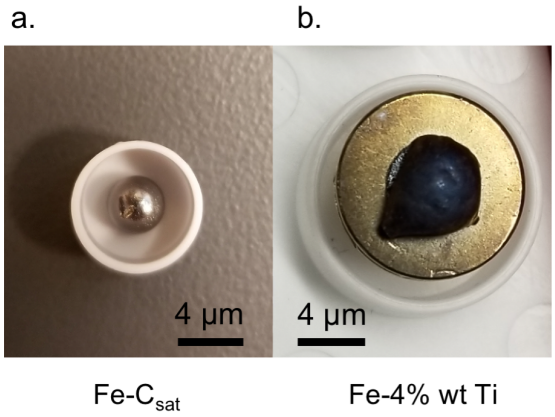

Figure 10.8. Binary alloys melted in Al_2O_3. a.) Fe-C_{sat}, and b.) Fe-4% wt Ti. The Fe-Ti alloy was removed from the crucible prior to the picture and is shown mounted on a microscope stub.

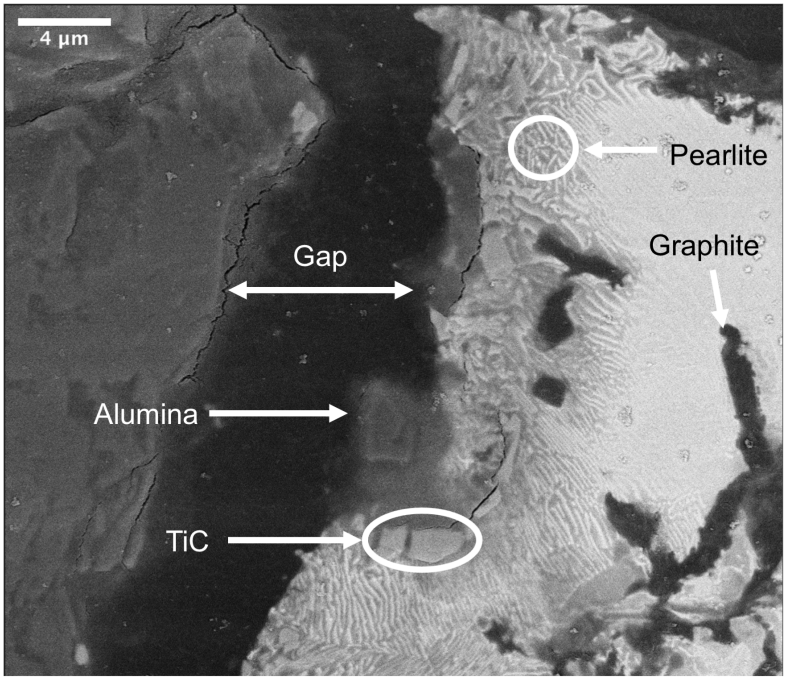

Figure 10.9. Vertical cross-section of Al_2O_3 crucible and 0.97% wt Ti alloy. (BSE)

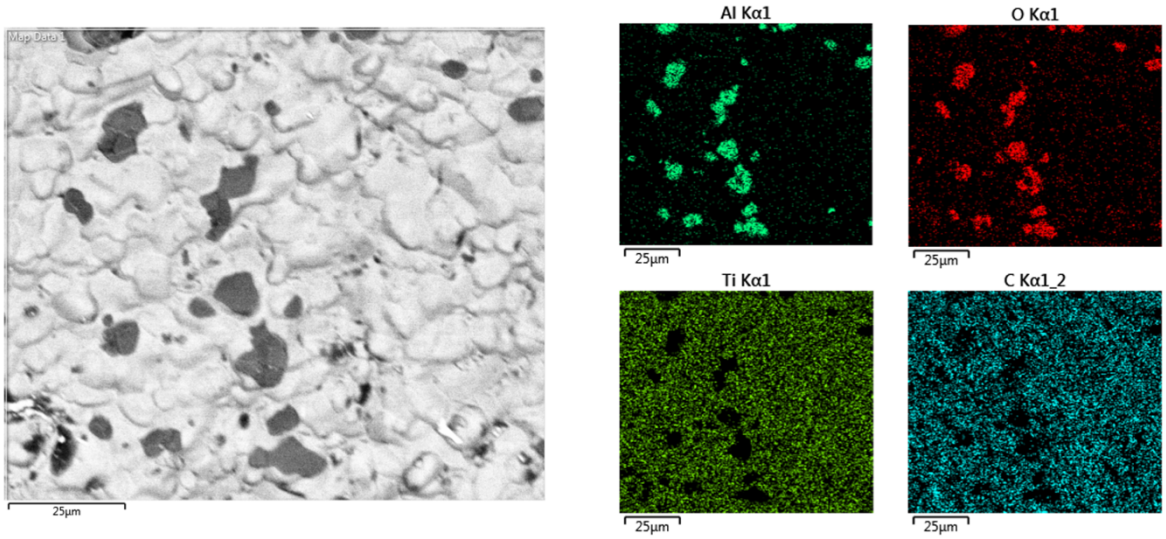

Figure 10.10. Micrograph and EDS map of the Fe-C_{sat}-Ti droplet previously in contact with an alumina crucible.

The phenomenon here is similar to that observed by Dezellus et al. where a Cu-Sn-Ti alloy was seen to reactively wet glassy carbon [24]. There, the dissolved Ti in the alloy reacted with glassy carbon substrate to create a layer of TiC. Fe-C_{sat}-Ti appeared to wet alumina macroscopically, odd from the "like wets like" rule of wetting. However, the metal was wetting TiC, not Al_2O_3. In reality, the metal wetted TiC, which formed a thin layer on the crucible. Only the Al_2O_3 crucible appeared to macroscopically wetted, because it was the only one to react with TiC.

Why the metal would not wet the coated crucibles, particularly the fluxed crucible deserves deeper investigation. The phase diagrams of the two slag systems are shown in Figure 10.11. For the fluxed system (in Figure 10.11a) the activity of alumina is 1 for the liquid system, and it would be expected that TiC should undergo a reaction similar to that of the pure alumina crucible. The morphology of the top of the Al_2O_3-CaF_2 flux coating along with energy-dispersive X-ray spectrum (EDS) and vertical cross section of the coated crucible are shown in Figure 10.12. The simulated spectra of different calcium aluminates were calculated with DTSA-II at 25 keV [25]. Notably, the fluorine peak at 0.677 keV [26] was absent from the measured spectrum despite the flux originally containing a majority of CaF_2. The fluorine loss occurred due to the high vapor pressures of fluorides, with AlF_3 predicted as the dominant gas species by FactSage 8.0. Rather than the flux surface coating containing CaF_2, the resultant coating had a composition nearest CA2, determined by the Ca/Al EDS peak ratio. The amount of Ca is expected to decrease into the thickness of crucible, and thermodynamics dictates the equilibrium phase at the coating-crucible interface would have to be CA6;

this decrease in Ca can be seen from the EDS line scan in Figure 10.13. CA2 is not in equilibrium with Al_2O_3, and therefore, there is no reaction with TiC. Without the reaction, a substrate of TiC does not form, disabling the wetting effect.

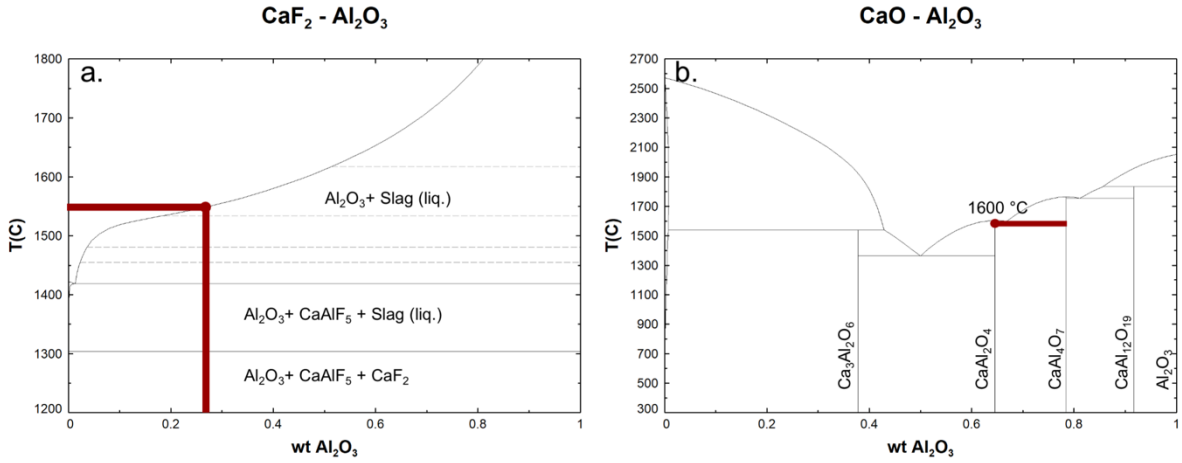

Figure 10.11. a.) Al_2O_3- CaF_2 phase diagram. b.) Al_2O_3-CaO phase diagram. Calculated with FactSage Oxide Database.

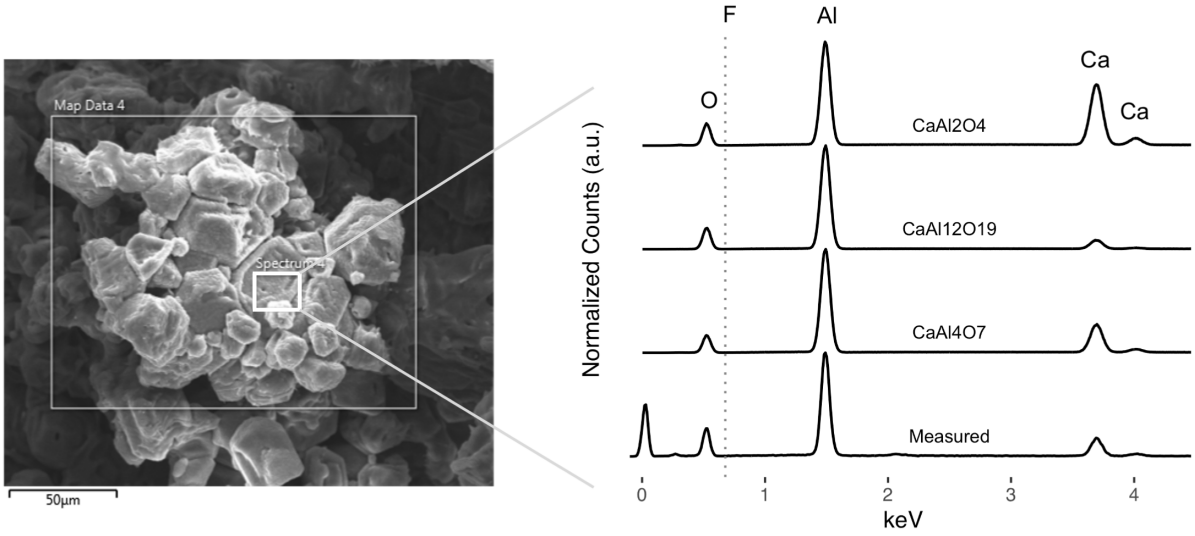

Figure 10.12. Morphology and EDS spectrum of fluxed crucible surface, with simulated spectra calculated with DTSA II at 25 keV.

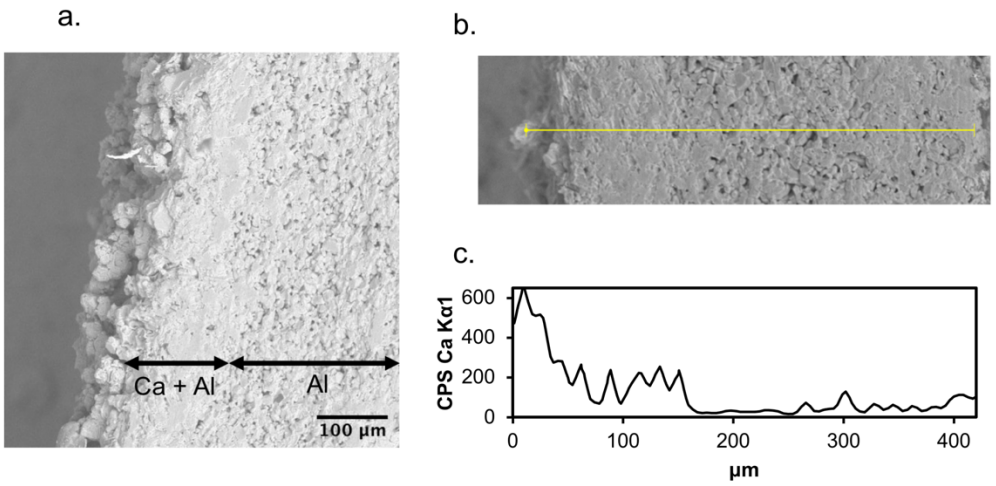

Figure 10.13. a.) Cross-section of the horizontal interface of Al_2O_3- CaF_2 crucible. b.) micrograph of interface coupled with c.) EDS line scan of Ca from the open portion of the crucible (left) into the bulk (right).

The fluxed crucible and the sintered CA crucible were similar chemically, but the fluxed crucible did a better job at completely preventing wetting. The fluxed crucible was more effective at preventing adhesion because the flux was able to coat the crucible walls rather than only coating the bottom. When viewing the top edge of a fluxed crucible, Ca could be identified from EDS, shown in Figure 10.14. Liquid fluxes and slags are generally wetting to Al_2O_3 substrates [27], allowing the flux to "climb" the crucible in similar fashion to the reactive wetting by Fe-C_{sat}-Ti. Thus, the problem of wetting was prevented by utilizing the wetting behavior of a different system.

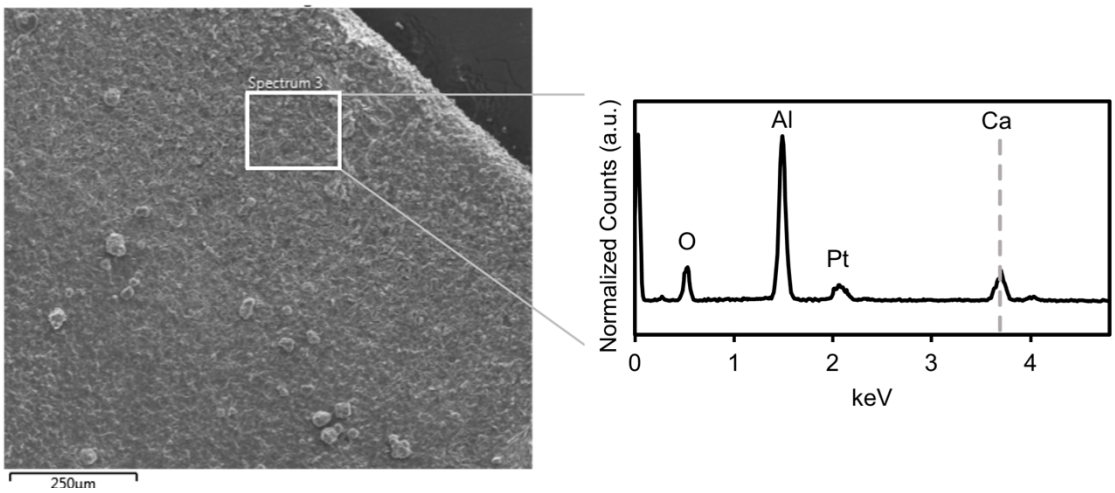

Figure 10.14. Micrograph of the top edge of a fluxed crucible with EDS spectrum. Notably the spectrum includes the peak for Ca at 3.69 keV [26]. The presence of Pt is due to the coating necessary for viewing the sample with SEM.

The flux created a consistent and adequate coating with little preparation. The inclusion of a volatile species had the advantage of utilizing wetting to fully coat the oxide while remaining fully solid after processing and during use. As a practical measure to prevent wetting, the following guidelines are suggested: the flux or slag must be able to melt completely at temperatures obtainable with available equipment and must be thermodynamically compatible to prevent consumption of the crucible.

10.6 Conclusions

Molten metals are not expected to wet solid oxides. Molten Fe-Ti-C_{sat} reactively wetted Al_2O_3 crucibles on a macroscopic level, and this occurred due to the formation of a layer of TiC that adhered to the Al_2O_3. Crucibles of graphite and MgO nor alumina crucibles with coatings exhibited this behavior, though samples melted in graphite crucibles became covered with graphite particles, eliminating any usefulness for in-situ experiments. The wetting was caused by a reaction layer that adhered TiC to the alumina crucible which and the TiC was then wetted by the molten metal. With alumina crucibles coated in either an Al_2O_3- CaF_2 flux or sintered CA particles, the reactive wetting was prevented. Though the original composition of the flux had Al_2O_3 activity equal to 1 (the reaction layer was expected to form), the volatilization of the fluorine from the flux created a calcium aluminate layer. The wetting of the crucible walls by the liquid flux gave it advantage over the sintered CA crucible which provided incomplete coverage.

10.7 Hypothesis Revisited

The wetting of alumina by Fe-C_{sat}-Ti can be prevented by coating the crucible in a thin layer of liquid flux. This should raise the angle of contact by at least 10°.

This hypothesis was supported. The angle of wetting was raised by a minimum of 15° when the alumina crucible was coated with flux.

10.8 References

[1] Y. Yang, K. Raipala, and L. Holappa: in *Treatise on Process Metallurgy, Volume 3: Industrial Processes*, S. Seetharaman, A. McLean, R. Guthrie, and S. Sridhar, eds., 3A edn., Elsevier, 2014, pp. 60–1.

[2] R.J. Fruehan: *ISS Trans.,* 1985, vol. 6, pp. 43–9.

[3] L. Shao and H. Saxén: *Steel Res. Int.,* 2012, vol. 83, pp. 878–85.

[4] R. Beheshti, J. Moosberg-Bustnes, M.W. Kennedy, and R.E. Aune: *Ironmak. Steelmak.*, 2016, vol. 43, pp. 394–402.

[5] J. Naidich: *Prog. Surf. Membr. Sci.,* 1981, vol. 14, pp. 353–484.

[6] O. Dezellus and N. Eustathopoulos: *J. Mater. Sci.*, 2010, vol. 45, pp. 4256–64.

[7] C. Wu, R. Wiblen, and V. Sahajwalla: *Metall. Mater. Trans. B*, 2000, vol. 31, pp. 1099–104.

[8] K.I. Ohno, T. Miyake, S. Yano, C.S. Nguyen, T. Maeda, and K. Kunitomo: *Tetsu-To-Hagane/Journal Iron Steel Inst. Japan*, 2016, vol. 102, pp. 684–90.

[9] A.W. Cramb and I. Jimbo: *Steel Res.,* 1989, vol. 60, pp. 157–65.

[10] C. Bernhard, G. Xia, A. Karasangabo, M. Egger, and A. Pissenberger: *7th ECCC, METEC InSteelCon 2011, 7th Eur. Contin. Cast. Conf. Dusseldorf, Ger.*, 2011, p. Session 17, Paper ECCC-58, pp.1–12.

[11] D. Bergsma and R.J. Fruehan: *60th Ironmak. Conf. Proc.,* 2001, pp. 297–312.

[12] P. Xiao and B. Derby: *Acta Mater.,* 1996, vol. 44, pp. 307–14.

[13] Y. Li, Y. Li, and R.J. Fruehan: *ISIJ Int.,* 2001, vol. 41, pp. 1417–22.

[14] T. Britt and P.C. Pistorius: *Metall. Mater. Trans. B*, 2021, vol. 52, pp. 1–5.

[15] M. Sumito, N. Tsuchiya, K. Okabe, and K. Sanbongi: *Trans. Iron Steel Inst. Japan*, 1981, vol. 21, pp. 414–21.

[16] P. Ni, H. Goto, M. Nakamoto, and T. Tanaka: *ISIJ Int.*, 2020, vol. 60, pp. 1586–95.

[17] C.S. Nguyen, K.I. Ohno, T. Maeda, and K. Kunitomo: *ISIJ Int.*, 2017, vol. 57, pp. 1491–8.

[18] M.M. Sun, J.L. Zhang, K.J. Li, S. Ren, Z.M. Wang, C.H. Jiang, and H.T. Li: *JOM*, 2019, vol. 71, pp. 4305–10.

[19] P.C. Pistorius and N. Verma: *Microsc. Microanal.,* 2011, vol. 17, pp. 963–71.

[20] M.-M. Sun, J.-L. Zhang, K.-J. Li, H.-T. Li, Z.-M. Wang, C.-H. Jiang, S. Ren, L. Wang, and H. Zhang: *JOM,* 2020, vol. 72, pp. 2174–83.

[21] Y. Chung and A.W. Cramb: *Metall. Mater. Trans. B*, 2000, vol. 31, pp. 957–71.

[22] M. Gelbstein, N. Froumin, and N. Frage: Mater. Sci. Eng. A, 2008, vol. 495, pp. 159–63.

[23] Y. Kim and J. Lee: *J. Am. Ceram. Soc.,* 1989, vol. 72, pp. 1333–7.

[24] O. Dezellus, F. Hodaj, A. Mortensen, and N. Eustathopoulos: *Scr. Mater.*, 2001, vol. 44, pp. 2543–9.

[25] N. Ritchie, *NIST DTSA-II*, https://www.nist.gov/services-resources/software/nist-dtsa-ii.

[26] A. Thompson, D. Attwood, E. Gullikson, M. Howells, J. Kortright, A. Robinson, and others*: X-Ray Data Booklet*, Lawrence Berkeley National Laboratory, Berkeley, CA, 2009.

[27] J.Y. Choi and H.G. Lee: *ISIJ Int.*, 2003, vol. 43, pp. 1348–55.

11 Investigation into the Temperature of Metallic High-Temperature Confocal Scanning Laser Microscope Samples

This chapter modified from its original form in the journal
Metallurgical and Materials Transactions B:

S. T. Britt and P. C. Pistorius, "Investigation into the Temperature of Metallic High-Temperature Confocal Scanning Laser Microscope Samples," *Metall. Mater. Trans. B*, Apr. 2022. DOI: 10.1007/s11663-022-02515-4.

11.1 Abstract

In high-temperature confocal scanning laser microscopy (CSLM), the top of the opaque sample is observed while being heated by thermal radiation from an incandescent heating element, reflected from the inside of an ellipsoidal chamber. The temperature is measured with a thermocouple in the sample holder. The true temperature at the top of the sample differs from the measured temperature because of thermal contact resistance (between the metallic sample and the crucible, and between the crucible and the sample holder) and because of temperature gradients within the sample. Assessment of these differences is important for accurate experiments. The method of accounting for the difference between the true sample temperature and the measured temperature was found to have an error of ± 12.5 °C when melting pure metals in MgO crucibles. Temperature gradients within the sample were investigated by observing MgO particles flowing on liquid iron and comparing with a finite element model. Particles near the top of the droplet had median velocities around 20 μm/s. The model (which included radiative heating) predicted a velocity of 3 mm/s with temperature difference of 1.2 °C over the droplet height. The real droplet is expected to have a difference of much less than 1 °C.

11.2 Within the Narrative

The CSLM was an often-used tool for the duration of this thesis. In recording the formation temperature of TiC or Ti(C,N) particles (Ch. 9), knowledge of the surface temperature was vital. This work seeks to illuminate temperature conditions with the sample, extending the knowledge of conditions within the CSLM not just to help the work contained in this thesis, but to assist the broader community to enable the use of this instrument for more quantitative experiments.

11.3 Introduction

The high-temperature confocal scanning laser microscope (CSLM) is a critical tool for the metallurgist. Viewing metals *in-situ* is advantageous for studying thermodynamics, oxidation, phase transformations, mass transfer, and non-metallic inclusions [1–10]. Many researchers have used the microscope for qualitative *in-situ* observations, but there are also advantages of using the CSLM for *ex-situ* experiments due to the fast heating and cooling rates, small sample size, and controlled atmosphere [11,12]. Few studies have been published using quantitative observations, though there are exceptions [9,13,14]. Despite increasing utilization of the CSLM, the conditions within metal samples heated by the CSLM remain relatively unknown. Two examples of this are the unknown thermal gradients within the metal and the lack of a fundamental understanding of the temperature offset between the measured temperature (at the thermocouple on the sample support) and the actual sample temperature.

Knowing the temperature distribution is important for experiments observing the flow of molten metal. CSLM samples have a high area-to-volume ratio. As an industrial example, in an electric arc furnace containing 150 tons of steel with inner diameter of 6 m, the ratio of the bath area to the steel volume is around 1.2 m^{-1}. For a hemispherical droplet with a diameter of 2 mm, as in the CSLM, the ratio of the exposed area to volume is 3000 m^{-1} (or 3 mm^{-1}). The large specific surface area, small size, and non-uniform temperature of CSLM samples result in Marangoni flow [15,16], unlike flow conditions in industrial processes and even laboratory-scale melts. Piva et al. predicted that the large specific surface area of the CSLM sample and radiative heat loss would result in a 20 K temperature difference between the top and bottom of the droplet [16].

Marangoni flow is driven by gradients in surface tension, which depend on the temperature and sample composition. The surface tension (σ) at a certain temperature (T) can be represented by Eq. 1, where σ_0 is the surface tension at the melting temperature, $\frac{d\sigma}{dT}$ is the temperature dependence of surface tension, and T_m is the melting temperature of the metal. $\frac{d\sigma}{dT}$ is negative for most pure metals [17], though the value can be positive in the presence of surface-segregated elements. For pure metals, a higher temperature results in a lower surface tension, and a larger temperature gradient would promote higher liquid velocities because of a larger surface tension gradient.

$$\sigma = \sigma_0 + \int_{T_m}^{T} \frac{d\sigma}{dT} dT \qquad \text{Eq. 1}$$

The model by Piva et al. predicted Marangoni-driven flow rates as high as 45 mm/s for a liquid steel droplet in an alumina crucible [16]. The model used a simple boundary condition by setting the bottom crucible surface to 1600 °C, with all other free surfaces experiencing radiative heat loss. However, the thermal boundary conditions of the CSLM are more intricate. The CSLM heats samples with a halogen lamp in an ellipsoidal mirror chamber; the lamp is centered roughly at one focal point, and the sample is placed at the other focal point. Given this configuration, the sample receives radiation from all sides (due to reflections from the mirror chamber) rather than heating solely on the crucible bottom. Heating that includes mirror reflections would be more homogeneous than predicted by Piva et al [16]. but would not be completely uniform as a certain amount of energy is lost during each reflection, subject to the mirror's emissivity (ε); in addition, radiation escapes through the fused-quartz window at the top of the chamber. Figure 11.1 illustrates the differences between the model of Piva et al. and the mirror chamber model used in the current work.

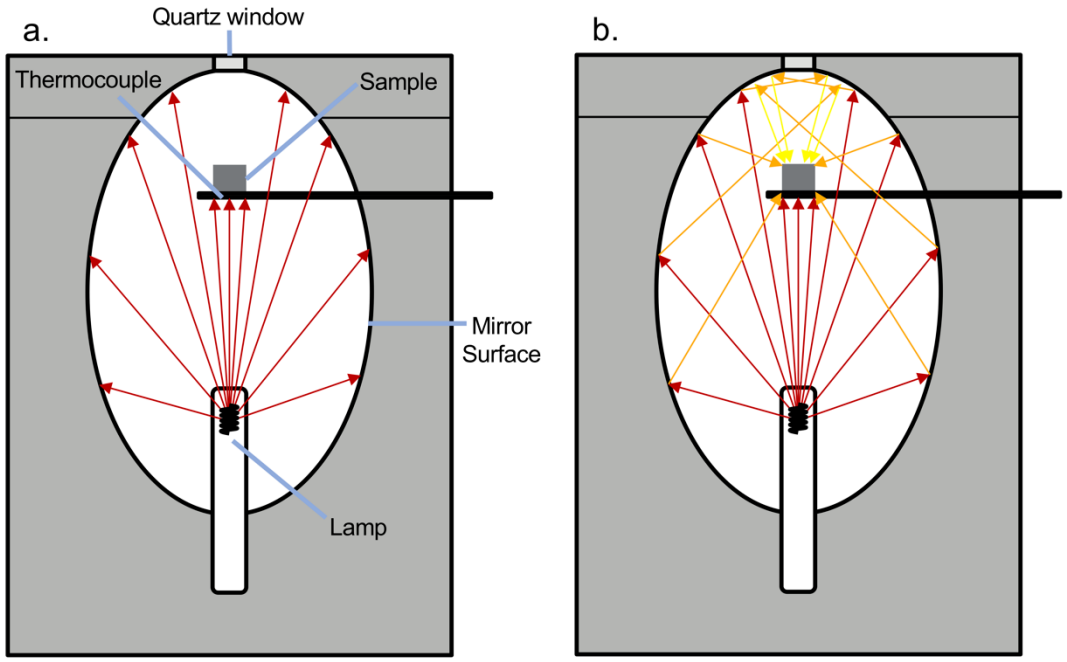

Figure 11.1. a.) Schematic of light rays traced from halogen lamp to sample similar to the Piva et al. boundary condition [16]. b.) Schematic of light rays traced from halogen lamp to sample including reflections. Red rays carry the most energy. Orange rays have lost energy due to one reflection, and yellow rays have lost the most energy due to two reflections.

Inhomogeneous heating is thought to contribute to the difference in temperature between the thermocouple (TC) and the metal sample. The difference is typically quantified by observing phase transformations that occur at well-known temperatures. For example, pure copper (melting point 1085 °C) has been seen to melt with the

thermocouple reading as high as 1165 °C using the instrument described later. The common practice to account for this offset is to establish a calibration curve by observing the melting of pure Cu and pure Fe. A linear relationship is created from the two observed melting points to predict the temperature of the sample based on the TC temperature. However, this method assumes that the offset is independent of material, an assumption not investigated in the literature. Rather than seeing an offset dependent on temperature, Yin and Emi found that the temperature offset of a low-carbon steel sample was roughly constant between 1600 and 1720 K [15]. In a different steel, Arai et al. found similar results over a 40 K range [18]. However, there has not been comparable work observing samples at lower temperatures or a material with higher thermal conductivity than steel.

The present work describes two issues with performing quantitative, temperature dependent CSLM experiments: the dependence of the temperature offset on material and the incomplete understanding of the temperature gradients which drive fluid flow within the droplet. The former is investigated by melting a series of pure metals and comparing the assumed linear relationship to the observed offsets. The latter is investigated both by *in-situ* observation and by a finite-element model. The model improves on that presented in literature [16] by including heating by halogen lamp in mirror furnace.

11.4 Methods

11.4.1 CSLM Features

The CSLM manufactured by Yonekura consists of a water-cooled mono-ellipsoidal mirror furnace with 1.5 kW halogen lamp. The heating chamber is stainless steel, plated with gold and polished to a mirror finish. A B-type thermocouple (TC) connected to a disk-shaped platinum sample support (8 mm diameter, 0.25 mm thick) rests on an alumina rod, with the disk located in the vicinity of the upper focal point of the ellipsoidal chamber; the halogen lamp is roughly centered on the lower focal point. A red laser (632.8 nm wavelength) shines through a fused-quartz window at the top of the chamber to view samples *in-situ*. For this study, the p_{O_2} was controlled below 10^{-21} atm by flowing either argon or an argon plus 5% hydrogen mixture through a Cu getter, two Mg getters, and one desiccator before flowing to the furnace. p_{O_2} was monitored by an oxygen probe heated to 700 °C in a tube furnace at the outlet.

11.4.2 Methods for Material Dependence of Temperature Offset

To obtain the temperature offset, a sample of a pure metal (Ag, Au, Cu, Fe, or Ni) was placed in an MgO crucible (70 µL, 3.16 mm internal diameter) on the sample holder, and the CSLM chamber was sealed, evacuated, and backfilled with argon. (Sample masses are mentioned below.) The melting points of Au and Cu differ by only 20 °C; hence samples of the two metals would have similar temperature offsets if the offset were material independent. Metals were heated according to the different profiles shown in Figure 11.2. Profiles were developed for samples to melt during a 30 °C/min increase in temperature. When the samples were heated to the last set temperature, the temperature was further increased at 30 °C/min until the sample melted. The melting temperature was recorded (based on the visible change in sample shape), and a hold function was used to cool the sample enough to solidify (~20 °C below the observed melting point). The temperature was subsequently raised in 5 °C increments until the sample melted again. This process was repeated until the metal was melted at least three times.

The metal samples (Cu, Ag, Au, Fe, and Ni) had masses around 0.09 g. An additional Au sample was tested, with a similar volume to the Cu and Ag samples. Since Au is approximately twice as dense as Cu and Ag, the larger Au sample had a mass of 0.188 g.

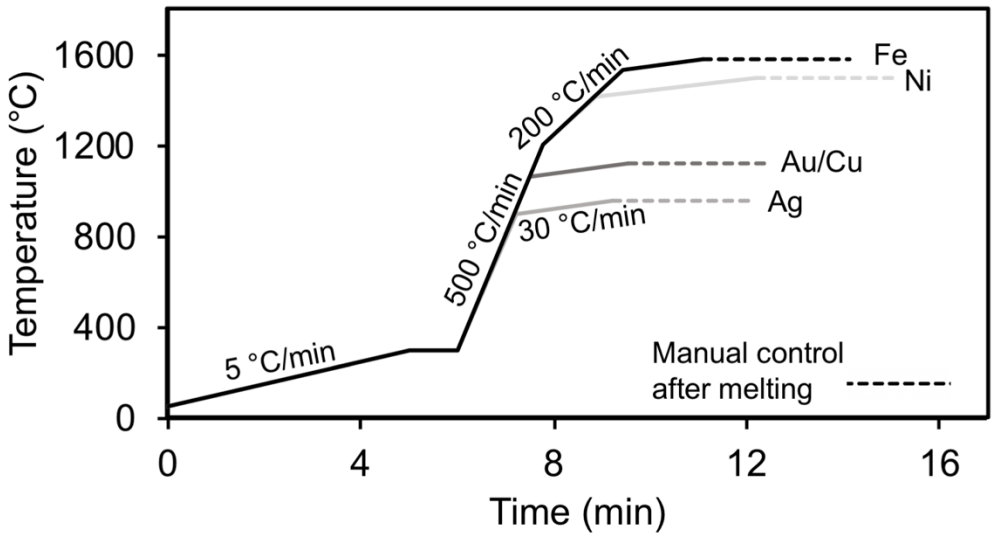

Figure 11.2. Heating profile for temperature offset experiments. All temperatures are nominal.

11.4.3 Particle Tracking

To serve as flow tracers, approximately 0.6 mg MgO powder, with particle size approximately 3.5 µm, was added to pure Fe (0.07 g) previously melted in an MgO

crucible (70 µL). The MgO crucible containing the metal sample and tracers was placed on the thermocouple holder, and the CSLM chamber was sealed, evacuated, and backfilled with argon. The p_{O_2} during particle tracking was kept below 5×10^{-23} atm. Samples were heated according to the profile in Figure 11.3. When the sample temperature reached 1600 °C (to ensure melting) a hold was initiated and the temperature was manually decreased and held at 1580 °C. The temperature was held at 1580 °C while videos of the sample surface were recorded at 10 frames per second with a resolution of 960×720. The 10x objective lens provided both enough magnification to identify particles and a field of view large enough to observe the same particles in multiple frames (to enable tracking).

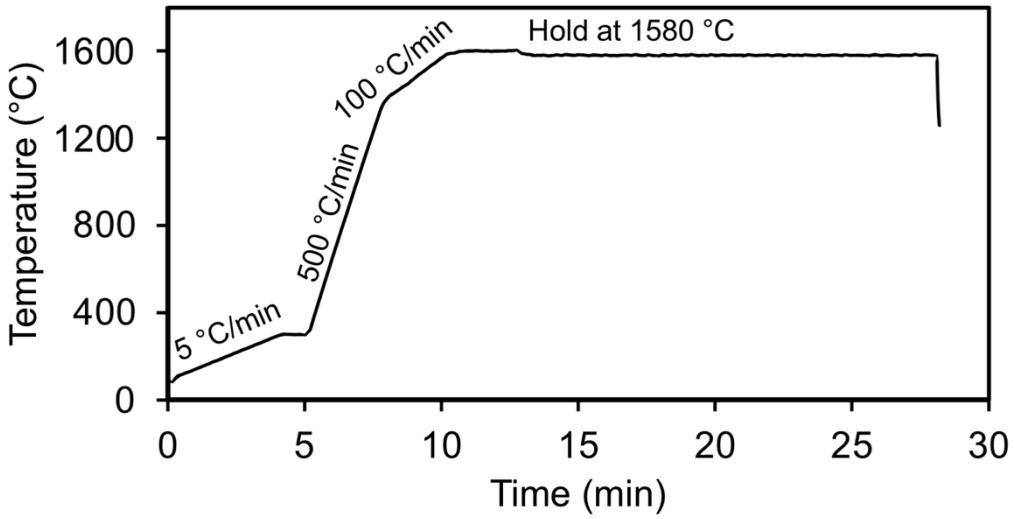

Figure 11.3. Heating profile for particle flow experiments. All temperatures are nominal.

To compare the results to the finite-element simulation, the position of the field of view relative to the highest point of the droplet surface must be known. (This is because – as shown below – the surface flow rate depends strongly on position on the droplet surface.) This was done by "chasing" the focal plane with the microscope, illustrated in Figure 11.4. As the focal plane of the microscope was raised, the band of high intensity (the in-focus part) would move towards the top of the sample. A cycle of raising the focal plane and moving the stage could be repeated until raising the focal plane resulted in the entire image darkening (Figure 11.4c.). At this point the stage was centered on the topmost point of the droplet, and the relative position of subsequent images could be read from the stage micrometers. Three regions of the droplet were recorded, one at the highest point of the droplet (center), one 280 µm "North" of center, and one 190 µm "South" of center. Flow at each location was recorded for at least 30 seconds.

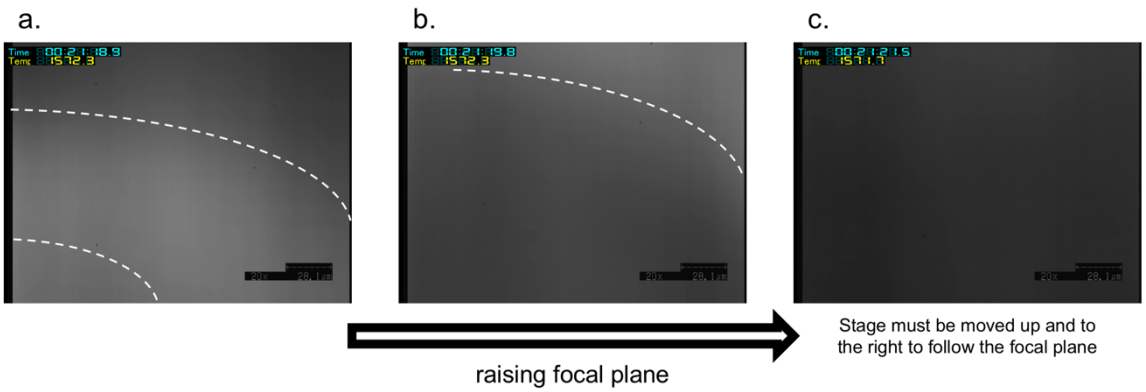

Figure 11.4. Series of micrographs illustrating "chasing" the focal plane to find the top of the sample. Dotted white lines outline the region of higher intensity, i.e., the part that was in-focus. a.) Micrograph in focus. b.) After focal plane was raised. The stage was moved towards the top right to follow the focus. c.) Focal plane has moved above the droplet.

11.4.4 Image Processing

The observed MgO particles showed little contrast with the molten bath. Particles were detectable by eye, but single-step image processing such as edge detection and thresholding was unable to isolate the particles to allow automatic tracking. The resulting image processing steps needed to isolate particles are shown by Figure 11.5. Images captured from the CSLM (Figure 11.5a) were converted to 8-bit black and white images and cropped to remove the information overlays and letterboxing (Figure 11.5b). The ImageJ plugin "Trainable Weka segmentation"[19] was used to segment the particles from the melt (Figure 11.5c). The plugin uses a set of machine learning algorithms to perform semantic segmentation, distinguishing particles from the iron bath. Three classes were identified from a single image to train the segmentation algorithm: class 1 was MgO particles (red in Figure 11.5c), class 2 was the molten bath (green in Figure 11.5c), and class 3 contained instrument artifacts such as banding caused by the laser rastering (purple in Figure 11.5c). The segmentation produced images of three intensities, one for each group. A threshold was applied to the resulting images so that particles (formerly red) became white with all else becoming black.

The ImageJ plugin "TrackMate" was used to identify particles and track motion [20]. Particles were detected with the "Laplacian of Gaussian (LoG)" detector (settings 15 px diameter and 0.1 threshold) and were automatically filtered based on quality. The simple "Linear Assignment Problem (LAP)" tracker was used to track the particles with maximum linking distance of 100 px. The resultant image with all particle tracks is shown in Figure 11.5d. Statistics of the traced particles were exported to a CSV file which recorded the change in position of every particle between each pair of

subsequent frames as a separate data point. For each set, at least 4500 particles were identified. Each change in particle position was divided by the effective frame rate (see the following paragraph) to obtain the velocity of each particle for a pair of frames.

Because there was a mismatch between the recorder frame rate and the laser raster rate, parts of the recorded images were the same between frames. This resulted in erroneous near-zero velocities when using particle images from consecutive frames. Rather than using every frame, every x^{th} frame was used instead. For example, if x was 3, every third frame would be used in the tracking algorithm. The effect on the velocity distribution is illustrated with the Southern observation set shown in Figure 11.5e. With x as 1 or 2 (using every frame or every other frame), there were many particles with erroneously near-zero velocity values, sufficient to reduce the median velocity to near zero. With $x \geq 3$, the medians converged, eliminating the effect of mismatched frame rates. Higher values of x resulted in fewer high-velocity outliers. High-velocity outliers often resulted from misidentification of particle pairs: between frames, particles on parallel paths could falsely be identified as the same particle, leading to an increased velocity when compared to correct particle identification in a subsequent frame. The data presented here used every 5^{th} frame (x=5) to combine the elimination of false near-zero velocities and to reduce the number of high-velocity outliers.

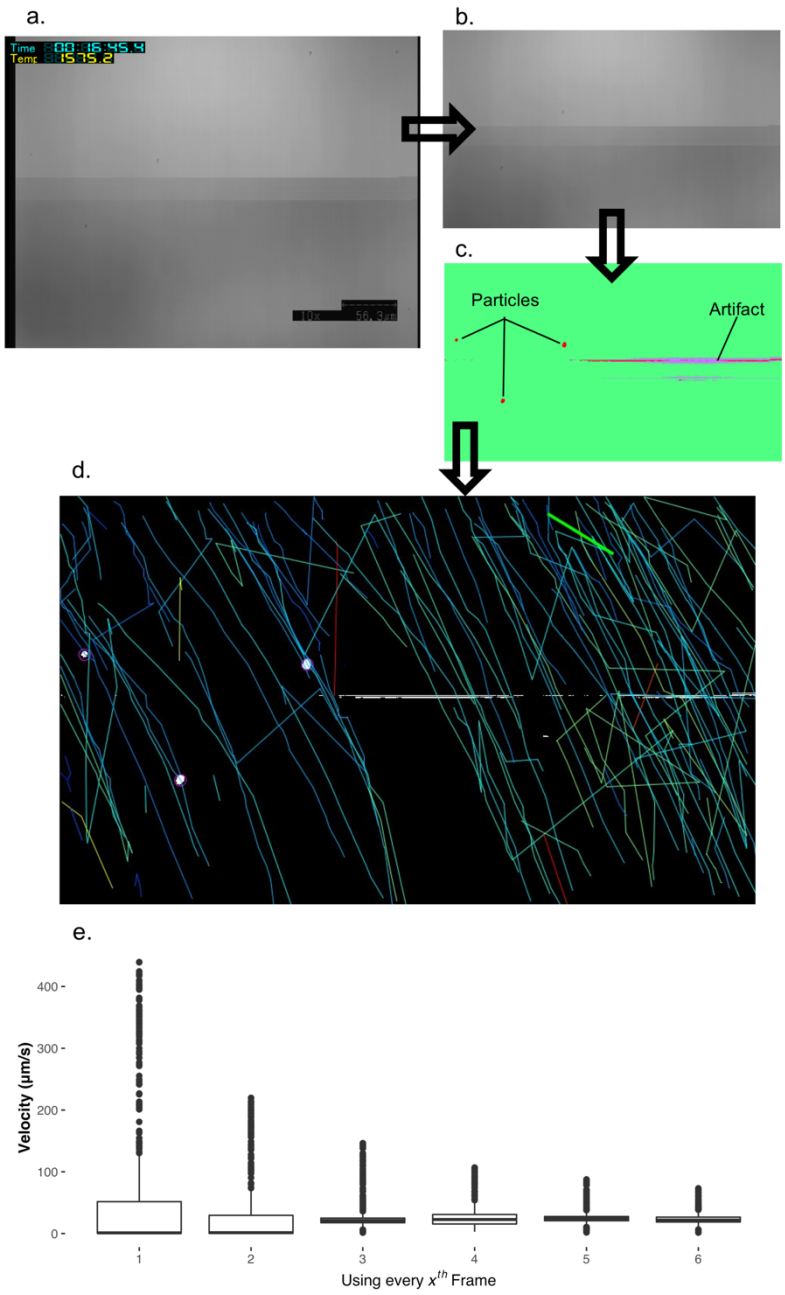

Figure 11.5. CSLM image processing flowchart. a) original image. b.) image cropped and converted to 8-bit. c.) image after segmentation. Identified particles are red; the molten bath is green; image artifacts are purple. d.) resulting image after thresholding and particle tracking. White circles are particles from the current frame. Lines represent all particle tracks with a gradient from red to blue indicating faster to slower velocity. e.) velocity results of using every x^{th} frame.

11.4.5 Model Description

A model combining the fluid flow, surface radiation, and heat transfer of the CSLM and metal sample was constructed using COMSOL 5.5 [21]. COMSOL is a multiphysics, finite element analysis software. This finite element model (FEM) improved on the steady-state 2D axisymmetric model of Piva et al. [16] by adding the mirror chamber and halogen lamp to the simulation. Model geometry is shown in Figure 11.6. The origin of the model was the intersection of the axis of symmetry, the Pt sample support, and the MgO crucible. A combination of two half ellipsoids was used to create the metal droplet shape. One half ellipsoid (defining the bottom of the droplet) was downward facing with a height of 2.2 mm and width of 1.58 mm. The second half ellipsoid (defining the top of the droplet) was upward facing with height of 1.2 mm and width of 1.67 mm. This geometry was based on scans with a Keyence VR-5000 white-light optical profilometer of an empty crucible and the crucible containing the metal droplet observed in the experiment. The 3D profiles were reduced to 2D slices, and the slice shown in Figure 11.6b was selected as reference for the model geometry. In the experiment, the highest point of the solidified droplet was not in the center of the crucible, but the simulation assumed it was centered. The height of the second half ellipsoid was selected so to match the curvature of the experimental droplet at a position 900 μm away from the highest point. During optical profilometry, reflections from the crucible left a gap in the measurement between the center of the crucible and the wall; the bottom of the sample was assumed to be flat (though simulations with a rounded bottom showed little difference). Only the top of the droplet was adjusted when changing the droplet size.

The cavity of the ellipsoidal chamber has a major axis of 4.85 cm and a focus of 3.5 cm. The origin of the model was the upper focal point, shown with red dot in Figure 11.6c. The filament was modeled as a set of six circular rings, spaced 3.75 mm apart vertically, with cross-sectional radii of 0.65 mm, located 2.85 mm from the axis of symmetry. The center of the bottom-most filament circle was 78.4 mm below the origin. The open space between the top of the chamber and the axis of symmetry represented the quartz window. Simulations used a maximum element size of 0.05 mm for the sample and 1.94 mm for the chamber.

The governing equation for heat transfer is Eq. 2, that for fluid flow by Eq. 3, and that for radiation by Eq. 4, with a description of variables in Table 11.1. The power supplied to the filament was used as a thermal boundary condition which provided a direct comparison of the model to the physical system. As the chamber was cooled by pumping chilled water, the bottom and vertical surfaces of the chamber were set to 20

°C. All surfaces were assumed to be ideal gray bodies, with reflectivity defined as one minus emissivity. For fluid boundary conditions, the free surface of the droplet was governed by Marangoni flow, the interface between the crucible and metal was a no-slip boundary, and a constant pressure was set at the intersection of atmosphere, crucible, and metal.

$$\rho C_p \boldsymbol{u} \cdot \nabla T + \nabla \cdot \mathbf{q} = \mathrm{Q} \quad \text{Eq. 2}$$

$$\rho(\boldsymbol{u} \cdot \nabla)\boldsymbol{u} = \nabla \cdot [-\mathrm{p}\mathbf{I} + \mu(\nabla \boldsymbol{u} + (\nabla \boldsymbol{u})^{\mathrm{T}})] + \boldsymbol{F} + \rho \boldsymbol{g} \quad \text{Eq. 3}$$

$$J = \varepsilon \sigma_{SB} T^4 + G \quad \text{Eq. 4}$$

Table 11.1. Description of variables for finite element model

Symbol	Description
ρ	Density (kg/m^3)
C_p	Specific heat capacity at constant pressure (J/(kgK))
$\boldsymbol{u}$	Velocity vector (m/s)
T	Absolute temperature (K)
$\mathbf{q}$	Heat flux vector (W/m^2)
Q	Heat from external sources (W/m^3)
p	Pressure (Pa)
$\mathbf{I}$	Identity tensor (-)
$\boldsymbol{F}$	Volume force vector (N/m^3)
$\boldsymbol{g}$	Acceleration of gravity vector (m/s^2)
μ	Dynamic viscosity (Pa*s)
γ	Temperature derivative of surface tension (N/(m*K))
J	Net radiative flux (W/m^2)
ε	Emissivity (—)
σ_{SB}	Stefan-Boltzmann constant (W/(m^{2}K^4))
G	Incoming radiative flux (W/m^2)

Care was taken to ensure the values used for the thermophysical materials properties were at the proper temperature. Table 11.2 shows the density at the melting temperature (ρ), emissivity (ε_{metal}), thermal conductivity (k), constant pressure heat capacity (C_p), and the coefficient of thermal expansion (CTE) for the materials used in the simulations. Density for solids was calculated at the melting temperature using the CTE. Stainless steel (316) was used as the material for the chamber walls and used room-temperature properties. Table 11.3 shows the temperature dependent density (ρ(T)), dynamic viscosity (μ), and surface tension (σ) for the simulated liquid iron with T being the temperature of the sample in K and T_{melt} being the tabulated melting temperature in K.

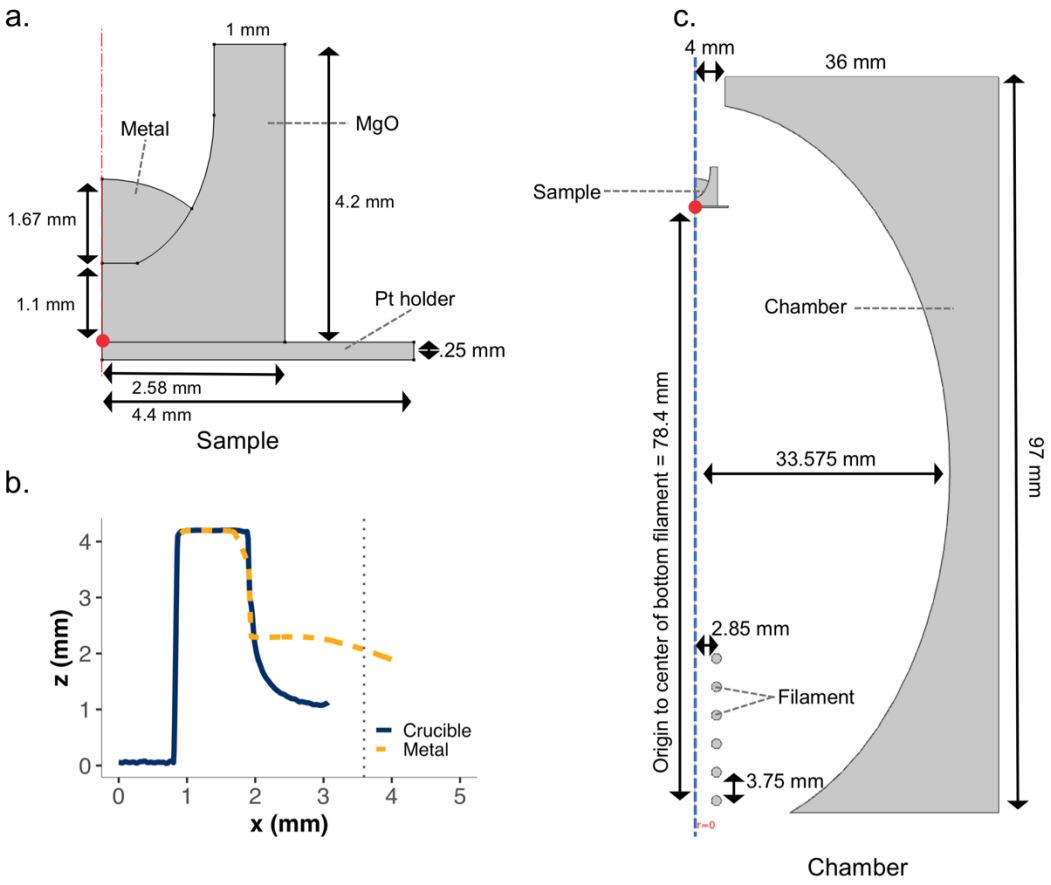

Figure 11.6. Geometry for finite element model. a) MgO sample geometry compared to b.) The results of non-contact profilometer. The dotted line denotes the axis of revolution. c.) Chamber geometry. In a.) and c.), the red dots indicate the location of the origin.

Table 11.2. Material Properties for Finite Element Model

Material	ρ (g/cm^3)	ε	k (W/m*K)	C_p (J/kg*K)	CTE (10^{-6}/K)
Ag	9.47	0.11	362	310* [22]	28.4
Au	17.7	0.21	247	162* [22]	22.1
Cu	8.08	0.15	330	504	25.8
Fe (*liq.*)	ρ(T)	0.4	33	900	—
MgO	3.45***	1* [23]	7* [24]	1341* [25]	—
Pt	20.1	0.15* [26]	63* [27]	176* [27]	11.3* [27]
316 St. Steel	7.95**	—	13.7**	470**	—

*All properties are from [17] unless noted with a reference

** Room temperature property

*** Manufacturer specified at room temperature

Table 11.3. Temperature Dependent Liquid Properties for Finite Element Model [17] (*T* in Kelvin)

Material (*liq.*)	*ρ(T)* (g/cm^3)	μ (mPa*s)	σ (mN/m)
Fe	7.035-9.26*10^{-4}(T-T_{melt})	.191*exp(51500/8.314/T)	1872 - 0.49 * (T-1811)

Values as low as 0.021 for the emissivity of gold have been reported, but the emissivity can change depending on the surface condition [28]. For the CSLM, this has been seen when melting pure iron (1538 °C) in an Al_2O_3 crucible. If the instrument was used extensively since the last cleaning, the power of the lamp can reach its maximum limit without melting the iron, indicating less reflection from the mirror (caused by an increase in mirror emissivity). It was found that the same iron sample could be melted after wiping the deposited particles off the mirror surface. No literature was found on the emissivity changes of mirror due to thin powder coatings, but even were an empirical correlation available, the upper hemisphere of the chamber usually has a thicker coating, producing an emissivity gradient and complicating the model.

Instead, chamber emissivity was used as a tuning parameter because the emissivity was unknown. This also allowed simplification of the model: rather than including the transparent fused-quartz enclosures used to air-cool the lamp, the tuning parameter also compensated for not modeling the small absorptivity of the fused-quartz lamp enclosure. To estimate mirror emissivity, comparison was made of the simulated power and that actually used to heat an MgO crucible containing Fe to a thermocouple temperature of 1600 °C; the required filament power was 1.395 kW. Table 11.4 shows the simulated thermocouple temperature resulting from a power of 1.395 kW, varying the mirror emissivity. An emissivity of 0.05 resulted in a TC temperature closest to 1600 °C and was used for all subsequent simulations.

Table 11.4. Simulated Thermocouple Temperatures Dependent on Chamber Emissivity

Emissivity	**0.04**	**0.045**	**0.05**	**0.055**	**0.06**
Thermocouple Temperature (°C)	1673	1634	1598	1565	1533

11.5 Results and Discussion

11.5.1 Material Dependence of Temperature Offset:

The results of the calibration melts are shown in Table 11.5. The average temperature offset (ΔT) is defined in Eq. 5 as the difference between the observed thermocouple temperature upon melting and the tabulated (true) melting point of the metal. Ag melted at a thermocouple temperature lower than the tabulated value, but all other metals had a positive temperature offset. Sample mass did have an effect on the offset: offsets of the different-sized Au samples differed by 15 °C, with the heavier sample melting closer to the tabulated temperature. This alone shows that a simple linear calibration of temperature offset does not fully represent the true offsets.

$$\Delta T = T_{measured}^{melt} - T_{actual}^{melt} \quad \text{Eq. 5}$$

Table 11.5. Calibration Experiment Results

Metal	Measured Thermocouple Temperatures (°C)	Melting Temperature (°C)	Average ΔT
Ag	955, 960, 959	962	-4.0
Au (smaller)	1083,1081,1082	1064	18.0
Au (larger)	1066, 1066, 1068, 1067	1064	2.8
Cu	1120, 1110, 1113	1085	30.3
Fe	1580, 1577, 1574	1538	39.0
Ni	1504, 1500, 1500	1455	46.3

The temperature offset differed significantly between similar sample sizes of the same material (Au) at approximately 15 °C and also between different materials of the same size (Cu/Au) at approximately 27 °C. The latter is despite the melting points of Au and Cu being similar - 1064 °C and 1085 °C, respectively. If a linear expression represented the offset well, metals with similar melting points would have similar offsets. For comparison, the two-point calibration, a linear expression based on the melting results of Fe and Cu, is provided in Eq. 6 (for temperatures in °C), with the resulting temperature offset based on the regression given by Eq. 7. From this expression, the offsets at the melting points of Cu and Au would differ by 0.4 °C; the actual difference is more than 12 °C, demonstrating the limitations of the linear expression.

$$T_{actual} = 0.981 * T_{measured} - 9.17 \quad \text{Eq. 6}$$

$$\Delta T = 0.0194 * T_{actual} + 9.35 \quad \text{Eq. 7}$$

To investigate this further, the FEM was used to predict the behavior of Cu and Au heated by the mirror furnace. Two simulations were performed to simulate the response of the solid metals, one with the properties of Au and one with the properties of Cu, in the mirror furnace. Simulations were performed with filament power set to 400 W so that the TC temperature would be near the melting temperature of Au. The simulations predicted the metals to be near the same temperature - 1091.7 and 1091.8 °C for Au and Cu, respectively.

Neither the linear expression nor the FEM could account for the difference in temperature offset between different materials. One possible explanation for failure is a non-zero thermal contact resistance (TCR) between the sample and the crucible (and

between the crucible and the sample support). TCR arises from imperfect contact between surfaces, creating gaps over which heat transfer must occur by radiation or convection rather than conduction [29]. The empirical correlation by Cooper et al. predicts that an increase of normal pressure decreases thermal resistance [30]. This might be a reason for the smaller temperature offset observed with the larger Au sample: assuming a similar sample shape, the larger Au sample would have exerted a larger pressure on the sample-crucible interface.

TCR is not inherently a material property but depends on a material hardness (for solids) and thermal conductivity. The Cooper-Mikic-Yovanovich correlation was used to estimate the trend across metals [30]. When applying the correlation, the surface roughness parameters and interfacial areas were the same for all the metal samples, all metal masses were 0.09 g, the hardness values are those of annealed, room temperature metals [31–33], and the thermal conductivities were taken from Table 11.2. Using this first approximation, the metals in increasing order of contact resistance were Ag, Au, and Cu, agreeing with the trend of temperature offsets. While the trend does agree, the assumptions required to make the prediction means that, while TCR cannot be eliminated as the cause of the offset, it can also not be confirmed. Unfortunately, literature is lacking in tabulated values of the thermal resistance between oxides (crucible material) and metals of less than 1 g. Some investigations of low melting-point liquid metals solidified onto high melting-point metals have been reported, but the instrument response time needed to obtain precise results means even these have not been thoroughly investigated [34].

The inability of both model and regression to predict the temperature offset means caution should be taken when performing CSLM experiments requiring an exact temperature. Figure 11.7 shows the residual values from the Cu-Fe regression in Eq. 7. When comparing pure metals of similar masses melted in MgO crucibles, the error was ± 12.5 °C, based on the maximum of the residual values.

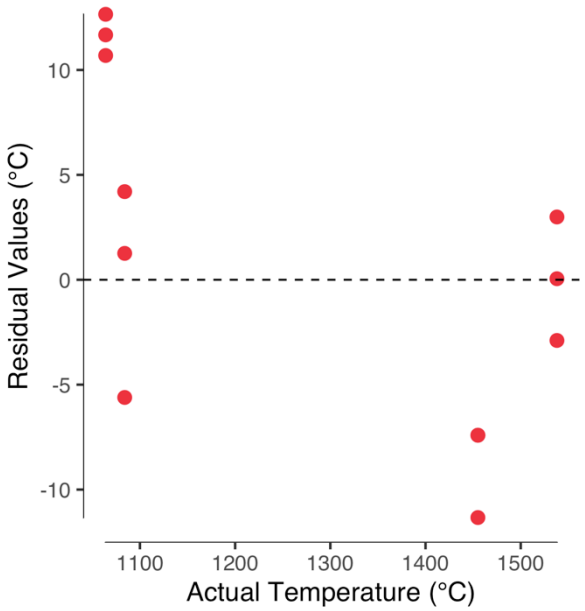

Figure 11.7. Residual values of melting temperatures compared to the linear regression Eq. 6. All points used a similar mass of material, i.e., the larger Au sample is not shown.

A more precise offset correction can be determined, but investigation into a method other than linear regression is required. In solid steels, the temperature offset was found to be constant between the melting temperature and 120 °C cooler [15,18]. Assuming that the offset is constant for even lower temperatures (an assumption yet unproven), observing a solid-state phase transition of the metal of interest could provide a reference for the offset. The austenite-ferrite transition in steel could provide such a reference point if the offset is found to be constant between the transition temperature and the melting temperature. However, other metals must be observed to prove that the temperature offset is constant over a certain range. This could be an issue when using materials with higher thermal conductivities, such as Cu. Finally, as studies like that of Yin and Emi have not been able to record the temperature of the metal beyond the solidus [15], it must be proven that the shape change upon melting does not affect the offset; to date no direct measure of the temperature offset when the metal is liquid has been reported.

11.5.2 Particle Tracking and Model Validation

The general direction of particle movement on the metal droplet surface is shown in Figure 11.8a. Particles traveled from South to North, moving through the center, before turning around in the Northern region of the droplet. This change in direction coincided with a steeper region of the droplet surface, detectable by the focus fall-off. The statistics and distribution of the three observed regions are shown in Figure 11.8b-d, and statistical values are presented in Table 11.6. The particles moved fastest in the

Southern region, slowed at the highest point of the droplet (the center region) and maintained a roughly constant velocity through the direction change in the Northern region. At each location, particle velocities had a median near 20 µm/s, and more than 90% of the particles had a velocity below 50 µm/s.

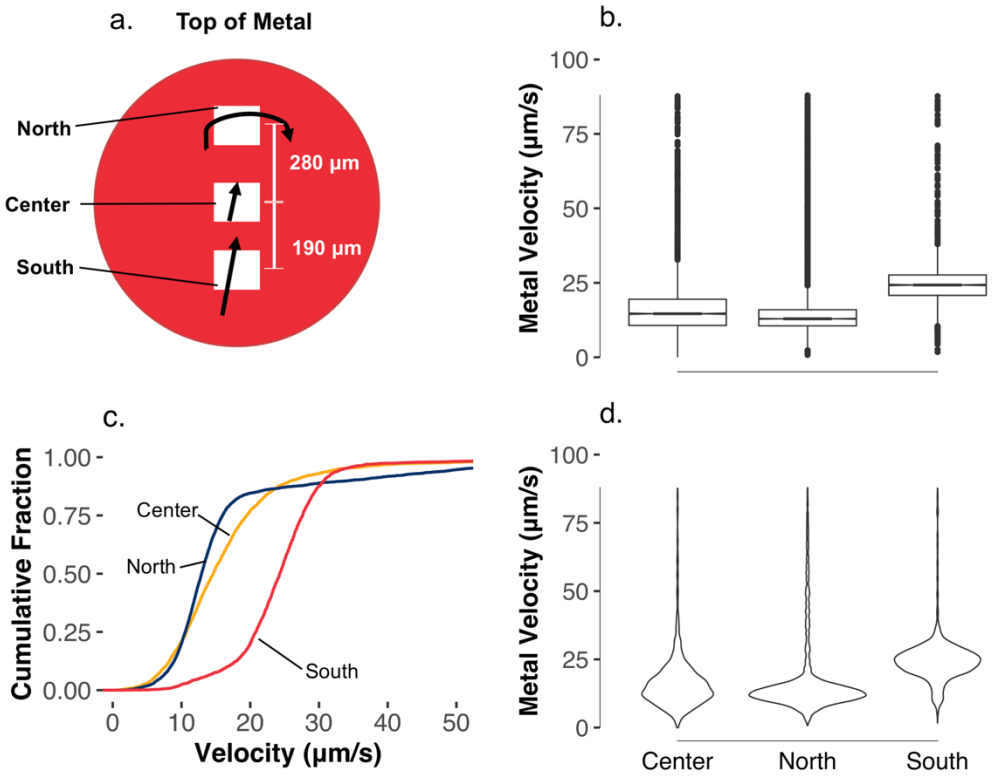

Figure 11.8. Results of the experimentally tracked particles. a.) Schematic showing locations analyzed and the direction of particles within. b.) Statistics of the tracked particle velocities for the three locations. c.) Empirical cumulative distribution for the three locations. d.) Violin plot showing the distribution of velocity for the three locations.

Table 11.6. Statistics of Experimentally Tracked Particles (µm/s)

	1st Quartile	Median	Mean	3rd Quartile	Upper Fence
Center	0.5	14.6	16.6	19.5	32.7
North	10.5	12.9	17.1	16.0	24.1
South	20.8	24.3	24.6	27.6	37.8

Marangoni flow is sensitive to surface tension gradients (and hence thermal gradients) on the surface of the sample, and therefore it should be possible to validate the thermal gradients of the FEM by comparing particle movement on the molten metal surface with simulated velocities. The results simulated with a power of 1.347 kW are shown in Figure 11.9. Figure 11.9a shows the temperature of the thermocouple and the temperature of the droplet along the axis of symmetry. There is some uncertainty about

the exact location the TC measures, but the simulated temperature was between 1579.5 °C and 1581.2 °C, a match to the experimental condition. The simulated droplet exhibited a 1.2 °C temperature difference over the height of metal, and the simulated fluid flow in Figure 11.9b showed a maximum velocity of 3.3 mm/s and an anticlockwise flow. Including the radiative heating chamber in the simulation resulted in values of both the temperature difference over the metal height and the fluid velocity to be an order of magnitude lower than previously predicted [16]. Figure 11.9c and d show the velocity magnitude and the temperature along the top surface of the droplet. The fluid direction follows what is expected for surface tension driven flow: fluid flows away from the region of highest temperature (and lowest surface tension) to the region of lower temperature.

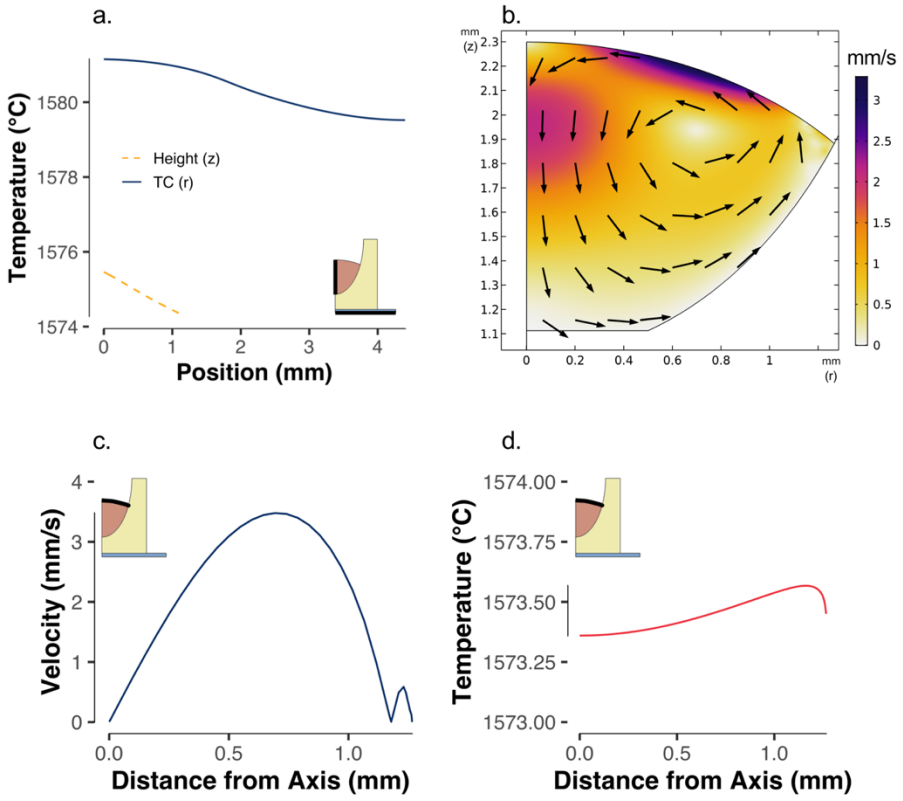

Figure 11.9. Results of the simulation with ε = 0.05 and power = 1.347 kW. a.) Temperature of the thermocouple over its width and the metal over its height. Zero is closer to the origin in both cases. b.) Fluid flow profile. c.) Velocity of the top surface of the metal droplet. d.) Temperature of the top surface of the droplet.

The simulation overestimated the velocity compared to the experimental observations. The Southern region was centered 190 µm away from the top of the droplet, and the image was 240 µm tall, giving a field of view between 70 to 310 µm from the droplet top. A representative micrograph with overlaid velocity vectors is shown in Figure 11.10a with coupled simulation result in Figure 11.10b. Over this

range, the simulation predicted a minimum velocity of 0.5 mm/s (nearer the droplet top) and a maximum of 2.2 mm/s (nearer the crucible wall). Less than 2% of the observations fell within this predicted velocity range: the simulation over-estimated the particle velocity by two orders of magnitude. Furthermore, moving farther from the droplet top should further increase the velocity, but there was little change in velocity when comparing the Northern observations to the center observations. This is partially due to the limitations of a 2D model, which could only capture radial flow and not the circumferential flow that was observed. A 3D simulation with coarse meshing was performed, but the results predicted little circumferential flow.

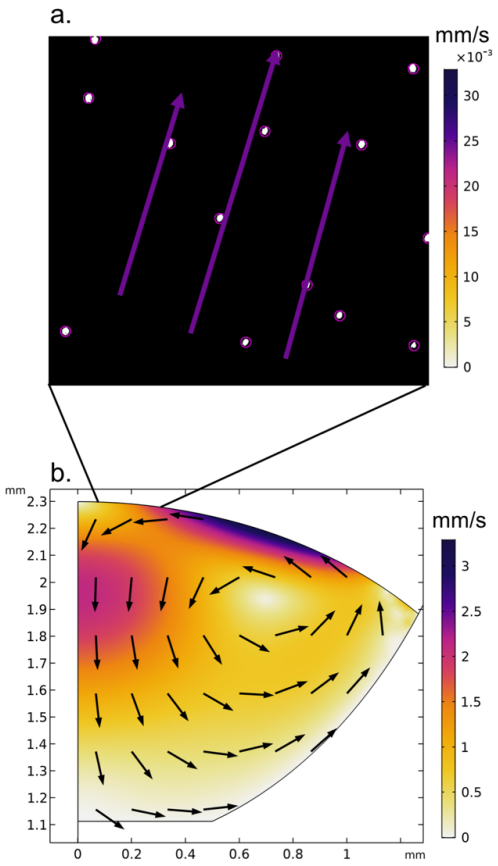

Figure 11.10. a.) Processed frame from CSLM (Southern location) annotated with particle velocity vectors. Particles are shown in white and circled in purple. b.) Simulated results annotated with spatial location of the observed frame. This frame corresponds to the $70 \leq r \leq 310$ μm relative to the highest point of the droplet. Color bars depict the different scales between a and b.

Despite the mismatch between the simulated and experimental results, conclusions can still be drawn. Because flow is surface tension driven, it is sensitive to temperature gradient. A temperature difference of 1.2 °C over the height of the droplet resulted in a maximum velocity of 3.3 mm/s in the simulated condition. As the experimental

velocity was smaller, the expected temperature difference within the metal should be much smaller than 1.2 °C.

One major uncertainty of the model is the shape of the droplet. The model assumed a symmetric profile, but that was not the practical case. Even when precisely measuring the sample shape after experiments, the solidified shape would not have been the same as that of the liquid droplet. Figure 11.11 shows how small changes in the height and width of the upper ellipsoid (defining the top of the droplet) can affect the fluid direction and magnitude. As the droplet height decreased or the primitive width increased (both leading to a smaller curvature), the maximum surface velocity decreased, seen in Figure 11.11a. Figure 11.11b-d show the fluid profile of droplets with height of 1 mm and increasing the width of the top of the upper ellipsoid. The highest velocity of these had a width of 1 mm (the largest curvature). This height was distinct because the minimum velocity was obtained at a width of 1.75 mm; the other simulated heights had minimums corresponding to the larger widths (the smallest curvature). This was due to the intermediate flow pattern seen in Figure 11.11c: the flow pattern was primarily anticlockwise, but beyond a width of 1.75 mm there was a clockwise flow pattern. A continued decrease in curvature (Figure 11.11d) resulted in the entire pattern becoming clockwise, and the velocity increased compared to the intermediate case. Curvature affects the radiative heat transfer, with a decrease in curvature shifting the hottest part of the droplet from the center to the edges. This drives the flow pattern, with flow from the hottest surface location to the coldest. The important conclusion is that the simulated velocity is strongly dependent upon droplet shape. However, this dependency does not extend to the absolute temperature; that is, the droplet shape did not affect the average temperature predicted by the FEM. Rather, the changes in surface temperature were fractions of a degree Celsius, similar to Figure 11.9d.

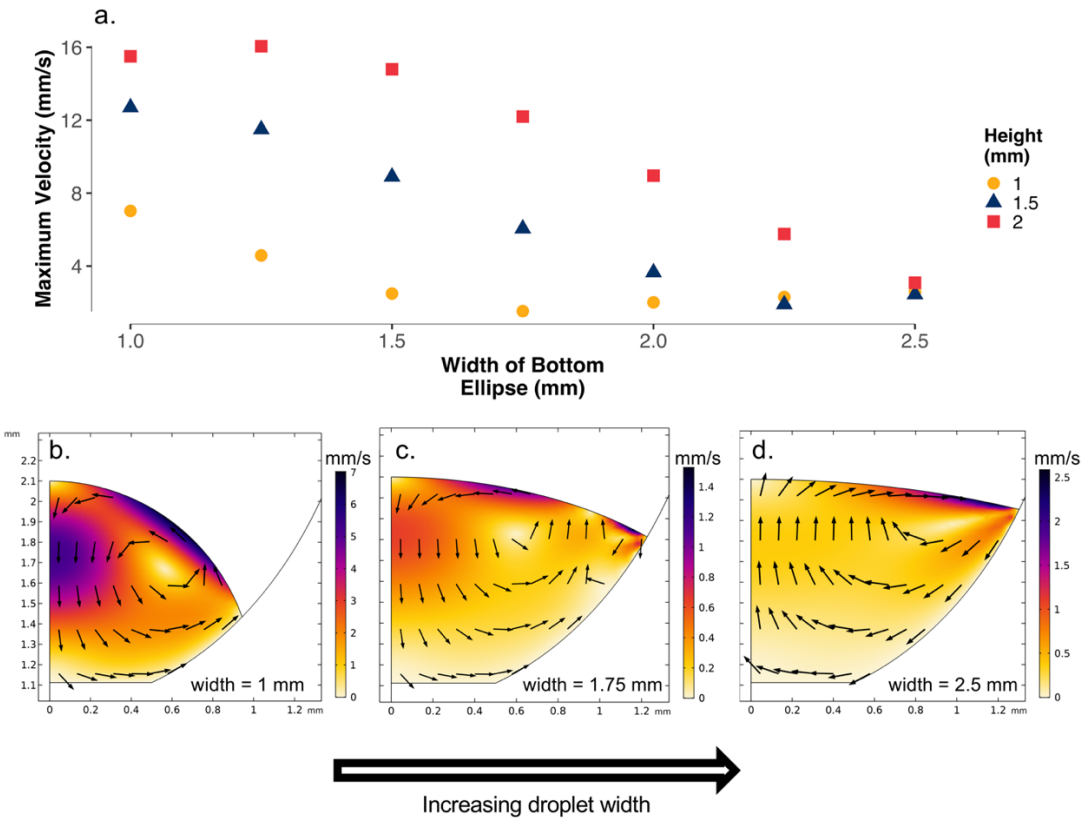

Figure 11.11. Sensitivity of predicted velocity to droplet shape. a.) Effect of the droplet height and width on the maximum surface velocity. Simulated velocities for droplets of different shapes: b.) height 1 mm and width 1 mm; c.) height 1 mm and width 1.75 mm; d.) height 1 mm and width 2.5 mm. The color bar changes to show the maximum velocity of simulation. Case c.) had the lowest velocities as flow was intermediate between fully clockwise or fully anticlockwise.

Since the simulated fluid flow was sensitive to the droplet geometry, it is likely also sensitive to other approximations that were made in the model. It has already been mentioned that the real metal droplet was not exactly symmetrical as assumed, and the CSLM chamber has further asymmetries such as the alumina rod that supports the sample. The inclusion of the rod would likely create asymmetric heating, leading to higher temperature gradients. In addition, the fused-quartz window for the laser is important. Not including the window (that is, removing the hole at the top of the chamber) resulted in a 20 °C increase in the droplet temperature and a clockwise flow pattern. This model treated the window as an opening but modelling it as a transparent medium (with non-zero absorptivity and reflectivity) could affect the results. The asymmetry in the experimental observation also reveals some limitations of the 2D axisymmetric model. Particles moved over the center of the droplet and showed some circumferential flow rather than only flowing to the center from all directions before coalescing or disappearing beneath the surface.

Though multiple assumptions were made in the model, and simulated velocities were higher than observed, the model allows useful qualitative conclusions. Modeling reflections within the mirror furnace was necessary to approach a realistic solution; the inclusion of reflections resulted in a temperature difference of 1.2 °C rather than 20 °C as previously reported [16]. The simulated fluid velocities were an order of magnitude higher than observed. As gradients drive the flow of liquid in CSLM samples, smaller velocities than predicted should stem from smaller temperature differences than predicted. For operators of the CSLM, there should be little concern about temperature gradients affecting experiments, but greater care should be taken in determining the temperature offset (between the sample and the measurement thermocouple), particularly for experiments where a precise temperature is required.

11.6 Conclusions

- The temperature offset between the melting point and measured melting temperature of various metals in the CSLM was not fully captured by either the standard method of a linear calibration or a finite element model simulating radiative heating by a mirror furnace. The implication is that researchers should take care when reporting results from the CSLM that require accurate knowledge of the droplet temperature.
- For pure metals of similar masses melted in MgO crucibles, using a linear regression based on the melting of pure Fe and Cu resulted in an error of ± 12.5 °C, based on the maximum of the residual values.
- An experimental technique was documented to find the highest point of the liquid droplet, and a methodology was presented to automatically track particles that have low contrast with the molten metal bath, while avoiding the effect of mismatched frame rates. MgO particles observed on liquid Fe were observed to have median velocities on the order of 20 μm/s.
- A multi-physics finite element model of the CSLM was developed to include reflections from the mirror furnace when radiatively heating a liquid iron sample. The model showed a temperature difference of 1.2 °C over its height, an order of magnitude lower than previous reported. The predicted velocity was still larger than reality, based on the velocity of particles observed in the experiment. Actual temperature gradients should be lower than those simulated, and the temperature difference in the droplet should be less than 1.2 °C. The model was sensitive to the droplet shape, with decreasing velocity when the top surface became less convex or when the droplet height was reduced.

11.7 Hypotheses Revisited

The melting offset of pure metals in the CSLM is material dependent, and differs by more than 5 °C for pure metals that have melting points within 25 °C.

This hypothesis is supported. Through melting pure Cu and pure Au, the observed melting temperature was dependent on both material and mass of material.

The temperature difference over the height of a liquid Fe sample contained in an MgO crucible is less than 3 K.

This hypothesis is supported. The particle tracing coupled with finite element model support that the temperature difference is much less than 3 K.

11.8 References

[1] Y. Ren, P. Zhu, C. Ren, N. Liu, and L. Zhang: *Metall. Mater. Trans. B*, 2022, vol. 53, pp. 682–92.
[2] R. Sarkar and Z. Li: *Metall. Mater. Trans. B*, 2021, vol. 52, pp. 1357–78.
[3] Y. Liu, Y. Sun, and H. Wu: *Int. J. Miner. Metall. Mater.*, 2021, vol. 28, pp. 1011–21.
[4] J. Zeng, C. Zhu, W. Wang, and X. Li: *Metall. Mater. Trans. B*, 2020, vol. 51, pp. 2522–31.
[5] M.E. Story and B.A. Webler: *JOM*, 2018, vol. 70, pp. 1225–31.
[6] E. Schmidt, D. Soltesz, S. Roberts, A. Bednar, and S. Sridhar: *ISIJ Int.*, 2006, vol. 46, pp. 1500–9.
[7] S.P.T. Piva, D. Tang, D. Kumar, and P.C. Pistorius: in *TMS 2018 147th Annual Meeting & Exhibition Supplemental Proceedings*, Springer, Cham, 2018, pp. 193–200.
[8] H. Abdeyazdan, N. Dogan, R.J. Longbottom, M. Akbar Rhamdhani, M.W. Chapman, and B.J. Monaghan: in *Advanced Real Time Imaging II*, The Minerals, Metals & Materials Society, 2019, pp. 61–73.
[9] Y. Li, Y. Li, and R.J. Fruehan: *ISIJ Int.*, 2001, vol. 41, pp. 1417–22.
[10] Y. Kang, P.R. Scheller, D. Sichen, and K. Morita: in *Advanced Real Time Imaging II*, The Minerals, Metals & Materials Society, 2019, pp. 13–8.
[11] G. Wang, Y. Zhao, Y. Xiao, P. Jin, S. Li, and S. Sridhar: *Metall. Mater. Trans. B*, 2020, vol. 51, pp. 3051–66.
[12] T. Britt and P.C. Pistorius: *Metall. Mater. Trans. B*, 2021, vol. 52, pp. 1–5.
[13] H. Mu, T. Zhang, L. Yang, R.R. Xavier, R.J. Fruehan, and B.A. Webler: *Metall. Mater. Trans. B*, 2016, vol. 47, pp. 3375–83.
[14] H. Yin, H. Shibata, T. Emi, and M. Suzuki: *ISIJ Int.*, 1997, vol. 37, pp. 936–45.
[15] H. Yin and T. Emi: *Metall. Mater. Trans. B*, 2003, vol. 34, pp. 483–93.
[16] S. Piva, P. Pistorius, and B. Webler: *JOM*, 2018, vol. 70, pp. 1193–8.
[17] J.J. Valencia and P.N. Quested: in *Casting*, S. Viswanathan, D. Apelian, R.J. Donahue, B. DasGupta, M. Gywn, J.L. Jorstad, R.W. Monroe, M. Sahoo, T.E. Prucha, and D. Twarog, eds., vol. 15, ASM International, 2008.

[18] Y. Arai, T. Emi, H. Fredriksson, and H. Shibata: *Metall. Mater. Trans. A Phys. Metall. Mater. Sci.*, 2005, vol. 36, pp. 3065–74.
[19] I. Arganda-Carreras, V. Kaynig, C. Rueden, K.W. Eliceiri, J. Schindelin, A. Cardona, and H. Sebastian Seung: *Bioinformatics*, 2017, vol. 33, pp. 2424–6.
[20] J.-Y. Tinevez, N. Perry, J. Schindelin, G.M. Hoopes, G.D. Reynolds, E. Laplantine, S.Y. Bednarek, S.L. Shorte, and K.W. Eliceiri: *Methods*, 2017, vol. 115, pp. 80–90.
[21] *COMSOL Multiphysics® v. 5.5*, COMSOL AB, Stockholm, Sweden.
[22] Springer Materials: in *Landolt-Börnstein: 19A1. Pure Substances: Part 1 Elements and Compounds from AgBr to Ba3N2*, Springer-Verlag, Berlin/Heidelberg, pp. 1–24.
[23] O. Rozenbaum, D. De Sousa Meneses, Y. Auger, S. Chermanne, and P. Echegut: *Rev. Sci. Instrum.*, 1999, vol. 70, pp. 4020–5.
[24] A.J. Slifka, B.J. Filla, and J.M. Phelps: *J. Res. Natl. Inst. Stand. Technol.*, 1998, vol. 103, p. 357.
[25] C.W. Bale, E. Bélisle, P. Chartrand, S.A. Decterov, G. Eriksson, A.E. Gheribi, K. Hack, I.H. Jung, Y.B. Kang, J. Melançon, A.D. Pelton, S. Petersen, C. Robelin, J. Sangster, P. Spencer, and M.-A. Van Ende: *Calphad*, 2016, 54, vol. 54.
[26] G. Neuer and G. Jaroma-Weiland: *Int. J. Thermophys.*, 1998, vol. 19, pp. 917–29.
[27] C. Smithells: in *Smithells metals reference book*, 8th ed., Elsevier Butterworth-Heinemann, Amsterdam, 2004, pp. 14–1, 14–43.
[28] W. Sabuga and R. Todtenhaupt: *High Temp. Press.*, 2001, vol. 33, pp. 261–9.
[29] Y. Xian, P. Zhang, S. Zhai, P. Yuan, and D. Yang: *Appl. Therm. Eng.*, 2018, vol. 130, pp. 1530–48.
[30] M. Cooper, B. Mikic, and M. Yovanovich: *Int. J. Heat Mass Transf.*, 1969, vol. 12, pp. 279–300.
[31] W.J. Poole, M.F. Ashby, and N.A. Fleck: *Scr. Mater.*, 1996, vol. 34, pp. 559–64.
[32] C.C. Lo, J.A. Augis, and M.R. Pinnel: *J. Appl. Phys.*, 1979, vol. 50, pp. 6887–91.
[33] Q. Ma and D.R. Clarke: *J. Mater. Res.*, 1995, vol. 10, pp. 853–63.
[34] Y. Heichal and S. Chandra: *J. Heat Transfer*, 2005, vol. 127, pp. 1269–75.

12 Hypotheses Revisited

Table 12.1 lists the hypotheses presented in Ch. 4 and the result, either supported, partially supported, or unsupported.

Table 12.1 Hypotheses Revisited

Ch.	Hypothesis	Conclusion
6	The formation of Ti(C,N) will decrease the dissolution rate of pure graphite 70% compared to a binary alloy and 30% compared to dissolved Ti alone.	**Unsupported:** Dissolved Ti had no effect on the dissolution kinetics. The average normalized mass transfer coefficient of metal containing Ti(C,N) had a mean value 20% less than that dissolved in the binary alloy.
7	Doping coke analog coated graphite rods with 10% TiC will result in the formation of statistically significantly thicker solid iron shells, compared with undoped coatings or those containing Ti(C,N) or TiN.	**Partially Supported:** the shell diameter for coatings containing TiC were statistically significantly larger only compared with TiN, not compared with those undoped or containing Ti(C,N).
8	Liquid Fe-C_{sat} will not react with or wet glassy carbon. An angle of contact should be greater than 90°.	**Unsupported:** glassy carbon was reactively wetted by Fe-C_{sat}
10	The wetting of alumina by Fe-C_{sat}-Ti can be prevented by coating the crucible in a thin layer of liquid flux. This should raise the angle of contact by at least 10°.	**Supported:** the angle of wetting was raised by a minimum of 15° when the alumina crucible was coated with flux.
11	The temperature gradient over the height of a liquid Fe sample contained in an MgO crucible is less than 3 K.	**Supported:** the particle tracing coupled with finite element model support that the temperature gradient is less than 3 K.
11	The melting offset of pure metals in the CSLM is temperature dependent, and differs by more than 5 °C for pure metals that have melting points within 25 °C.	**Supported:** the offsets of Au and Cu were respectively 3 °C and 30 °C, greater than 5 °C.

13 Conclusions

The primary impact of this work should be further elucidation as to how titanium additions protect the hearth. Previously, the mechanism described by literature discussed how protection might occur. The present work has filled in some of the peripheral details of the mechanism described by Bergsma and Fruehan. From a fundamental materials science perspective, one finding is why Ti is uniquely able to protect the hearth. Ti(C,N) particles have a strong tendency to combine, creating large, linked Ti(C,N) agglomerations. These agglomerations should better restrict flow in worn regions than individual particles.

From a practical perspective, this work emphasizes the importance of heat transfer when protecting the hearth by Ti additions. The importance of heat transfer to hearth protection is seen in Ch. 6 and 7. For refractory wear by dissolution, it was not enough for Ti(C,N) to be in the melt to see a major reduction in dissolution rate. A shell must be solidified to see the beneficial effects reported by industry. Skull formation was seen to be heat transfer controlled in Ch. 7. These measurements were performed in stagnant melts, and skulls that formed on rods containing TiC or Ti(C,N) differed little in thicknesses as opposed to rods that were undoped. While not proven by this work, the authors propose that formation of a skull in the hearth is likely to be under mixed control when Ti is present, a combination of heat transfer and reaching a critical concentration of Ti(C,N) at the worn area. When doping hearth refractory with Ti(C,N), the formation of pure TiN should be avoided due to its lack of adhesion to the refractory.

Beyond the effects of Ti(C,N), this work also shows the catalytic graphitization of glassy carbon crucibles by Fe-C_{sat}. Comparison to a coke analog substrate reveals significant differences between the different carbonaceous materials and liquid Fe-C_{sat}. Analogs showed little penetration or interaction with the Fe-C_{sat}. Glassy carbon is reported to have a faster dissolution rate than metallurgical coke, that is thought to result in the different extent of interactions.

Finally, the work presents results that make the HT-CSLM a more useful quantitative tool. A practical methodology was developed to allow easier viewing of liquid metallic samples. The specific experiment used flux to prevent wetting of the Al_2O_3 crucibles by liquid metal, but the principle- using a liquid flux or oxide to change the surface chemistry of the crucible- can be adapted to other systems that experience problematic wetting. Standard practices of using the CSLM were also challenged. One held up

against investigation- the thermal gradient within CSLM samples was quite small- while the other did not- the temperature offset was independent of material. These findings further characterize the conditions within the heating chamber of the microscope and should give future researchers confidence when using the microscope and reporting results.

14 Future Work

These ideas for future work are contained within Ch. 5-7 but are repeated here for ease of reference.

14.1 Skull Formation Experiments including Heat Transfer and Forced Stirring

Ch. 6-7 sought to understand Bergsma and Fruehan's mechanism of hearth protection by increasing the experimental complexity. The shell formation experiments included heat transfer effects but was contained in a stagnant melt. Because of the importance of the viscosity to the proposed mechanism, future experiments should include some external stirring. One proposed experiment would be performing the skull formation experiments in a high-frequency induction furnace, enabling convection by magnetic stirring. Should that stirring not be enough, an experiment is imagined using a modified set-up from Ch. 6. Replacing the stirring assembly with a single rod of graphite (~1.5 cm) diameter should allow enough heat extraction to solidify a shell of iron while stirring.

14.2 Computational Fluid Dynamics

A constant problem when charging Ti is how to effectively localize it at the region of wear. As noted in Ch. 7, the formation of a Ti-bear could be limited by both heat transfer and the concentration of Ti(C,N) particles. A computation model that includes heat transfer, fluid flow, and particle thermodynamics could be utilized to predict skull formations based on charge practice of Ti additions.

14.3 Adhesion of TiC to Carbonaceous Refractory

Ch. 5 documented an experiment to test if TiC could remain on graphite in spite of hot metal undersaturated in TiC. These experiments were unable to be performed quantitatively. Future work could utilize micro-computed tomography to quantify the amount of TiC lost in these experiments. Though TiC is the only Ti-based compound known to be added to hearth refractory, studying Ti(C,N) and TiN should also be beneficial.

15 Glossary

Ash — inorganic mineral impurities contained within carbonaceous materials
BF — blast furnace
Bear — titanium accretions on the hot face of the BF refractory
CFD — Computational fluid dynamics
CSLM — Confocal scanning laser microscope
FEA — Finite element analysis
Hot face — the side of refractory contacting hot metal
HM — hot metal
[Me] — dissolved content by weight of element Me in hot metal
(MeO) — dissolved content of metal oxide by weight in slag
NTHM — net ton of hot metal; a unit of production
p_{N_2} — partial pressure of N_2
p_{O_2} — Partial pressure of O_2
Skull — layer of solidified iron on the hot face of the refractory
TC — thermocouple